Characterization of rapid prototyped Ti6Al4V bone scaffolds by the combined use of micro-CT and in situ loading

PROYECTO FIN DE CARRERA

INGENIERÍA INDUSTRIAL

Autora: Laida Elicegui Garciandia

Directores: Martine Wevers, Jan Schrooten (Katholieke Universiteit Leuven)

Cotutora: Elisa Ruiz Navas (Universidad Carlos III de Madrid)

Leganés, Septiembre 2009

Preface

To my family and friends,

Thanks to Carlos III University of Madrid, and especially to Elisa Ruiz for her help, for giving me the opportunity of doing my master thesis in the Katholieke Universiteit Leuven. Thanks to Martine, Jan, Simon, Maarten, Saartje, Kris, Kristof, Paul and, above all, to Greet. It was a pleasure to work with you in Belgium.

Summary

The present project dealt with the morphological and mechanical characterization of Ti6Al4V bone scaffolds produced by Selective Laser Melting, via micro-CT combined with in situ compressive loading. The in situ loading stage was first validated by proving that there was no difference between compressing the bone scaffolds on a conventional loading device, or on the in situ loading stage. Then, the effect of stepwise loading on the derived mechanical properties was assessed, showing a significant difference for the E-modulus, since the structures were non-linear elastic. It was seen that the variation of mechanical and morphological parameters for scaffolds with the same design within one production batch was neglectable. Thus, for future work, one random scaffold might be considered as representative for those produced with the same design. The influence of varying the pore size while keeping the strut size constant was assessed both morphologically and mechanically, setting up a protocol for future assessment of the scaffolds. The combination of micro-CT and in situ loading allowed to relate the failure mechanisms to the design and to locate the onset of failure by the change in morphological parameters.

List of Symbols

2D	Two Dimensional
3D	Three Dimensional
3DFD	Three Dimensional Fiber Deposition
CAD	Computer Aided Design
CT	Computed Tomography
E	Young's modulus (MPa)
E_s	Young's modulus of the bulk material (MPa)
FE	Finite Element
FEA	Finite Element Analysis
I	Intensity of incident radiation (# photons)
RP	Rapid Prototyping
SLM	Selective Laser Melting
TE	Tissue Engineering
c	Speed of light (m/s)
h	Planck's constant (Js)
ρ^*	Density of the porous material (g/cm^3)
ρ_s	Density of the bulk material (g/cm^3)
σ_{ucs}	Ultimate compressive strength (MPa)
ε_{ucs}	Strain at ultimate compressive strength (MPa)
σ_{ys}	Yield stress of the bulk material (MPa)
λ	Wavelength (nm)
ν	Frequency (Hz)
μ	Linear attenuation coefficient (cm^{-1})

List of Figures

List of Tables

Table of Contents

1. General introduction

Porous structures play an important role in everyday life. They can be used in many applications; for thermal insulation, packaging, as structural materials or floating materials and, more recently, in bone tissue engineering (TE), for the replacement of damaged bones, since, bone itself is a porous material, by seeding cells onto porous matrices known as scaffolds.

In the field of TE the tendency is to evolve from the use of foams with random microstructures to highly controllable designed structures, which allow a variation on the morphological parameters of the scaffold, so that research can be done towards a better understanding of the role of morphological and mechanical aspects, which are of main importance for the seeding and growth of cells. This control over the designed structures can be achieved by using rapid prototyping (RP) techniques.

The present project will deal with the morphological and mechanical characterization of Ti6Al4V bone scaffolds, with different pore sizes, produced by an RP technique named Selective Laser Melting (SLM) with two different machines, LM and Concept. Mechanical and morphological analysis will be carried out, via several methods, amongst which stepwise loading combined with intermediate microfocus X-ray computed tomography (micro-CT) scanning should be mentioned, with the final goal of finding a correlation between them. In the present project, a novel in situ loading stage will be placed inside the micro-CT to allow stepwise loading with intermediate scanning and avoid the transfer of the samples.

Chapter 2 pretends to give an idea on what TE is, the state of the art of the production techniques for bone TE engineering scaffolds and the use of stepwise loading combined with micro-CT for the characterization of porous structures. Thus, give the reader a general overview on the state of the art to make understandable the reason why the present project was carried out.

Chapters 4, 5 and 6 will deal with mechanical and morphological characterization, via Archimedes, microhardness tests and microscopy respectively, of porous RP Ti6Al4V scaffolds produced with LM and Concept machine. This will serve to assess the performance and robustness of SLM technique and see whether there is any difference on the performance of the LM and the Concept machine.

Chapter 7 will deal with a thorough mechanical compressive characterization of the assessed material. As mentioned before, a novel in situ loading stage will be placed inside the micro-CT to avoid the transfer of the samples. The main goal will be the validation of the novel in situ loading stage by loading the samples on an Instron 4505, which is a conventional loading device, and the in situ loading stage.There will also be a part devoted to bulk RP Ti6Al4V structures in order to have an idea of the performance of the technique by comparing the experimental results to the theoretical for bulk Ti6Al4V. There will be another part on the compressive and cyclic (fatigue) behavior of the RP porous Ti6Al4V scaffolds produced with both LM and Concept machines. This will serve to derive any differences on the mechanical behavior that may be attributed to the machine the scaffolds were produced with.

Chapter 8 will talk about micro-CT combined with in situ loading. First, a comparison will be made between the data obtained by continuous compression loading and stepwise loading to derive whether they are significantly different or not. Second, a morphological characterization of the samples will be done on the preloaded stage. Validation of the data obtained via micro-CT will be done by comparing the value of porosity obtained with the one from Archimedes. After, stepwise compression loading combined with micro-CT imaging will be done to analyze the evolution of the morphological parameters of the scaffolds under varying compressive load, thus, for different strain values, as well as to derive the failure mechanisms.

In fact, all the chapters will be oriented to setting up a protocol for further research on the relation of morphological and mechanical parameters of porous RP Ti6Al4V scaffolds via stepwise loading with intermediate micro-CT imaging.

2. Literature review

2.1. Introduction

A porous solid is one made up of an interconnected network of solid struts or plates which form the edges or faces of pores. Such materials are common in nature: wood, cork, bone and sponge, for example. Man has made use of these natural cellular materials for centuries and, more recently, man has made his own. Among the latter, we can find the honeycomb-like materials and metallic, polymeric or ceramic foams.

Nowadays, almost any material can be foamed and metals, ceramics, glasses, and even composites, can be fabricated into porous materials.

The single most important feature of a porous solid is its *relative density*, ρ^*/ρ_s; that is, the density of the porous material, ρ^*, divided by that of the solid from which the pore walls are made, ρ_s. Very high specific properties can be achieved in porous solids due to their low density. The four major areas of application of porous materials have always been thermal insulation, packaging, structural use, and buoyancy. However, more recently the biomedical use is becoming of major importance.

Cellular materials can lead to great improvements, amongst others by imitating nature, which is the main goal of TE (Sachlos and Czernuszka [2003; Yeong et al. [2004]). It is an interdisciplinary field which applies the principles of engineering and life sciences to the development of biological substitutes that restore, maintain or improve tissue function. This is achieved by seeding cells onto porous matrices known as scaffolds. Thus, the scaffold attempts to mimic the function of the natural extracellular matrix, providing a temporary template for the growth of target tissues.

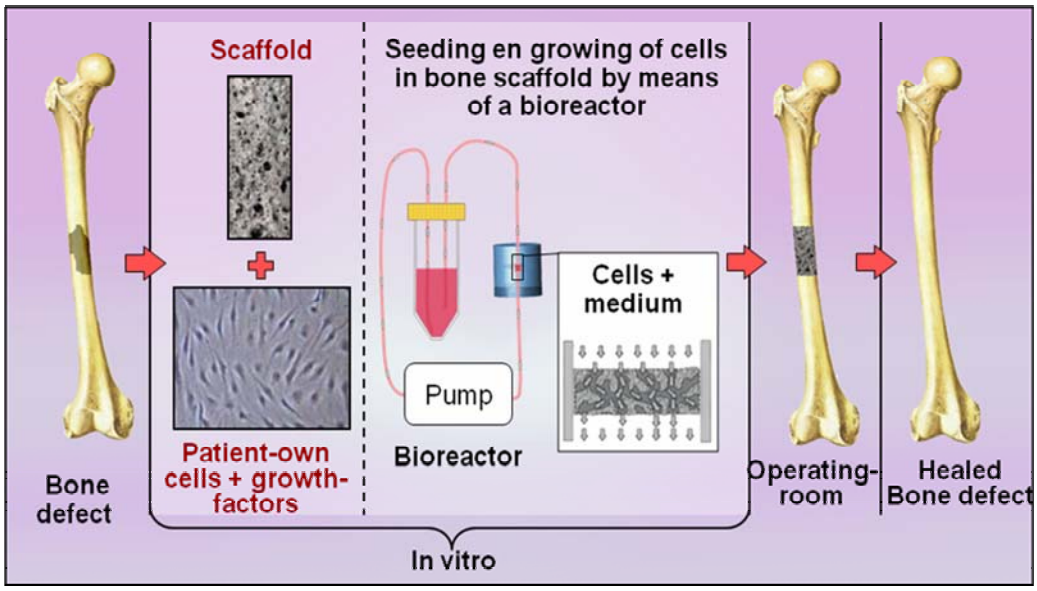

Fig.2.1. Schematic overview of bone tissue engineering.

Several requirements, apart from density, have been identified as crucial for the production of TE scaffolds (Sachlos and Czernuszka [2003]). They should:

- Possess interconnecting pores of appropriate scale (pore size, pore shape, porosity and interconnecting pore size) to favor tissue integration and vascularisation.
- Be made from materials which are bioinert, as Ti6Al4V, or with controlled biodegradability so that tissue will eventually replace the scaffold.
- Have appropriate surface chemistry to favor cellular attachment, differentiation and proliferation.
- Not induce any adverse response.
- Be easily fabricated into a variety of shapes and sizes.
- Possess adequate mechanical properties to match the intended site of implantation and handling.

It can be seen that those characteristics scaffolds have to meet can be divided in two kinds. One of them concerning the medical field and the other related to the engineering field, because design and fabrication of bone scaffolds should find a balance between mechanical function and biological performance.

The present project will deal with the engineering part of the analysis of the TE scaffolds and, more specific, it will focus on the combination of micro-CT imaging, image analysis and in-situ loading (inside the micro-CT device) to determine the morphological and the related mechanical properties of Ti6Al4V scaffolds for bone engineering. Bone engineering is a field within TE (Fig.2.1). After fracture, bone disease or other conditions resulting in skeletal loss or compromise, porous materials offer the possibility for nearly faultless replacement of the normal bone material. Scaffolds are used for replacing bone, because bone itself is a porous material.

2.2. Production techniques

Conventional scaffold fabrication techniques include, for example, solvent-casting particulate-leaching, gas foaming, fiber meshes and fiber bonding, phase separation, melt molding, emulsion freeze drying, solution casting or freeze drying (Sachlos and Czernuszka [2003]; Yeong et al. [2004]). However, there are inherent limitations in these processing methods, which offer little capability to precisely control pore size, pore geometry, pore interconnectivity, spatial distribution of pores and construction of internal channels within the scaffold.

In the field of TE the tendency is to evolve from the use of foams with random microstructures to highly controllable designed structures, which leads to an improvement of the predictability of in-vitro and in-vivo experiments in which morphological parameters are systematically varied, yielding better understanding of the role of morphological and mechanical aspects. This control over the designed structures can be achieved by using RP techniques.

RP is a common name for a group of techniques that can generate a physical model directly from computer-aided design (CAD) data. It is a broad

field in which two main techniques can be distinguished: direct RP and indirect RP. In direct RP the scaffold is fabricated while in indirect RP, RP systems are used to produce a sacrificial mold to fabricate TE scaffolds (Yeong et al. [2004]). Based on a 3D CAD model, the virtual product has to be analyzed by specific software programs which prepare the model slicing it into layers of constant thickness (Hollander et al. [2003]). This allows the production of scaffolds with customized external shape and predefined and reproducible internal morphology, thus, controlled pore size, porosity and pore distribution (Sachlos and Czernuszka [2003]) allowing TE grafts to be tailored for specific applications or even for individual patients (Hutmacher et al. [2004]). Besides, the use of RP techniques can reduce time and cost significantly compared to conventional techniques (Hollander et al. [2003]).

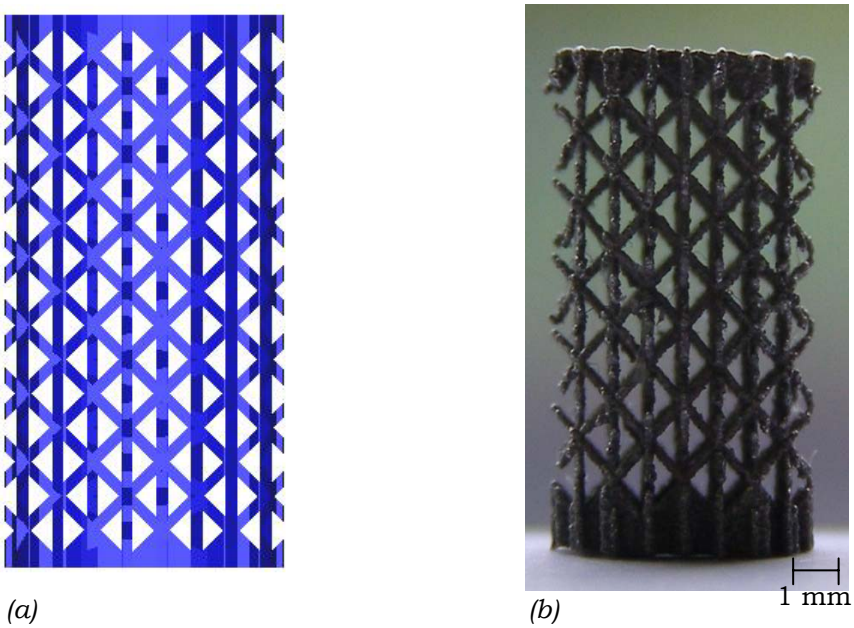

Fig.2.2. ***(a)*** **CAD design of a porous Ti6Al4V scaffold** ***(b)*** **Picture of porous RP Ti6Al4V scaffold.**

The potential of 3D fiber deposition (3DFD), a direct RP technique, for fabricating 3D Ti6Al4V scaffolds with regular and reproducible architecture meeting the requirements of TE has been demonstrated. Scaffolds with highly uniform internal honeycomb-like structures, controllable pore morphology and complete pore interconnectivity can be obtained by varying the direction of fiber depositing and the space between the fibers. Results of in vitro studies revealed the biocompatibility of the scaffolds (Li et al. [2006]). Ti6Al4V scaffolds produced by 3DFD have also been used to study the influence of the structural characteristics on the bone ingrowth. In vivo tests were done to study the effect of different porosities, pore sizes and thus different mechanical properties, on the amount of new bone growth. So, the capability to control scaffold architecture variables of the Ti6Al4V scaffolds by using 3DFD was demonstrated (Li et al. [2007]).

The present project focuses on Ti6Al4V scaffolds produced by a direct RP technique namely selective laser melting, SLM. Fig.2.2 shows a typical example. The starting point for SLM, as for all generative manufacturing processes, is a three-dimensional (3D) model generated by a CAD, which is subdivided into

layers of a definite thickness. The actual part is generated by a repeating process of applying new material layers and transferring the area and contour information of each layer into the material using a laser beam (Hollander et al. [2003]). The physical process is a complete bonding between the layers yielding densities of approximately 100% in one step.

Successful fabrication of biocompatible 3D bone substitutes made of Ti6Al4V with different surface properties within few hours by SLM has already been reported. As this titanium alloy is a biologically approved and well-described prosthetic material, only the physical surface properties derived from manufacturing the scaffolds by SLM could potentially influence cellular growth (Hollander et al. [2003]). Nevertheless, it was proven they were compatible with human primary osteoblasts, thus, the scaffolds produced by SLM are biocompatible.

Since RP techniques have a limited resolution, variability on the produced geometry is introduced. This variability may be relatively large, especially when the feature dimensions within the microstructure are near the physical production limits. In the case of applications such as tissue engineering, designing near the physical production limits makes sense as this allows e.g. improving the contact surface area between biological tissue and scaffold. That is, it has to be taken into account that the ultimate goal is the scaffold to be implanted and cells to grow in it, which demands to work close to the physical production limits. That is why although biocompatibility has been extensively checked, the mechanical properties of porous Ti6Al4V scaffolds produced by SLM still need to be assessed. Also the morphological characterization will be very useful to see how accurate and robust the production technique is. The CAD model can serve for example as an input for Finite Element Analysis (FEA) of which the aim is to be able to predict the behavior of a material when subjected to any stress. As there may be differences between the CAD model and reality, the FE modeling will be improved with the data obtained from the morphological and mechanical characterization. When the FE model is capable of simulating reality, it will be a reliable source of what would be the best design to meet certain engineering, medical and biological requirements. That best design could then be converted into a CAD design and fabricated.

The previously described design loop is subject of a recently approved OT-project. The flow chart of the overall project and the contributions of the present study to that work are demonstrated in Fig.2.3.

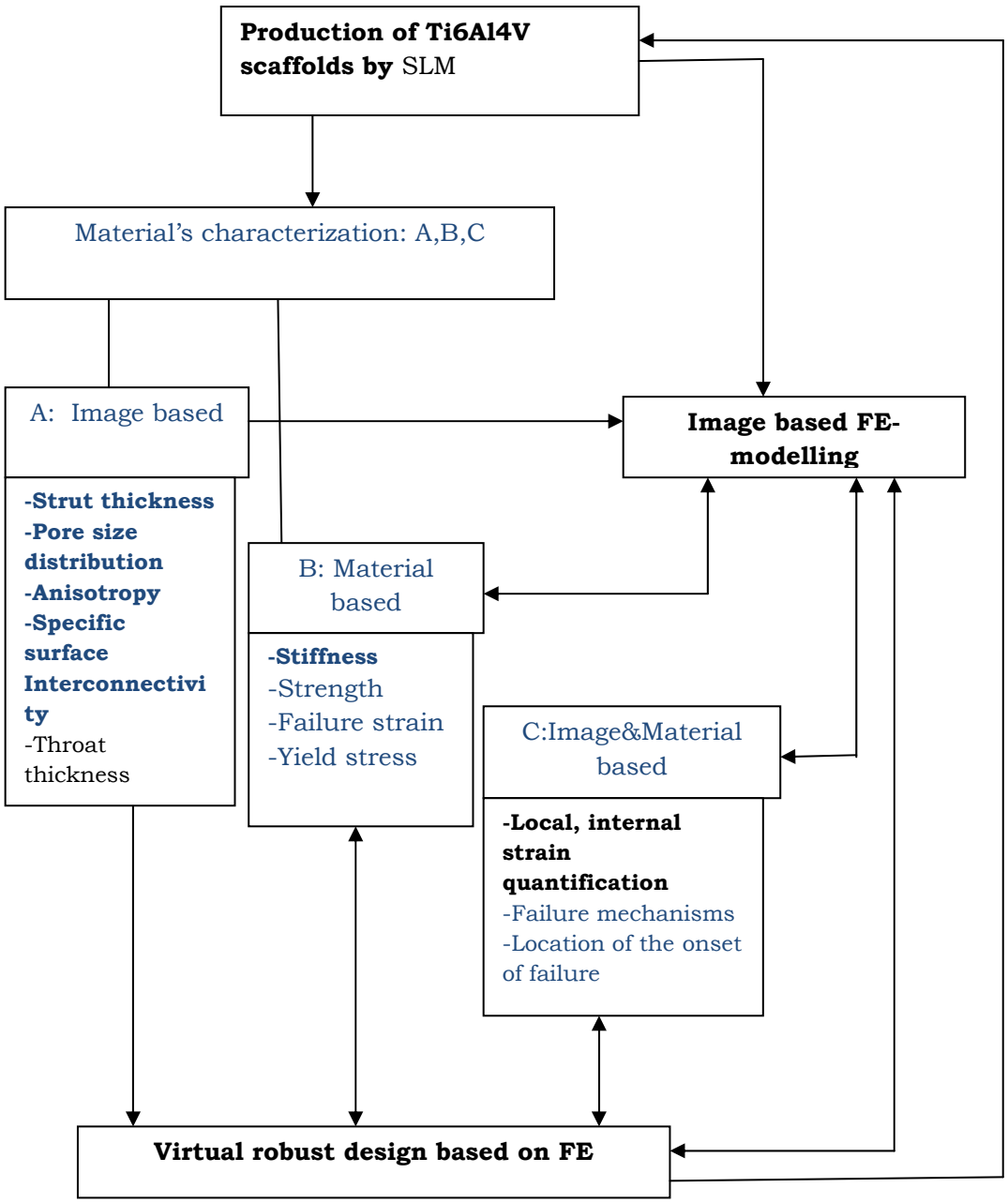

Fig.2.3. Flow chart of the overall project in which the parts the present work dealt with are highlighted in blue.

2.3. Characterization techniques

As been said, both the morphological and mechanical properties of the RP Ti6Al4V bone scaffolds will be assessed by the combination of micro-CT, image analysis and in-situ loading. Micro-CT is a relatively young imaging technique for characterizing porous materials that visualizes the 3D, internal structure of objects in a non-destructive way, with a resolution that can be as low as 1μm. Micro-CT itself provides a high-resolution 3D map of the X-ray absorption coefficient μ of the material. This enables to visualize the microstructure and to analyze it qualitatively but can also be the starting point for quantitative 3D image analysis. The combination of micro-CT with 3D image analysis techniques enables an extensive quantitative description of the microstructure of porous materials that cannot be obtained by other methods

(Benouali et al. [2005]). It has been stated that micro-CT is a particularly suitable technique for internal investigation and quality control of metal foams. Nevertheless, micro-CT also has its limits. Due to the limited resolution, details below 1μm cannot be visualized. Besides, if the intensity of the attenuated X-rays does not differ much from the initial intensity before passing through the material or when almost all X-rays are absorbed, the structure of the material cannot be visualized. The first is more common for low density materials such as polymers, while the second only happens for dense metals or ceramics. The non-invasive character allows further testing and analysis after or while scanning.

Mechanical testing of porous materials is the prerequisite for any structural application. Compression tests are widely used, providing useful information such as Young's modulus (E), the ultimate compressive strength (σ_{ucs}) and the strain at ultimate compressive strength (ε_{ucs}), and are very suitable for materials such as RP Ti6Al4V which have a scattered behavior in tension. Therefore, the combination of micro-CT and mechanical testing might be the way to go for characterization of TE scaffolds.

Micro-CT and compression tests have been used in a combined way several times to study the mechanical behavior of different porous or cellular materials. As it can be read below, the combination of both allows a very thorough study of the relationship between morphology, mechanical properties and fracture behavior in porous materials. Nevertheless, stepwise loading is the way to analyze the evolution of a material under stress, and it cannot be forgotten that its behavior may differ from continuous loading.

The mechanisms of compressive deformation that occur in both open cell and closed cell aluminium alloys were established in Ref. (Bart-Smith et al. [1998]). It was achieved by using X-ray CT and surface strain mapping to determine the deformation modes and the cell morphologies that control the onset of yielding. The specimen surface was sprayed with paint to enhance the speckle pattern for strain mapping and the compression device was not located inside the CT machine. It was concluded that the cell morphologies that dictate yielding appeared to be shape dominated, which makes improvement of the mechanical properties through control of the cells during manufacture to be particularly challenging. The latter could be achieved by SLM, as seen in previous paragraphs.

In the case of closed cell porous aluminum, the compressive and damage behavior has also been studied using high-resolution X-ray CT and strain mapping, but using an in situ test rig instead of having to move the sample from the compression device to the CT machine (Ohgaki et al. [2006]). It was found that the microcracks were mainly initiated from the cell walls and that the micropores with large diameters were also damaged. The local strain mapping indicated that the edges of the micropores with large diameters had large strain under compression, which was consistent with the crack analysis.

In Ref. (Dillard et al. [2005]) the deformation and fracture behavior of an open cell nickel foam were analyzed using X-ray micro-CT. A tensile/compression machine was especially designed to allow the observation of deformation and damage by micro-CT. The initial morphology of the foam was studied using 3D image analysis. It was observed that the main deformation mechanisms were the following: bending, stretching and alignment of the struts

in tension; buckling of the struts more or less parallel with the loading direction in compression. Strong strain localization was observed in compression, whereas, in tension, deformation of nickel foams remained quite homogeneous before the initiation of final cracks.

Also trabecular bone has been the object of many studies concerning micro-CT and mechanical testing.

Ref. (Nagaraja et al. [2005]) assessed the local trabecular bone deformation and damage under varying levels of uniaxial compression via micro-CT in combination with sequential fluorescent staining. Specimens were stained prior to mechanical testing to label preexisting microdamage, and after mechanical testing, with a different stain, to label microdamage incurred from mechanical testing. Micro-CT images in the undeformed state (0% strain condition) were used to create 3D high-resolution FE models for estimating the local stress and strain distributions. By this method, it was demonstrated that there is a direct relationship between 3D trabecular microstructural stress and strain concentration and local damage events. Besides, it was stated that the incremental loading protocol did not significantly affect the measured stiffness or failure properties relative to continuous loading. It was not the first report that stated stepwise compression to be comparable to classical continuous testing for trabecular bone(Nazarian et al. [2005]) ((Nazarian and Muller [2004]) (Muller et al. [2002]). Whether the same applies to RP Ti6Al4V scaffolds still remains a question.

In Ref.(Nazarian and Muller [2004]) stepwise microcompression in combination with time lapsed micro-CT imaging was used to analyze dynamic fracture progression of trabecular bone. Following the application of each strain step, the specimens were allowed to relax for 20 min prior to its transfer to the micro-CT for imaging, in order to establish an appropriate time interval for specimens to reach a plateau for stress relaxation.

Micro-CT in combination with in situ loading allowed visualization and quantification of failure initiation and propagation, that in combination with monitoring of damage accumulation was used to investigate the failure mechanisms of 3D trabecular bone in Ref. (Muller et al. [2002]). In this case, the loading stage was not located inside the micro-CT. And because the sample was removed and replaced from the micro-CT for each of the loading steps, the subsequent micro-CT scans were not consistently aligned in the global coordinate system (defined in the micro-CT). This artifact could be eliminated, but of course, will not even be present when the loading device is located inside the micro-CT. Thus, locating the loading device inside the micro-CT may spare errors derived from transferring the sample from the loading stage to the micro-CT and vice versa.

2.4. Conclusion

As mentioned, the present project will focus on the characterization of Ti6Al4V scaffolds produced by SLM. From the literature, it can be concluded that SLM, a RP technique, is very suitable for scaffold fabrication, since it allows to precisely control pore size, pore geometry, pore interconnectivity, spatial distribution of pores and construction of internal channels within the scaffold. It has also been demonstrated that SLM can produce scaffolds that are

biocompatible. However, it is very important to verify the robustness of the production process in morphological and mechanical parameters, which is one of the objectives of the project. Therefore, the combination of micro-CT imaging, image analysis and in-situ loading will be used, since, as stated in literature, it is a good technique to determine the morphological and the related mechanical properties of porous materials. In order to avoid the problems derived from transferring the sample from the micro-CT to the loading device and vice versa, a novel loading stage was developed in previous work which can be placed inside the micro-CT machine. Of course, the accuracy and reliability of this newly developed device needs to be proven, which is subject of the present project. Moreover, it was stated that there was no difference between continuous and stepwise loading in the case of trabecular bone, which will at present be assessed for the case of Ti6Al4V scaffolds produced by SLM.

Robustness of the production technique (SLM), will be studied (i) by comparing the same design produced by two different machines and (ii) by studying the variability within on production batch, produced with the same design and on the same SLM machine. First, bulk samples will be produced by two different machines, which will allow a comparison between the theoretically expected values for the mechanical properties and the ones obtained for each machine. As explained in previews paragraphs, the ultimate goal is the scaffold, which will of course always be porous, to be implanted and cells to grow in it. Therefore, the robustness of both machines will also be assessed for two identically designed porous structures.

Since the newly developed in-situ loading stage for the micro-CT has not yet proven its accuracy and reliability, a comparison to a standard mechanical loading device will be made. Also, in order to correlate the designed, morphological and mechanical properties, and check whether continuous and stepwise loading are different or not for Ti6Al4V SLM produced scaffolds, the same tests will be carried out on scaffolds produced with the same machine and varying pore sizes.

This project is intended to set up a protocol for the analysis of porous Ti6Al4V SLM produced bone scaffolds. The present investigation and further research could then be used to improve the design and FE modeling, to head towards a design that could model a perfect scaffold which meets certain engineering, medical and biological requirements on a production technique of which the relation between input (design) and output (produced scaffold) is completely known. This way, the perfect scaffold could be built.

3. Material

The scaffolds assessed in the present project were produced from Ti6Al4V powder with the characteristics specified in Table3.1. These data should be regarded as indicative since it corresponds to annealed Ti6Al4V, whereas, after SLM, Ti6Al4V will be closer to quenched. In the present project, no tensile but compressive properties will be derived. Nevertheless, the compressive elastic modulus of Ti6Al4V closely mimics the material's tensile elastic modulus (Young's modulus) (Boyer et al. [1994]).Moreover, under any heat treatment conditions, the compressive modulus will just slightly exceed the tensile Young's modulus.

Table3.1. Specifications of the Ti6Al4V powder.

Density	4.42 g/cm³
Max. Tensile Strength	1000 MPa
Tensile Strength at 0.2% deformation	920 MPa
Max. Strain	12%
E modulus	110 GPa
Melting point	1649°C
Average Grain Size	35 μm

Three designs of porous RP Ti6Al4V scaffolds and some bulk samples were produced, as shown in Table3.2. More information about the different production machines is given below.

Table3.2. Characteristics of the designs produced for the present project.

	Designed pore size (mm)	**SLM machine**
s0.1p0.8	0.8	LM
s0.1p1	1	LM
s0.1p1Concept	1	Concept
s0.1p1.2	1.2	LM
BulkLM	0	LM
BulkConcept	0	Concept

The three porous designs and the bulk samples were fabricated from the same powder and with the same technique (SLM), unit cell (Fig.3.1) and characteristics, except for the pore size, which was the only variable. Radiographic images of one sample per design can be seen in Fig.3.2, Fig.3.3 and Fig.3.4. The designed strut diameter was 0.1 mm. All cylinders had a radius of 3.00 ± 0.05 mm and a height of 12.0 ± 0.5 mm.

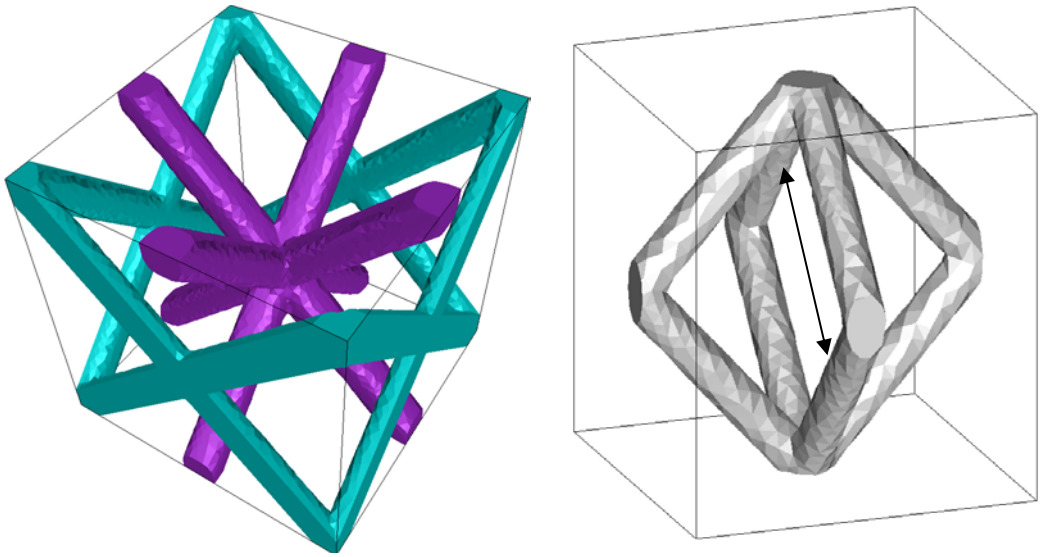

(a) *(b)*

Fig.3.1. *(a)* unit cell of the bone scaffold. *(b)* simplified unit cell of the bone scaffold in which the designed pore diameter is defined by an arrow.

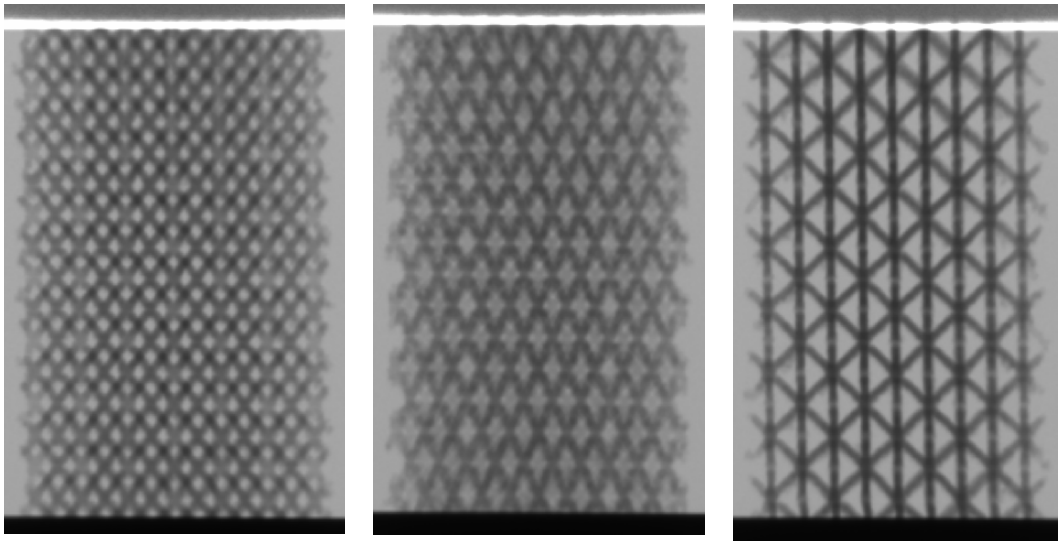

Fig.3.2.Radiographic images of a sample of design s0.1p0.8.

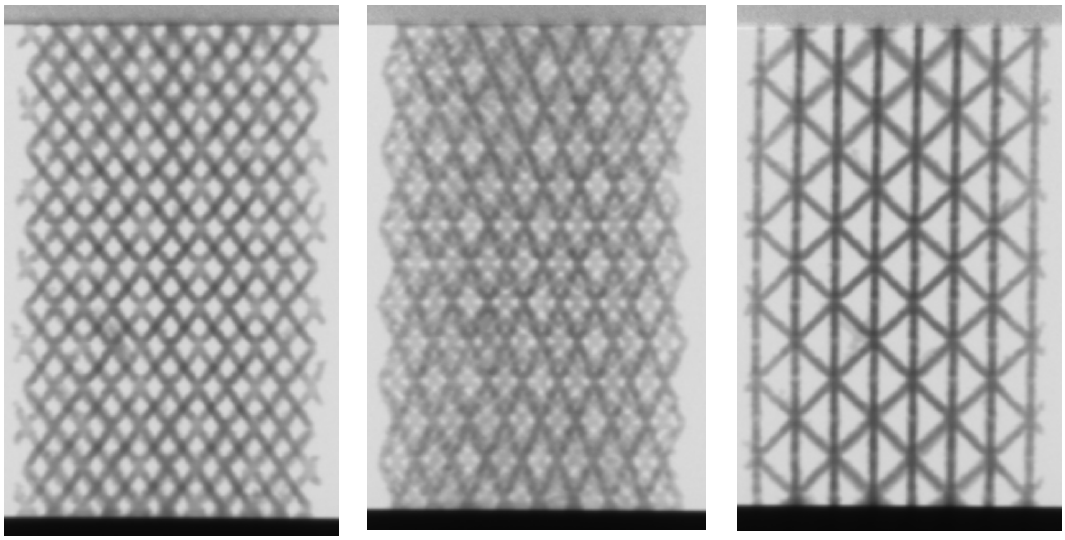

Fig.3.3. Radiographic images of a sample of design s0.1p1.

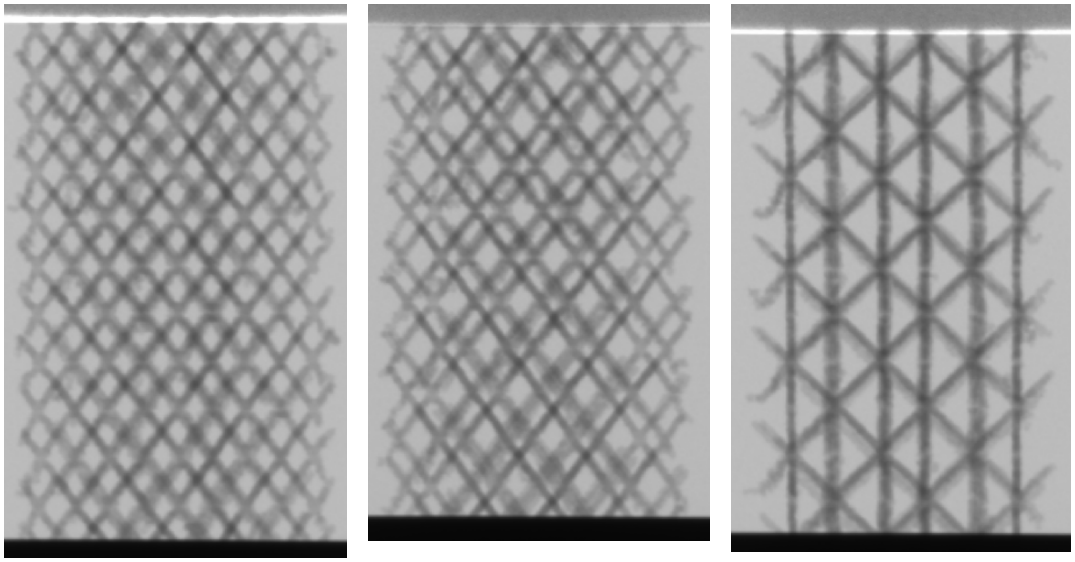

Fig.3.4. Radiographic images of a sample of design s0.1p1.2.

The starting point for SLM, as for all RP techniques, is a 3D model generated by CAD, which is subdivided into layers of a definite thickness. The actual part is generated by a repeating process of applying new material layers by moving the built cylinder down in the Z-axis, flattening the new powder layer with a roll and transferring the area and contour information of each layer into the material using a laser beam as outlined in Fig.3.5. In this study, the scaffolds were built on top of a plate that acted as a support from which the scaffolds were removed by wire electrical discharge machining. Fig.3.6 shows a typical porous RP Ti6Al4V porous scaffold produced by SLM.

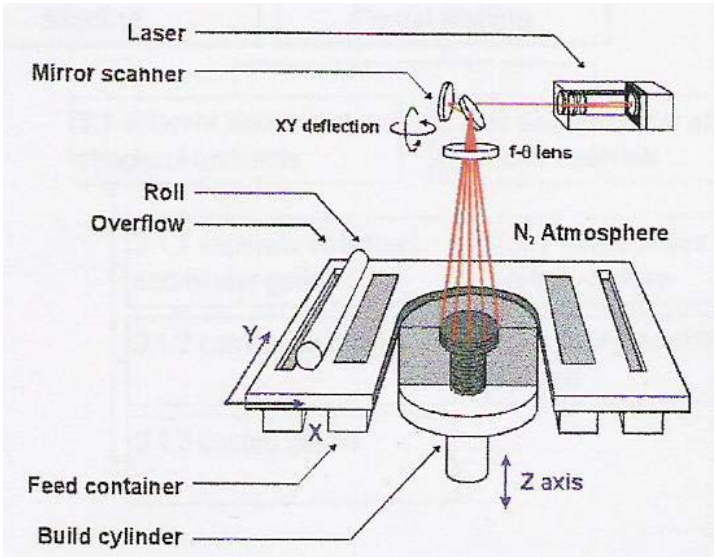

Fig.3.5. Schematic overview of the SLM process (Kruth [2003]).

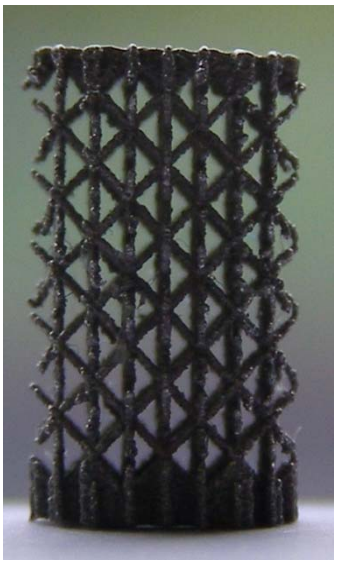

Fig.3.6. Ti6Al4V porous scaffold produced by SLM.

In the present project, two different machines, LM (Fig.3.7) and Concept (Fig.3.8), were applied to produce the bulk structures and the porous ones of a designed pore size of 1 mm. The technical details of LM and Concept can be seen in Table3.3.

Table3.3. Technical details of LM and Concept, SLM machines.

	LM	**Concept**
Laser	Yb: YAG	ND-YAG
Mode	continuous	continuous
Wavelength (nm)	1085	1064
Spot size (μm)	80	80/200
Scan speed (mm/s)	260	150
Power	39 W	25 W

The scaffolds and structures produced by Concept were built with a laser spot size of 80 μm, thus, the same as the LM one.

Fig.3.7. Concept SLM machine.

Fig.3.8. LM SLM machine.

4. Archimedes

4.1. Method

The Archimedes tests to define the porosity of the RP porous Ti6Al4V scaffolds were carried out on every sample to be analyzed by micro-CT combined with in situ loading, with a Sartorious YDK 01, YDK 01-0D Density Determination Kit, following Method1. The density of an immersed object relative to the density of a fluid is easily calculated without measuring any volumes, thanks to the relation expressed in eq. (4.1), in which all the variables are measured in the laboratory, being the density of the sample the only unknown.

$$\frac{DensitySample}{DensityFluid} = \frac{Weight}{Weight - ApparentInmersedWeight} \qquad \text{eq. (4.1)}$$

4.2. Experimental results and discussion

The aim of carrying out Archimedes test on the porous RP Ti6Al4V scaffolds was to know their porosity, which is summarized in Table4.1.

Table4.1. Results from Archimedes testing. (n=5)

	Porosity (%)
s0.1p0.8	85.28 ± 0.49
s0.1p1	88.13 ± 0.10
s0.1p1Concept	89.76 ± 0.08
s0.1p1.2	92.24 ± 0.15

Even though the design parameters for s0.1p1 were the same for LM and Concept, it can be seen that the outcome differs. This can be due to the rougher surface of the Concept samples. For the rest, the results show, as expected, that the porosity increased when the designed pore size increased.

4.3. Conclusion

The results from the Archimedes test were used to define the optimal threshold for the reconstruction of the images obtained via micro-CT (Ding et al. [1999]). Moreover, the porosity calculated by Archimedes was used as a physical reference to verify whether the data acquired by means of micro-CT was correct or not.

5. Microscopy

5.1. Method

One sample per design was analyzed by microscopy. Each sample was cut into three slices named top, middle and bottom. The following steps were followed for the microscopic analysis:

1. Measuring the dimensions of the samples with an electronic caliper.

2. Embedding of samples in resin.

   The cylindrical samples of height 12 mm and diameter 6 mm were put into a cylindrical polyethylene mould of diameter 25 mm and height 20mm, to be embedded in transparent resin. Self-curing resin was prepared by mixing 15ml Epofix Resin (Struer, Denmark) with 2ml of Epofix Hardener (Struer, Denmark). In order to make the bubbles created during the mixing of the resin disappear, the samples already embedded in self-curing resin were introduced in a vacuum diseccator (800mbar) at the temperature of 24^{o}C for 24 hours. After 24 hours the embedded samples were removed from the polyethylene mould.

3. Cutting, grinding and polishing of the samples.

   Each sample was cut with a microtome into three slices. Afterwards, the part of each slice that was analyzed with the microscope was grinded and polished.

4. Microscopy: photographing the polished surface.

   20 to 24 images of each sample surface were taken at the lowest magnification (PL 8x1), with a light optical microscope (Metalloplan, Germany) on which a CCD camera was assembled.

5. Stitching and binarizing of pictures.

   The reconstruction of each surface was made from the 20-24 pictures taken for each surface, by using Panavue Image Assembler, a digital image stitching software (http://www.panavue.com). They were converted to 8 bit images using Corel PHOTO-PAINT X3 in order to be able to binarize them using CTAnalyzer [Skyscan NV, Kontich, Belgium].

5.2. Experimental results and discussion

The aim of taking microscopic images was, at first, to run 2D analysis on them and to compare the results to those obtained by 2D analysis on the micro-CT dataset. This way, the microscopic images would serve as a physical reference. For the comparison to be valid, the analysis should have been done on a micro-CT in the same plane as the physical cutting plane. However, it was unfeasible to relate the height on which the microscopic section was taken with a slice in the micro-CT dataset, since the difference between the micro-CT slices was so small due to the regularity of the analyzed structures. One microscopic image per batch is shown in Figs.5.1, 5.2, 5.3 and Fig.5.4.

Fig.5.1 and Fig.5.2 state that there was a difference between the outcome of LM and Concept machines. The surface finish seemed to be smoother for the LM processed scaffold than for the Concept processed one. The settings for both machines, including the spot size were the same. However, power of the laser of LM machine was higher than the one of Concept, which resulted in a better melting of the powder and, therefore, in a better surface finish.

It can be observed in Figs.5.1, 5.3 and Fig.5.4 that the difference in the designed pore size can be noticed from the microscopic images.

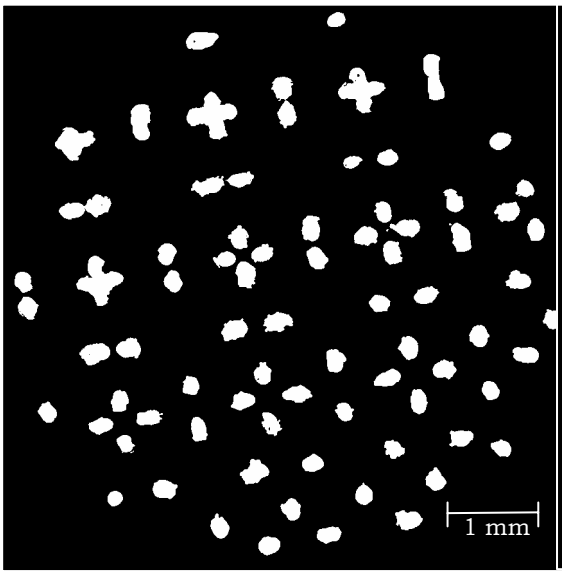

Fig.5.1. Microscopic image of a slice of s0.1p1 (designed pore size 1 mm) scaffold.

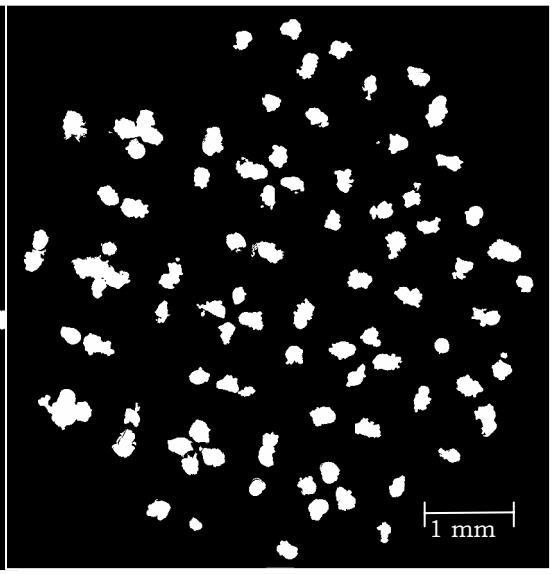

Fig.5.2. Microscopic image of a slice of s0.1p1Concept (designed pore size 1 mm) scaffold.

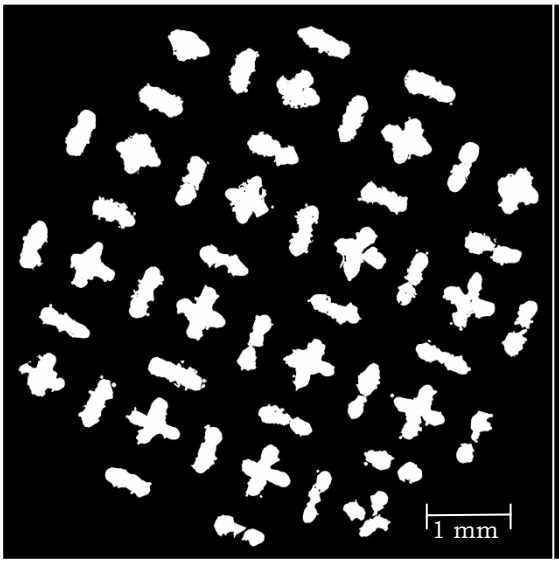

Fig.5.3. Microscopic image of a slice of s0.1p0.8 (designed pore size 0.8 mm) scaffold.

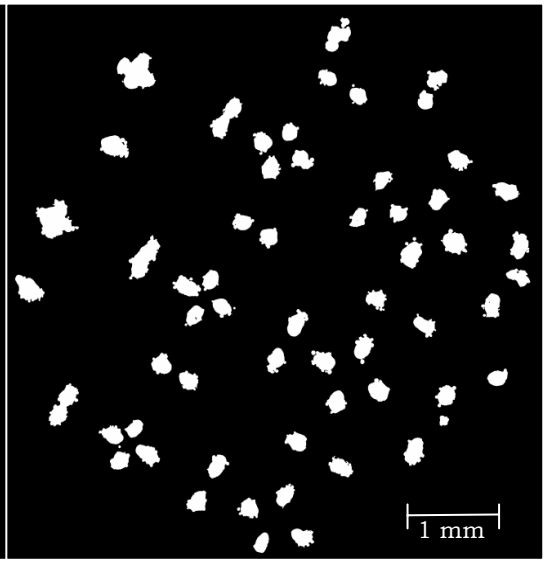

Fig.5.4. Microscopic image of a slice of s0.1p1.2 (designed pore size 1.2 mm) scaffold.

5.3. Conclusion

The matching of the optical images with the micro-CT images of the same cross-section in order to define validation criteria could not be done. However, the optical images showed that LM processed porous Ti6Al4V scaffolds had a smoother surface than the Concept processed ones. Besides, it was stated that a different pore size in the design gave a different output, thus, designed pore size is a parameter that can be controlled.

6. Microhardness

6.1. Method

Microhardness tests were carried out on the samples that were previously analyzed by microscopy, which means that the preparation for the hardness tests was the same as for microscopy.

Several Vicker's microhardness measurements were taken for one sample per design, on its different slices (top, middle and bottom) using a Leitz Durimet with a load of 100 g. The measurements were done via ocular, with the help of a CCD camera.

6.2. Experimental results and discussion

The results of the microhardness tests carried out on the porous Ti6Al4V scaffolds are shown in Table6.1.

Table6.1. Results of microhardness tests on the scaffolds. (n=5)

	Microhardness (HV)
s0.1p0.8	401.28 ± 15.13
s0.1p1	393.92 ± 16.20
s0.1p1Concept	411.93 ± 22.91
s0.1p1.2	403.01 ± 11.23
Theoretical (Annealed)	349

The experimental results showed a value of hardness significantly higher than the theoretical one for annealed Ti6Al4V. The microstructure of titanium alloys is strongly influenced by the processing history and heat treatment, as shown in Fig.6.1. The scaffolds produced by SLM are closer to quenched than to annealed due to the rapid cooling, when laser is not longer applied, during the process. The presence of martensite was corroborated by microscopy. Fig.6.2. shows the martensitic structure.

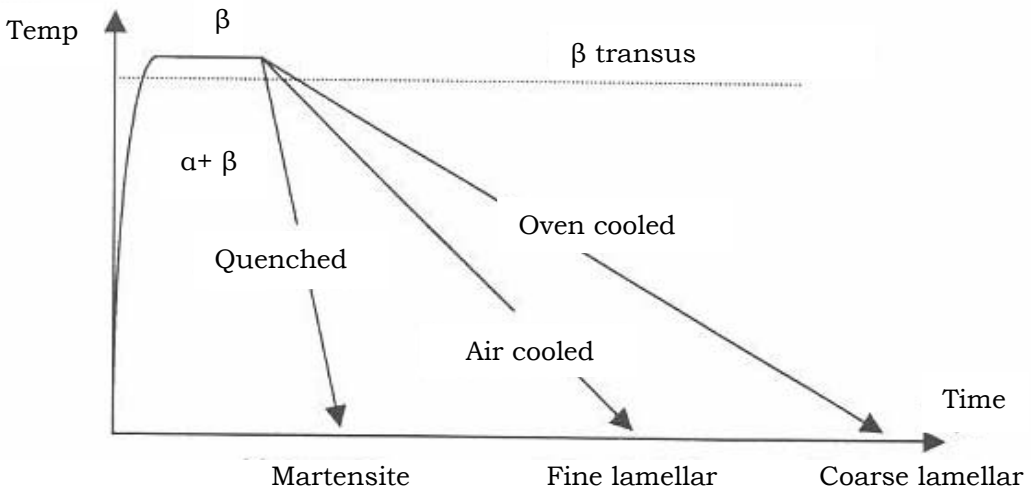

Fig.6.1.Lamellar α-structure (transformed β) of Ti6Al4V as function of the cooling rate (Schrooten [1999]).

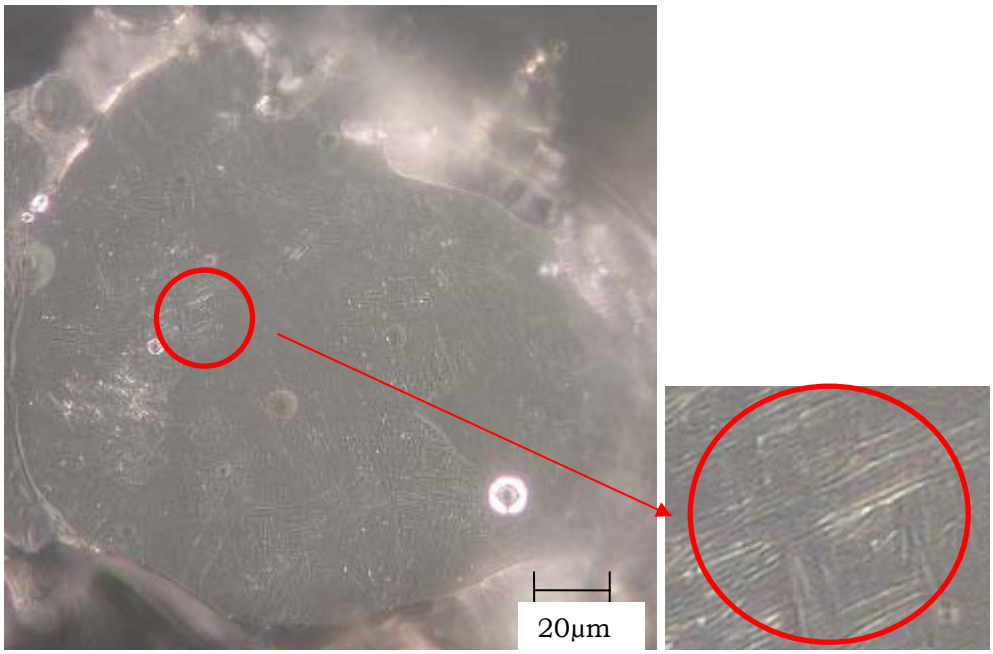

Fig.6.2. Microscopic image of one strut with martensitic structure highlighted by red circle.

An Anova test for three populations reflected, with a p-value of 0.19, that the there was no significant difference between the hardness values of the LM produced scaffolds. Thus, the hardness of the scaffolds produced by LM was totally independent from the design and production variables studied in the present project.

An Anova test for four populations was also carried out including data from s0.1p1Concept, leading to a p-value of 0.03. The fact that the p-value is lower than 0.05 means that at least one population's mean differs quite significantly from the others. Taking into account that the difference between the first and the second Anova test was the introduction of the data corresponding to the Concept processed scaffolds, it was concluded that the hardness of the Concept produced scaffolds was significantly higher than the LM produced ones. This could be due to the higher presence of oxygen in the processing with Concept machine, which leaded to the formation of titanium oxides on the surface, which are harder than Ti6Al4V.

6.3. Conclusion

The presence of a martensitic phase due to the quenching during the production process resulted in hardness values higher than the theoretical for annealed Ti6Al4V.

From the microhardness tests it was concluded that the hardness of the scaffolds produced by LM did not depend on the variables studied in the present project, thus, was independent from the strut diameter and the designed pore size. This indicated that the process was robust and had high repeatability concerning production variables, such as oxygen content of the atmosphere, which directly affect hardness.

Concept produced scaffolds were significantly harder than the LM processed ones, due to the formation of titanium oxides because of the higher presence of oxygen during the processing of the scaffolds.

7. Mechanical testing

7.1. Method

7.1.1. Instron 4505

Continuous compression tests were carried out on the Instron 4505 on both bulk and porous structures. Technical details of the machine can be read in Table7.1.

Table7.1. Technical details of Instron 4505.

Speed range	0.0005 - 1016 mm/min
Max. travel	1330 mm
Clearance between columns	575 mm

For both the bulk and porous scaffolds the compression tests were carried out at the test speed of 0.15 mm/min and the smallest possible preload, which could not always be the same since it had to be manually applied by inducing some displacement. The only difference was that a 100 kN load cell was used in the case of the bulk structures and a 5 kN one for the porous ones.

7.1.2. In situ loading stage

The in situ loading stage was placed inside the micro-CT, as shown in Fig.7.1.The X-ray source of the micro-CT can be seen in the picture.

Fig.7.1. In situ loading stage placed inside the micro-CT, of which the X-ray source can be seen.

Continuous, cyclic and stepwise tests were carried out at the in situ loading stage (Fig.7.1. and Fig.7.2.), on porous structures of every design; thus, s0.1p0.8, s0.1p1, s0.1p1Concept and s0.1p1.2. Characteristics of the loading stage are summarized in Table3.5.

For the continuous loading tests a speed of 0.2 mm/min and a preload of 0.01 kN were applied. The tests were load controlled.

For the cyclic testing 10 cycles (20 steps) of compression and release were applied to one sample per design, at a speed of 0.2 mm/min, a step size of 0.25 mm displacement and a preload 0.01 kN, being the tests displacement controlled.

The stepwise tests were performed at a speed of 0.2 mm/min, a step size of 0.2 mm displacement (6-7 steps per sample) and a preload of 0.01 kN was applied. The tests were displacement controlled.

Table7.2. Technical details of the in situ loading stage.

Crosshead speed (mm/min): 0.0014 - 12.5
Exchangeable "Sensy" load cells (30kN ± 30 N, 3 kN ± 1N , 100 N ± 0.02 N)
Max sample size: cylinder of 5 cm diameter and 5 cm height
Deformation rate between 0.005 en 5 mm/min
Load or displacement control
Control of relaxation

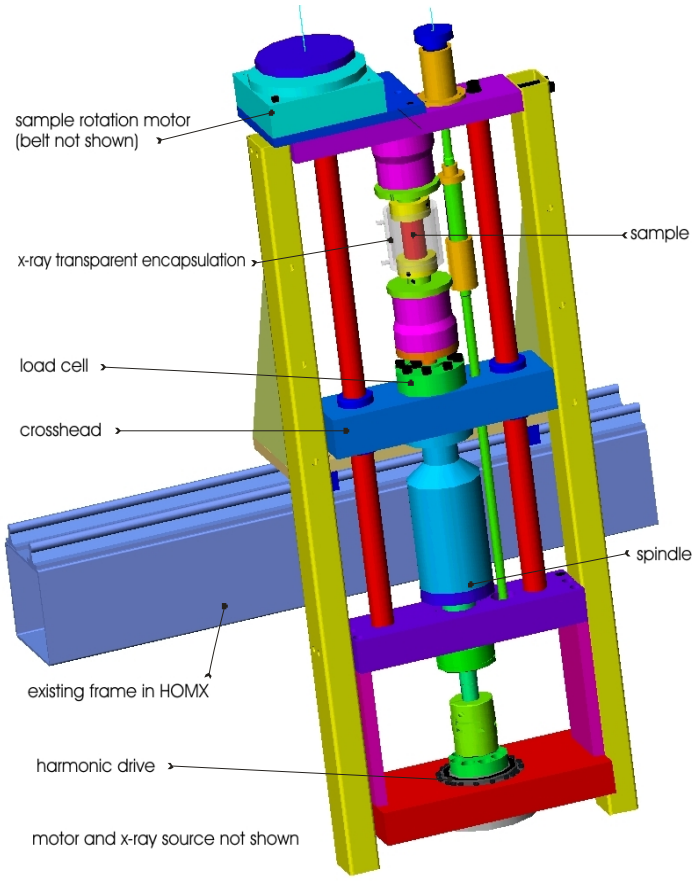

Fig.7.2. Schematic overview of the in situ loading stage.

7.2. Experimental results and discussion

It was already said that mechanical testing is a prerequisite for any structural application. In the present project, compression and cyclic tests were chosen to be carried out in order to mechanically characterize the porous Ti6Al4V scaffolds, since it is well known that metallic materials such as Ti6Al4V have a more stable and less scattered behavior in compression than in tension. Besides, the final application of the assessed scaffolds will to substitute damaged bones, which means that they will be subjected to cyclic loading (fatigue). Therefore, preliminary analysis was done in that field, by cyclic testing the scaffolds.

In both testing cases, the following three parameters were analyzed for each sample.

1. **E** (MPa), Young's Modulus.

   The assessed structure has a nonlinear elastic behavior, which means that Hooke's law cannot be applied to derive the E-modulus. This makes it difficult to calculate a single E modulus for the assessed structures, thus, the method used in Ref. (Kinney et al. [2001]) to calculate the E modulus of elastomeric foams with a highly nonlinear behavior was applied.

   The procedure goes as follows:

   I. A fourth order polynomial was fitted to the stress-strain curves between the first point and the ultimate compressive strength (Fig7.3).

   II. The derivative of the polynomial was plotted where the E modulus was expressed in function of the strain.

   III. The maximum of the graph described above was assumed to be the E modulus (Fig.7.4).

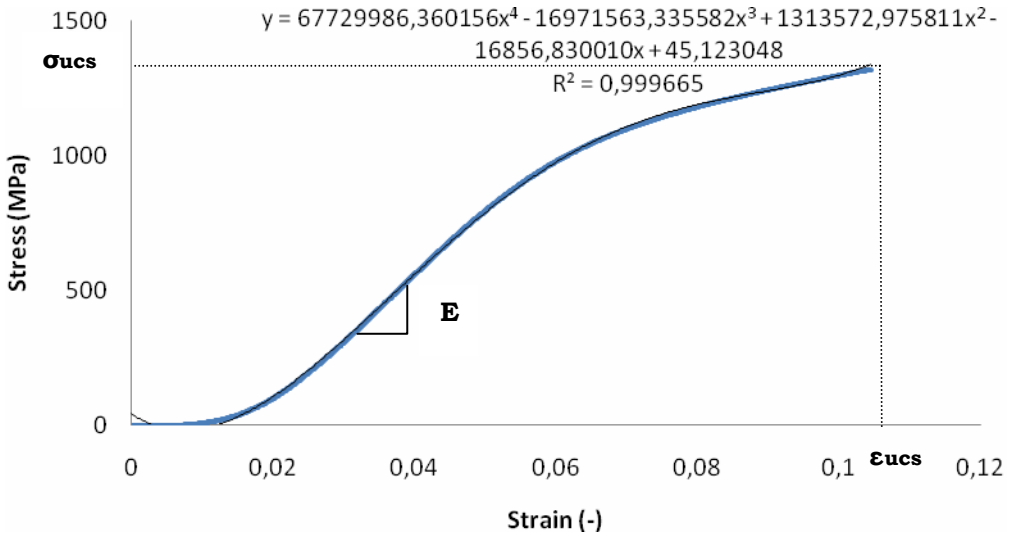

Fig.7.3. Stress-strain curve on which a fourth order polynomial has been fitted.

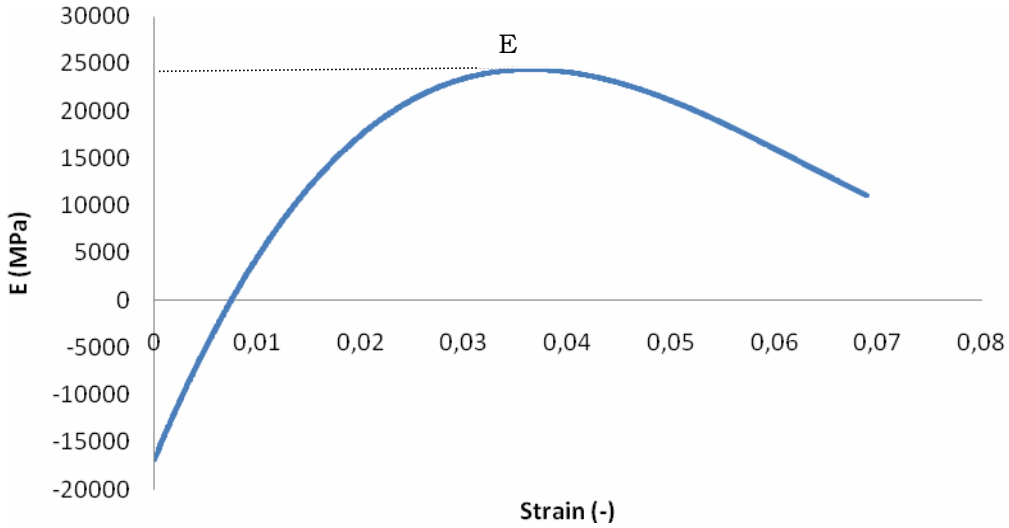

Fig.7.4. Graph of the variation of E with the strain of which the maximum is assumed to be the E modulus of the tested sample.

The reason the E modulus might be negative in the beginning of the Variation of E curve is that the polynomial did not fit the first part of the stress strain curve, in which the setting of the sample took place.

2. σ_{ucs} (MPa), ultimate compressive strength.

3. ε_{ucs}, strain at ultimate compressive strength.

7.2.1. Bulk scaffolds

The aim of testing bulk scaffolds in compression was to compare the experimental results with literature to be aware of the difference that may exist between theory and practice when producing the scaffolds by SLM, as well as to make a comparison between the two different SLM machines, LM and Concept.

For that, 3 BulkLM and 3 BulkConcept samples were tested in compression on the INSTRON 4505 assuming that the displacement of the samples was the one measured by the Instron. Table7.3 shows the results while Fig7.5 shows a typical graph for two bulk Ti6Al4V scaffolds, one made with LM machine and the other made with Concept.

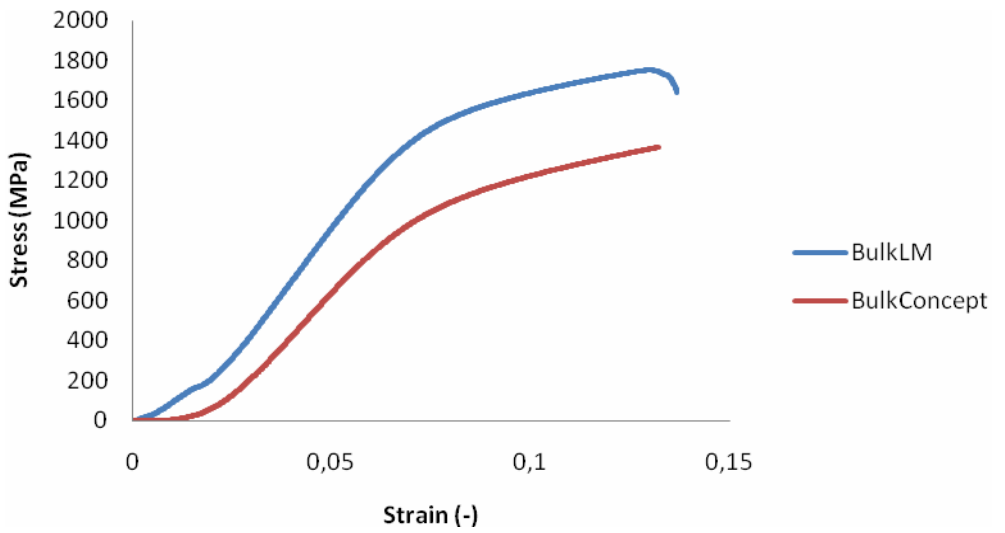

Fig.7.5. Stress-strain curves for a bulk scaffolds produced by LM and Concept measured by the Instron.

Table7.3. Results from the compression tests with Instron on bulk scaffolds. (n=5)

	E (GPa)	σ_{ucs} (GPa)	ε_{ucs} (%)
Bulk LM	26.04 ± 0.24	1.77 ± 0.031	13.9 ± 1.3
Bulk Concept	19.07 ± 1.73	1.54 ± 0.045	20.0 ± 1.0
Theoretical	113.8	-	-

The results showed a significant difference between theoretical and experimental values, as well as between values corresponding to the scaffolds manufactured by LM and Concept.

The theoretical value is the one for Titanium Ti-6Al-4V (Grade 5), Annealed, the powder from which the scaffolds were produced. Nevertheless, it has to be taken into account that the alloy will no longer be annealed after the production process; it will be closer to quenched, due to the fast cooling after the melting by laser. Besides, it is not known what criterion has been chosen to obtain the theoretical value of the E modulus. For these two reasons, the theoretical value has only been considered as a reference to have an idea of the range in which the experimental value should be, but never as an accurate measurement of what it should be.

Another reason for the experimental values to only reach around the 20% of the theoretically expected values was thought to be that the stiffness of the sample was higher than the stiffness of the clamps of the Instron, which would lead to an incorrect measurement of the displacement of the clamps. When this happens, the machine is said to be "soft", which means that the displacement it measures will always be higher than the real one, because the clamps are the ones that deform instead of the sample that incrusts in the clamps.

In order to verify whether the problem was that the machine was "soft", it was decided to test three more BulkLM samples while using Limess, an optical system for 3D deformation and strain measurements. However the samples could only be tested until around 35 kN which is lower than the ultimate compressive load, since the samples "exploded" when fracture occurred and the

risk of damaging the optical system could not be taken. Thus, the results of the tests were only used to verify the "softness" of the machine.

The results showed that there was a significant difference between the displacement measured by the Instron and the one measured by Limess, as can be seen in Fig.7.6.

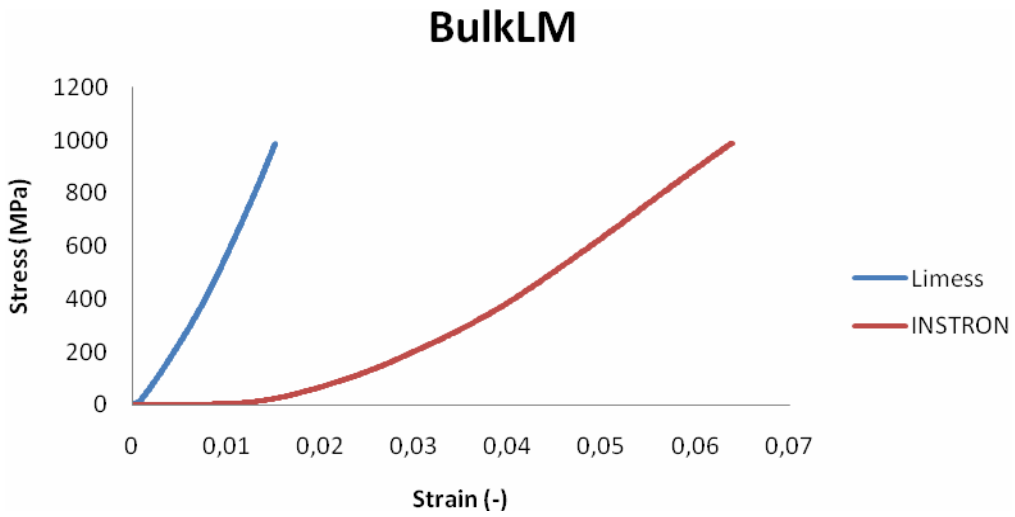

Fig.7.6. Comparison between the stress-strain curves built with displacement data from Instron and Limess in the same compression test for a BulkLM sample.

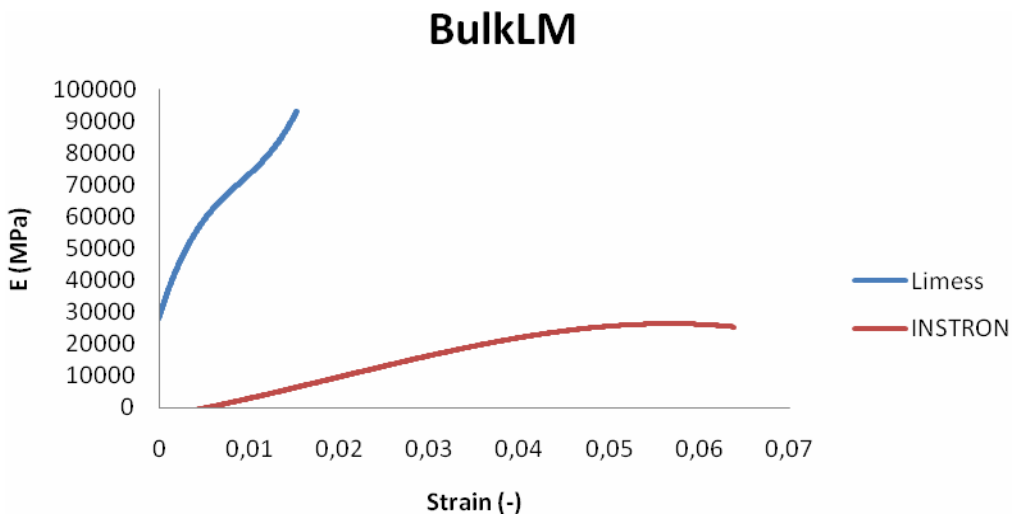

Fig.7.7. Comparison between the variation of E with displacement data from Instron and Limess in the same compression test for a BulkLM sample.

The graph corresponding to the variation of E by Limess in Fig.7.7 shows that if the test would have been carried out longer, the E modulus would have continued increasing, getting close or even exceeding the theoretical value. Nevertheless, as said before, it was not possible to carry out the tests for larger load values.

Limess is an optical system that tracks the displacement of some manually chosen points in the sample by using two cameras. The bulk Ti6Al4V scaffolds had a very homogeneous surface in which associating points from the images of the different cameras was difficult. In order to make the identification easier the scaffolds were painted with black and white sprays, which made it possible to use Limess for the bulk samples even though the overlapping surface of the two cameras was very small. However, it would never be feasible to use this system on the porous samples because of their small strut size and, thus, the small surface on which the tracking of points could be done.

All those facts suggested that Limess could only be used as an indicative tool that had been useful to verify that Instron was not measuring the correct displacement of the sample.

For further research and testing it was decided to use an extensometer when testing samples with the Instron and, in order to find a correction factor for the bulk samples that had already been tested, 2 more BulkConcept and 3 more BulkLM samples were tested. Fig.7.8 and Fig7.9 show a comparison between the stress-strain curves built with displacement data from Instron and the displacement data from an extensometer for BulkLM and BulkConcept.

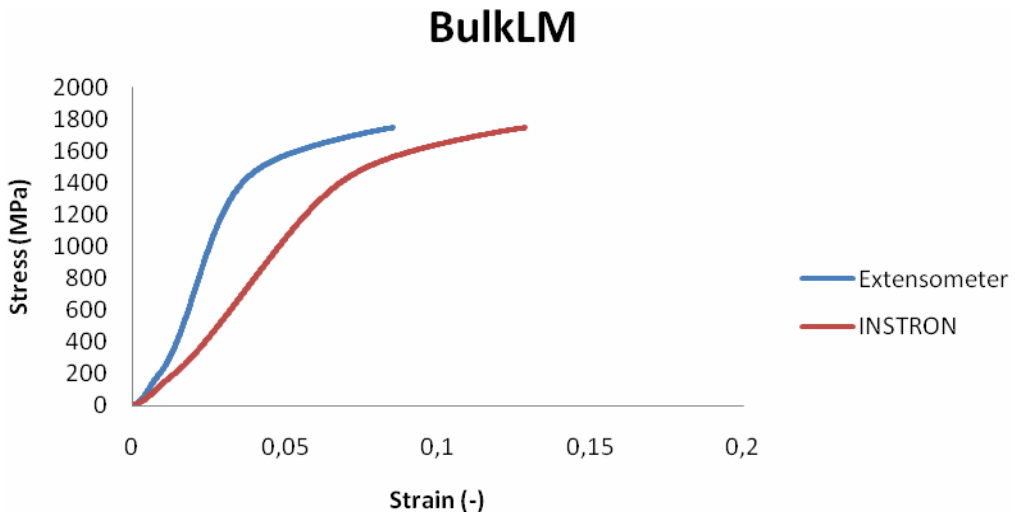

Fig.7.8. Comparison between the stress-strain curves built with displacement data from Instron and the displacement data from an extensometer in the same compression test for a BulkLM sample.

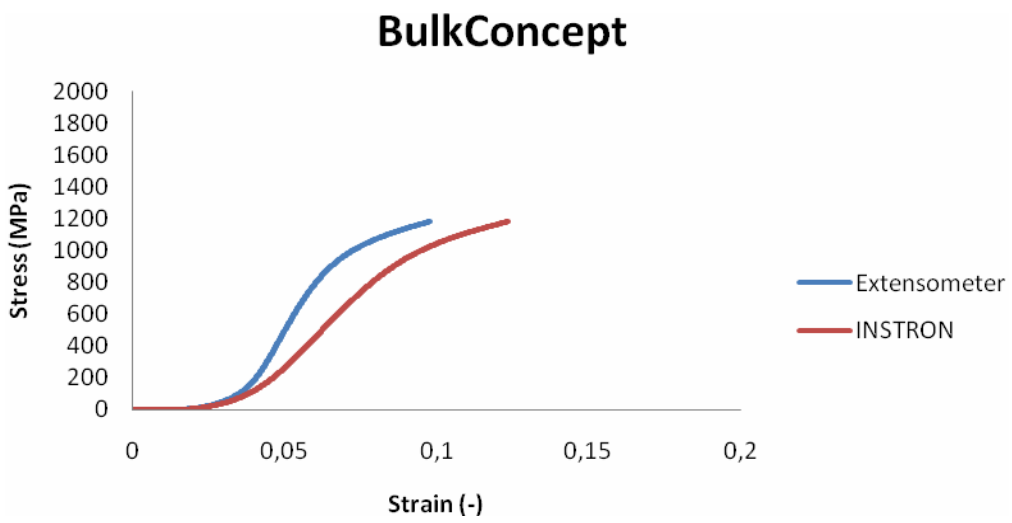

Fig.7.9. Comparison between the stress-strain curves built with displacement data from Instron and the displacement data from an extensometer in the same compression test for a BulkConcept sample.

Assuming there was a difference in the compression behavior of the samples depending on whether they were LM or Concept manufactured, two correction factors, one for each case, were calculated. For the determination of the correction factor the strain according to the Instron vs. strain according to the extensometer was plotted for each tested sample. Then, a linear trend line was fitted to each graph. The mean slope for the BulkLM samples was considered to be the correction factor for the BulkLM. The correction factor for BulkConcept samples was calculated in a homologous way. Table7.4 summarizes the correction factors.

Table7.4. Correction factor.

	Correction factor
BulkLM (n=3)	1.395
BulkConcept (n=2)	1.158

The correction factor was consistent with the results, which showed that the LM manufactured scaffolds were stiffer than the Concept manufactured ones.

The data from the samples tested with and without extensometer, taking into account the correction factors, were joined and Table7.5 summarizes the results.

Table7.5. Results from the compression tests with the Instron and displacement measured by an extensometer on bulk scaffolds. (n=5)

	E (GPa)	**σ_{ucs} (GPa)**	**ε_{ucs} (%)**
BulkLM	42.37± 5.66	1.77 ± 0.031	10 ± 0.9
BulkConcept	24.62 ± 3.82	1.54 ± 0.045	17.9 ± 1.1
Theoretical (Annealed)	113.8	-	-

The results from the compression tests with the Instron on the bulk samples showed that the mechanical performance of the LM manufactured

scaffolds was better than that of the Concept manufactured, even though the design was the same in both cases and both machines work according to the same production technique. The production parameters were set the same for both machines. However, the power of the laser of LM machine is higher, which leads to a better melting and a better bonding between particles and, therefore, to higher mechanical properties.

Furthermore, the results were far from the theoretical values. The main reasons for that was the presence of 0.5% microporosity on the structures and that bonding of the particles might only be partial via SLM. Thus, 42.37 GPa was then assumed as the correct E modulus of the bulk Ti6Al4V structures produced via SLM, while 1.77 GPa was assumed to be the ultimate compressive strength.

7.2.2. Porous scaffolds

7.2.2.1. Compression tests

Porous scaffolds were continuously tested in compression on the Instron as well as on the in situ loading stage. Five samples per design, thus, s0.1p0.8, s0.1p1, s0.1p1Concept and s0.1p1.2 were tested in each loading device. The reason for the samples to have been tested on two different machines is that the in situ loading stage, in which stepwise loading was going to be carried out to allow micro-CT imaging, still needed extra calibration and validation.

The main goal of the compression testing was to gather data about the mechanical properties of the porous scaffolds depending on their designed pore size and to see whether a correlation could be found between mechanical and morphological properties. However, the data obtained from the tests allowed further analysis such as: (i) assessment of the performance of two SLM machines by comparing designs s0.1p1 and s0.1p1Concept, (ii) assessment of the robustness of the production technique by comparing different samples with the same design within one production batch, (iii) comparison of the results obtained from the two loading devices (Instron and the in situ loading stage) to see whether they are significantly different, (iv) comparison of the data from the continuous compression tests with stepwise tests, both carried out on the in situ loading stage.

From previous experience with the bulk scaffolds, it was decided to use an extensometer to measure the displacement of the samples when compressing on the Instron. However, some tests of s0.1p1 and s0.1p1Concept were carried out without extensometer. Being the porous structures less stiff than the bulk ones, the difference between the displacement measurements of the Instron and the extensometer was not expected to be significant. To confirm, two additional compression tests with extensometer were carried out for s0.1p1 in order to calculate a correction factor for the strain for those samples that were tested without it.

For calculating the correction factor, the strain according to the Instron vs. strain according to the extensometer was plotted for each tested sample. Then, a linear trend line was fitted to each graph. The mean slope was considered to be the correction factor, namely 1.021.

The low correction factor is consistent with neglectable difference between the stress-strain curves plotted with the displacement data from Instron and the extensometer, as shown in Fig.7.10.

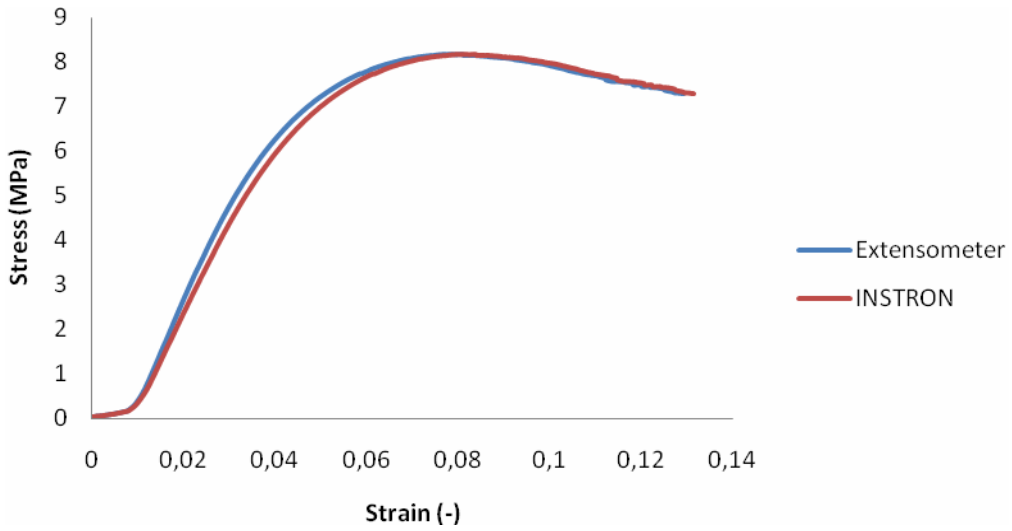

Fig.7.10. Comparison between the stress-strain curves built with displacement data from Instron and the displacement data from an extensometer in the same compression test for an s0.1p1 sample.

Since it was seen that the correction factor for the porous structures was close to 1, compression tests on the in situ loading stage were carried out without extensometer.

The results from the continuous compression tests on the in situ loading stage and the Instron are shown in Table7.6, Table7.7 and Table7.8.

Table7.6. Results from the continuous compression tests with Instron and in situ loading stage for Young's modulus. (n=5)

	Young's modulus (MPa)		
	Instron	**In Situ Loading Stage**	**p-value**
s0.1p0.8	389.68 ± 22.64	369.76 ± 29.83	0.32
s0.1p1	225.56 ± 20.46	237.74 ± 16.40	0.10
s0.1p1Concept	102.09 ± 8.948	101.17 ± 9.08	0.89
s0.1p1.2	79.93 ± 5.15	81.89 ± 4.92	0.53

Table7.7. Results from the continuous compression tests with Instron and in situ loading stage for Ultimate Compressive Strength. (n=5)

	Ultimate Compressive Strength (MPa)		
	Instron	**In Situ Loading Stage**	**p-value**
s0.1p0.8	15.70 ± 0.30	14.81 ± 1.41	0.17
s0.1p1	8.05 ± 0.28	8.04 ± 0.22	0.87
s0.1p1Concept	3.46 ± 0.07	3.44 ± 0.09	0.54
s0.1p1.2	3.97 ± 0.09	3.87 ± 0.22	0.44

Table7.8. Results from the continuous compression tests with Instron and in situ loading stage for Strain at Ultimate Compressive Strength. (n=5)

	Strain at Ultimate Compressive Strength (%)		
	Instron	**In Situ Loading Stage**	**p-value**
s0.1p0.8	9.2 ± 0.5	0.073 ± 0.4	0.001
s0.1p1	7.3 ± 0.2	7.2 ± 0.4	0.53
s0.1p1Concept	4.7 ± 0.3	4.7 ± 0.3	0.78
s0.1p1.2	9.0 ± 0.6	8.2 ± 0.2	0.44

All the p-values were higher than 0.05, except for the strain at ultimate tensile strength for s0.1p0.8. All the comparisons but the latter were considered to be not significantly different with a p-value as high as not to raise doubts. Thus, it was assumed that the difference between testing the samples on the Instron or on the in situ loading stage was not statistically significant. This means that, for further research, samples could be tested only on the in situ loading stage when looking for the mechanical properties of the porous RP Ti6Al4V scaffolds, since the stepwise loading for intermediate micro-CT scanning was carried out on the in situ loading stage.

As mentioned before, the data from the continuous compression tests on s0.1p1 and s0.1p1Concept allowed assessment of the performance of the two SLM machines; LM for s0.1p1 and Concept for s0.1p1Concept.

From the data for s0.1p1 and s0.1p1Concept (Table7.9) it was deduced that there was a difference in the compressive behavior of the samples depending on whether they were LM or Concept manufactured, which was consistent with the graphs in Fig.7.11.

Table7.9. Results from the compression tests carried out on the in situ loading stage for s0.1p1 and s0.1p1Concept. (n=5)

	E (MPa)	**σ_{ucs} (MPa)**	**ε_{ucs} (%)**
s0.1p1	237.74 ± 16.40	8.04 ± 0.22	7.2 ± 0.4
s0.1p1Concept	101.17 ± 9.08	3.44 ± 0.09	4.7 ± 0.3

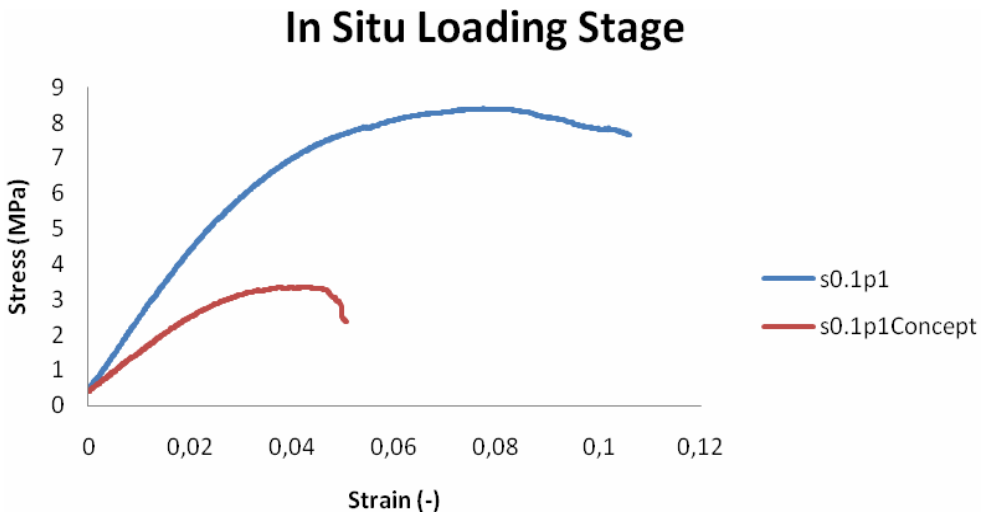

Fig.7.11. Typical stress-strain curves from data obtained from the in situ loading stage for a sample of s0.1p1 and s0.1p1Concept.

E modulus and ultimate compressive strength of porous scaffolds produced with the LM machine were more than twice the ones of Concept produced. The strain at ultimate compressive strength was also significantly higher for samples of s0.1p1. It was concluded that, even though the same production technique (SLM) was used, the LM machine produced scaffolds with much better mechanical performance than the Concept produced ones. The production parameters were set the same for both machines. However, the power of the laser of LM machine was higher, which led to a better melting and a better bonding between particles and, therefore, to higher mechanical properties.

Focusing now on the LM produced scaffolds, data from the continuous compression tests of s0.1p0.8, s0.1p1 and s0.1p1.2 on the in situ stage loading are presented in Table7.10 and Fig7.12 shows typical stress strain curves for s0.1p0.8, s0.1p1 and s0.1p1.2.

Table7.10. Results from the compression tests carried out on the in situ loading stage for s0.1p0.8, s0.1p1 and s0.1p1.2. (n=5)

	E (MPa)	σ_{ucs} (MPa)	ε_{ucs} (%)
s0.1p0.8	369.76 ± 29.83	14.81 ± 1.41	7.3 ± 0.4
s0.1p1	237.74 ± 16.40	8.04 ± 0.22	7.2 ± 0.4
s0.1p1.2	81.89 ± 4.92	3.87 ± 0.22	8.2 ± 0.2

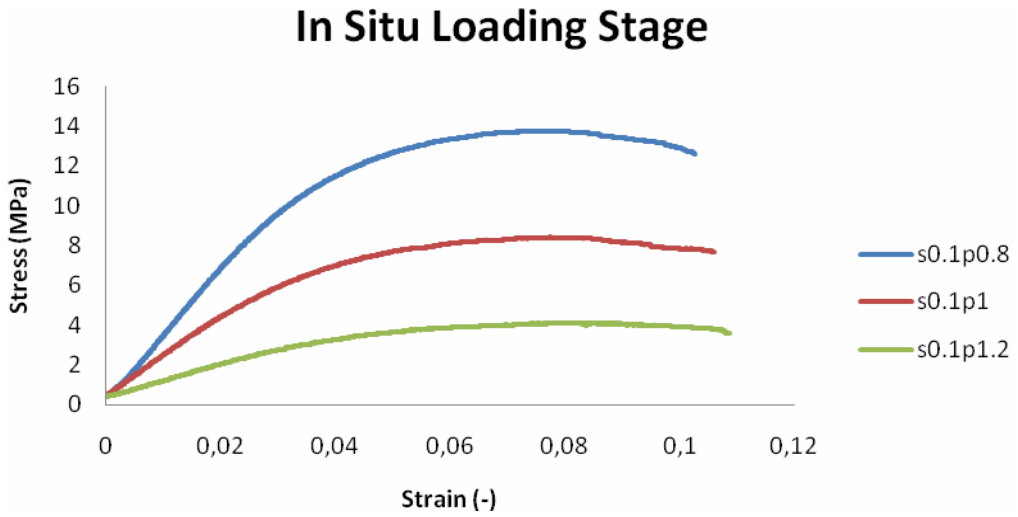

Fig.7.12. Typical stress-strain curves from data obtained from the in situ loading stage for a sample of s0.1p0.8, s0.1p1 and s0.1p1.2.

From Table7.10 it was seen that the variation of mechanical properties within one production batch (for one design) was always below 10%, indicating the robustness of the production technique.

Additionally, the results indicated that the larger the designed pore size, the lower the mechanical properties of the porous scaffolds. Thus, there might be a relation between the designed pore size and the mechanical properties of the porous scaffolds.

In Ref. (Gibson and Ashby [1988]) the correlation between specific density and mechanical properties such as E modulus (eq. 1.3) and ultimate

compressive strength (eq. 1.4) are given for open cell (Fig.7.13*(a)*) and honeycomb structures (Fig.7.13 *(b)*). The unit cell of the scaffolds studied in the present project is shown in Fig.7.13*(c)*.

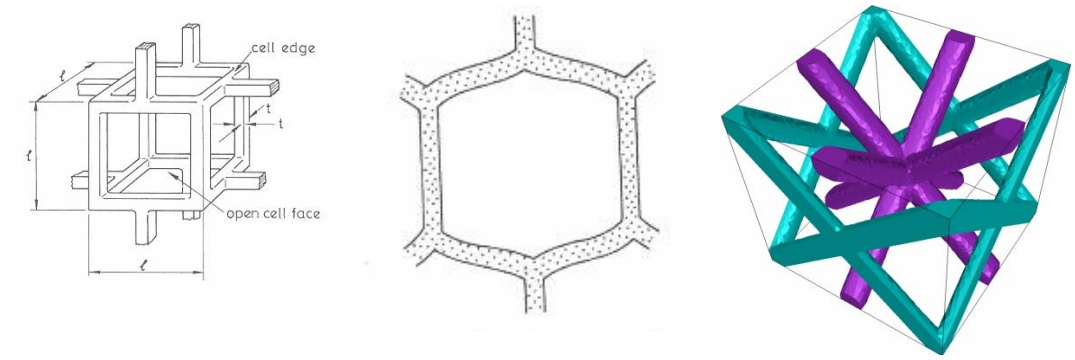

(a) ***(b)*** ***(c)***

Fig.7.13. *(a)* open cell, *(b)* honeycomb cell, *(c)* unit cell of the porous RP Ti6Al4V scaffold.

For open cell structures eq. (7.1) relates the specific density with the E modulus whereas eq. (7.2) relates the specific density with the ultimate compressive strength,

$$\frac{E}{E_s} = \left(\frac{\rho}{\rho_s}\right)^2 \qquad \text{eq. (7.1)}$$

where E is the Young's modulus of the open cell structure, ρ is the density of the open cell structure and E_s and ρ_s are, respectively, the Young's modulus and the density of the bulk material the porous material is made of.

$$\frac{\sigma_{ucs}}{\sigma_{ys}} = C\left(\frac{\rho}{\rho_s}\right)^{2/3} \qquad \text{eq. (7.2)}$$

where σ_{ucs} is the ultimate compressive strength the of open cell structure, σ_{ys} is the yield stress of the bulk material from which the porous material is made of and C is a constant.

For honeycomb structures eq. (7.3) relates the specific density with the E modulus whereas eq. (7.4) relates the specific density with the ultimate compressive strength.

$$\frac{E}{E_s} = 2.3\left(\frac{\rho}{\rho_s}\right)^3 \qquad \text{eq. (7.3)}$$

$$\frac{\sigma_{ucs}}{\sigma_{ys}} = \frac{2}{3}\left(\frac{\rho}{\rho_s}\right)^2 \qquad \text{eq. (7.4)}$$

The E modulus was plotted in function of the volume fraction of the porous RP Ti6Al4V scaffolds (Table7.11), produced by the LM machine, as shown in Fig.7.14 to see whether they were somehow correlated. Volume fraction was calculated from the porosity data obtained via Archimedes, as eq. (7.5) shows.

$$Volumefraction = \frac{100 - Porosity}{100} \qquad \text{eq. (7.5)}$$

Table7.11. E modulus, ultimate compressive strength, porosity and volume fraction for the porous RP Ti6Al4V scaffolds produced by the LM machine. (n=5)

	E (MPa)	σucs (MPa)	Porosity (%)	Volume fraction
s0.1p0.8	369.76 ± 29.83	14.81 ± 1.41	85.28	0.14
s0.1p1	237.74 ± 16.40	8.04 ± 0.22	88.13	0.11
s0.1p1.2	81.89 ± 4.92	3.87 ± 0.22	92.24	0.08

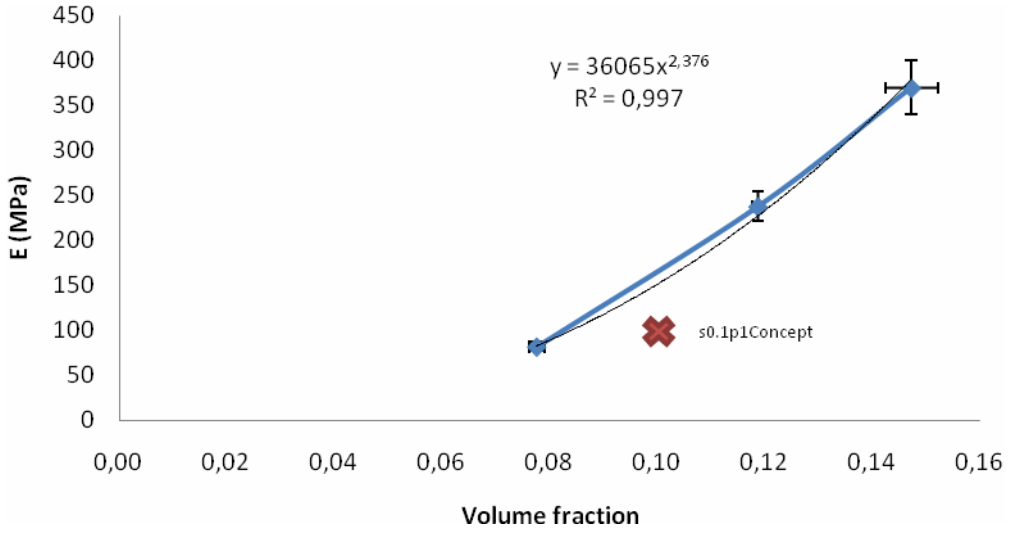

Fig.7.14. E modulus vs. volume fraction for the porous RP Ti6Al4Vscaffolds.

The exponential correlation between Young's modulus and volume fraction found from the experimental data is represented in eq. (7.6).

$$E = 36065\left(volumefraction\right)^{2.38} \qquad \text{eq. (7.6)}$$

Taken into account that volume fraction is equivalent to specific density and that from the compression tests it was known that the $E_s = 42.37$ GPa for the bulk Ti6Al4V structures processed by SLM, eq. (7.7) was obtained.

$$\frac{E}{E_s} = 0.85\left(\frac{\rho}{\rho_s}\right)^{2.38} \text{ (MPa)} \qquad \text{eq. (7.7)}$$

When comparing eq. (7.6) to eq. (7.1) and eq. (7.3) it was seen that the exponent of eq. (7.6) lies between the exponents of eq. (7.1) and (7.3). This meant that, concerning the E modulus, the behavior in compression of the porous Ti6Al4V scaffolds with the structure shown in Fig.7.13*(c)* produced with LM

machine following the SLM technique was found between the behavior of open cell and honeycomb structures.

The ultimate compressive strength was plotted against the volume fraction of the porous Ti6Al4V scaffolds (Table7.11) and visualized in Fig.7.15 to see whether they were somehow correlated.

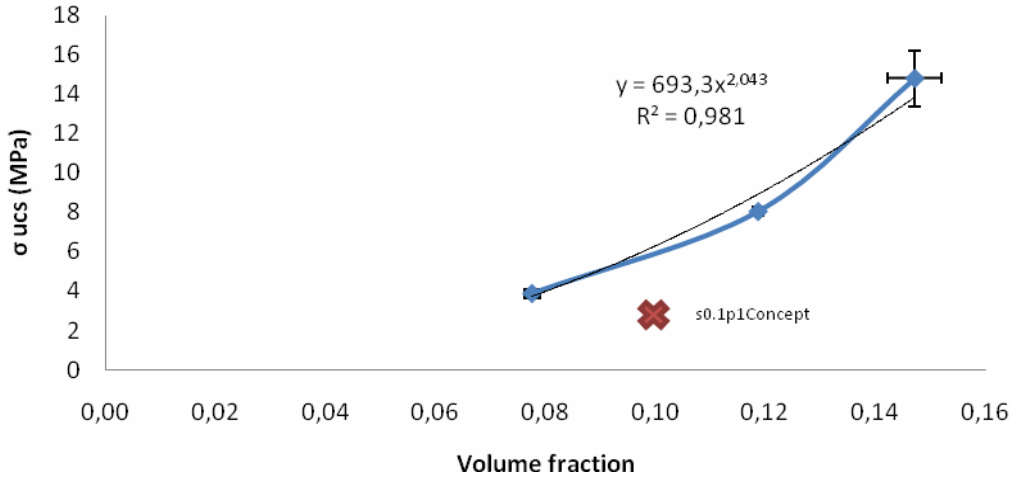

Fig.7.15. Ultimate compressive strength vs. volume fraction for the porous RP Ti6Al4Vscaffolds.

The exponential correlation between the ultimate compressive strength and the volume fraction found from the experimental data is represented in eq. (7.8).

$$\sigma_{ucs} = 693.3(volumefraction)^{2.04} \text{ (MPa)} \qquad \text{eq. (7.8)}$$

Taken into account that volume fraction is equivalent to specific density and that from the compression tests on the Instron it was known that the σ_{ys} = 1.77 GPa for the bulk scaffolds processed by LM, eq. (7.9) was obtained.

$$\frac{\sigma_{ucs}}{\sigma_{ys}} = 0.39\left(\frac{\rho}{\rho_s}\right)^{2.04} \text{ (MPa)} \qquad \text{eq. (7.9)}$$

When comparing eq. (7.9) to eq. (7.2) and eq. (7.4) it was seen that the exponent of eq. (7.9) lies very close to the one of eq. (7.4). This meant that, concerning the ultimate compressive strength, the behavior in compression of the Ti6Al4V porous scaffolds with the structure shown in Fig.7.13*(c)*, produced with LM machine, was close to the honeycomb structures'.

Then, it was verified whether eq. (7.7) and eq. (7.9) were also valid for the porous scaffolds produced by the Concept machine. Taken into account that $E_s = 24620$ MPa and $\sigma_{ys} = 1544.4$ MPa, were the values obtained by compression testing the BulkConcept samples and that for the s0.1p0.1Concept the measured mean volume fraction was 0.1, according to eq. (7.7) and eq. (7.9),

$E = 87.23$ MPa, whereas the actual value was 101.16 MPa.

$\sigma_{ucs} = 5.49$ MPa , whereas the actual value was 3.43 MPa.

Therefore, eq. (7.7) and eq. (7.9) were proved to be valid for LM produced porous RP Ti6Al4V scaffolds, but not for the Concept produced ones. These results indicated that eq. (7.7) and eq. (7.9) were machine dependent, and not production technique dependent.

7.2.2.2. Cyclic loading

The final application of the assessed porous RP Ti6Al4V scaffolds will be to substitute damaged bones, which means that they will be subjected to cyclic loading (fatigue). Therefore, preliminary analysis was done in that field by cyclic testing the scaffolds. Since it was proven that there was no significant difference between testing on the Instron or the in situ loading stage, the cyclic testing was only carried out on the in situ loading stage. They were focused on (i) assessing the performance of the two SLM machines used for the production of designs s0.1p1 and s0.1p1Concept and (ii) on comparing the behavior of the scaffolds with different designed pore sizes under cyclic loading, by analyzing the E modulus in compression and release.

Since the loading cycles were carried out until 0.2 mm displacement, which is far from the strain at the ultimate compressive and tensile strength, the E modulus could not be calculated from the derivative of the fourth grade polynomial. Thus, E modulus was calculated by fitting a linear trend line to the stress-strain curve (Hooke's law). Because a different criterion was used for the calculation of the E modulus, the compressive E modulus from cyclic loading should not be compared to that from the continuous loading, even though both tests were carried out in the in situ loading stage.

As mentioned before, the data from the cyclic loading tests on s0.1p1 and s0.1p1Concept allowed extra assessment of the performance of the two SLM machines; LM for s0.1p1 and Concept for s0.1p1Concept. From the results (Table7.12) it was deduced that there was a difference in the cyclic behavior of the samples depending on whether they were LM or Concept manufactured, which is consistent with Fig.7.16 and Fig.7.17. The E modulus in cyclic behavior of LM produced scaffolds was double the one of Concept produced. These results were consistent with the ones obtained by continuous compression testing.

Table7.12. Results from the cyclic loading tests (10 cycles - 2% strain) carried out on the in situ loading stage for s0.1p1 and s0.1p1Concept. (n=5)

	E compression (MPa)	**E release (MPa)**
s0.1p1	225.87 ± 3.87	221.37 ± 4. 79
s0.1p1Concept	114.17 ± 2.48	115.64 ± 5.39

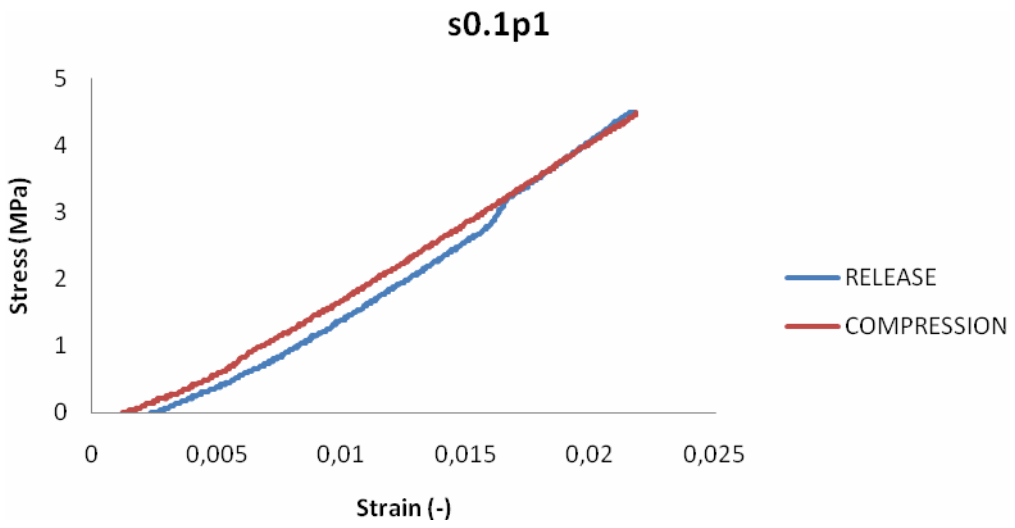

Fig.7.16. Typical compression-relaxation cycle for a sample of s0.1p1.

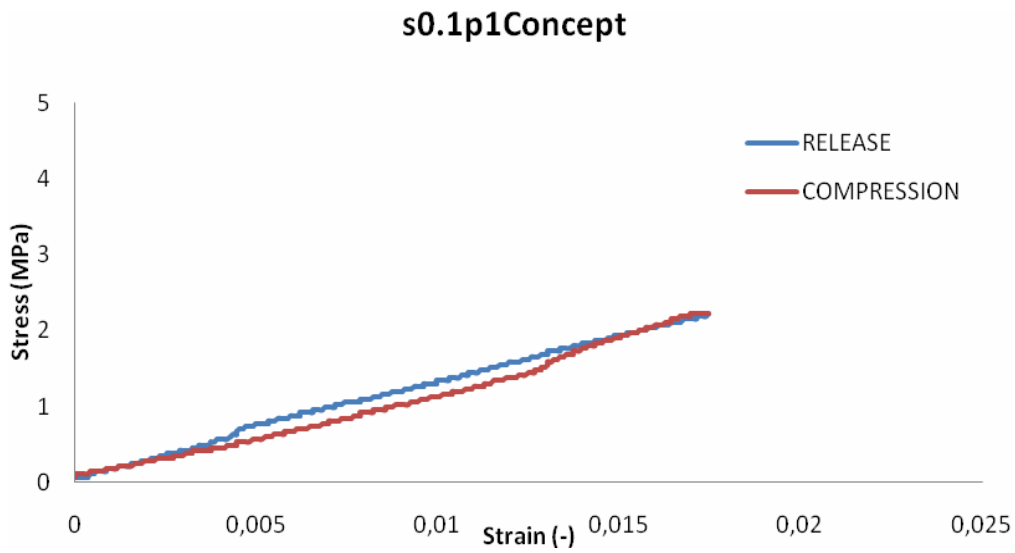

Fig.7.17. Typical compression-relaxation cycle for a sample of s0.1p1Concept.

Focusing now on the LM produced scaffolds, data from the cyclic testing of s0.1p0.8, s0.1p1 and s0.1p1.2 on the in situ loading stage are presented in Table7.13. Fig.7.18, Fig.7.19 and Fig.7.20 show typical compression-release stress-strain curves for S0.1p0.8, S0.1p1 and S0.1p1.2.

Table7.13. Results from the cyclic loading tests (10 cycles - 2% strain) carried out on the in situ loading stage for s0.1p0.8, s0.1p1 and s0.1p1.2. (n=5)

	E compression (MPa)	**E release (MPa)**
s0.1p0.8	431.93 ± 5.21	402.07 ± 1.78
s0.1p1	225.87 ± 3.87	221.37 ± 4. 79
s0.1p1.2	75.409 ± 1.30	90.032 ± 5.27

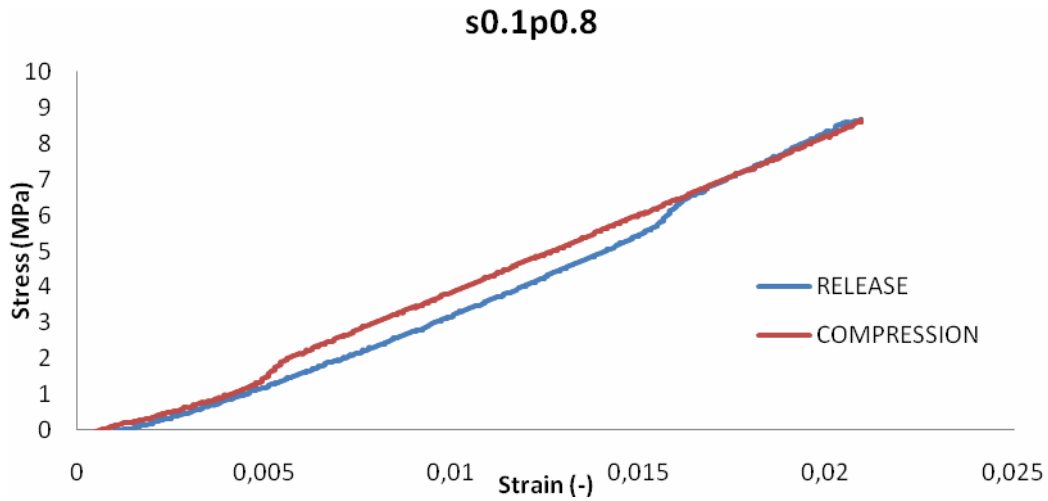

Fig.7.18. Typical compression-release cycle for a sample of s0.1p0.8.

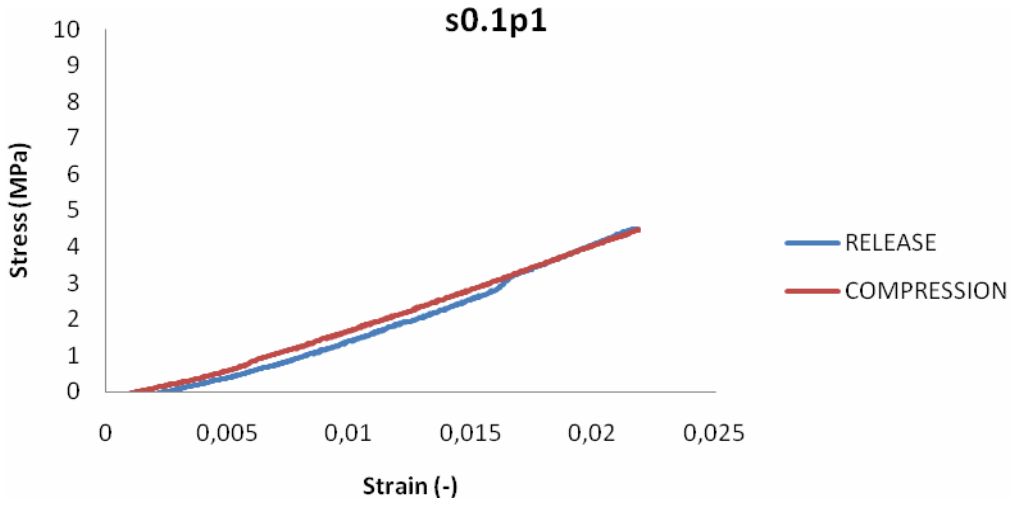

Fig.7.19. Typical compression-release cycle for a sample of s0.1p1.

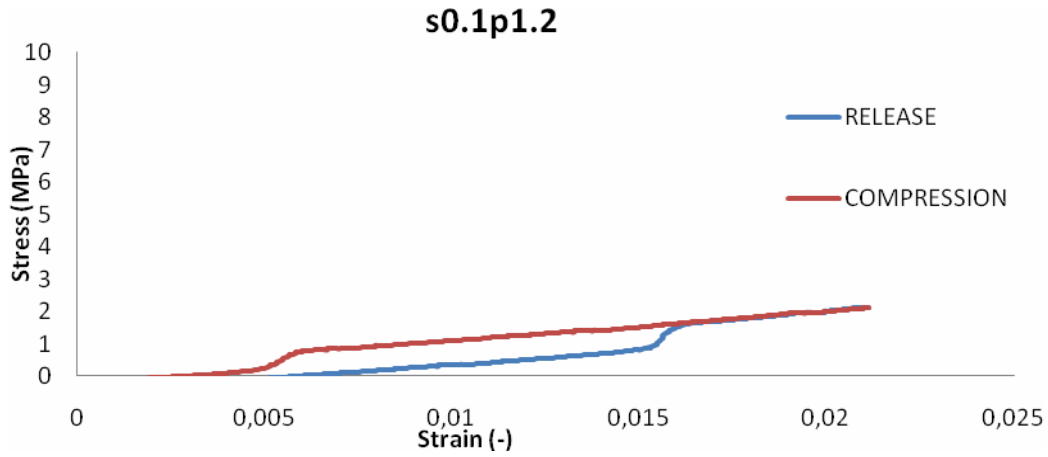

Fig.7.20. Typical compression-release cycle for a sample of s0.1p1.2.

The E modulus in cyclic behavior of LM produced scaffolds decreased with increasing designed pore size. These results were as well consistent with the ones obtained by continuous compression testing.

Even though s0.1p1 and s0.1p1Concept only showed a slight hysteresis, thus, a small difference between E compression and E release, the same could not be said about s0.1p0.8 and s0.1p1.2. Moreover, E compression was significantly higher than E release for design s0.1p0.8, whereas it occurred the other way around for design s0.1p1.2.

In all the graphs that represent compression-release cycles, independently of which design they corresponded to, a small bump was noticed. The bump always happened to appear at the same point of the loading, which indicated that it might be a technical problem of the in situ loading stage. Even though the size of the bump differed from one batch to another, it was always between 10-20 N. A load cell of 30 kN was used for the cyclic tests and the lowest variation that the in situ loading stage can theoretically detect with a load cell of 30 kN is 30 N. However, as it fell out of the order of variations that the in situ loading stage can detect, it was assumed that it had no influence on the behavior of the scaffolds. Thus, E modulus was in all cases calculated fitting a linear trend line to the stress strain curve, as said before, and leaving out the bump.

Nevertheless, the results for the E modulus were not consistent with each other, which together with the presence of the bump, made the data obtained from cyclic loading not reliable. Therefore, for further research, it would be interesting to repeat these cyclic loading tests with a load cell smaller than 30 kN, in order to verify whether the behavior of the scaffolds was affected by the bump.

7.3. Conclusion

The mechanical characterization of bulk structures was carried out in order to assess the performance of the SLM technique and both LM and Concept machines. The results were far from the theoretical ones due to a microporostity

of 0.5% and that the bonding between particles might not be complete via SLM. This might be valuable data for FE modeling, in order to head towards the perfect modeling of the porous RP Ti6Al4V scaffolds.

There was no significant difference between the compression tests carried out on the Instron and the in situ loading stage. Therefore, the stepwise loading which allowed intermediate micro-CT scanning was carried out only on the in situ loading stage. Moreover, the low variability of the studied mechanical properties within samples of the same design indicated that one sample was representative of a design.

Results from the cyclic testing were considered to be unreliable since the they were not consistent and a small bump was noticed in the compression-release cycles of every sample, independently of which design they corresponded to. Thus, further cyclic tests with a smaller load cell should be done to verify whether the bump affected the mechanical behavior of the scaffolds.

Concerning the performance of the two different SLM machines used for the production of scaffolds of designed pore size 1 mm, the compression tests on bulk structures and porous scaffolds showed that samples produced with LM machine had significantly higher mechanical properties than the Concept produced scaffolds. Therefore, Concept produced scaffolds were discarded, thus, no micro-CT combined with in situ loading was carried out on them.

Focusing on the LM produced scaffolds, it was concluded that the E modulus and the ultimate compressive strength of the porous RP Ti6Al4V scaffolds produced by SLM with the LM machine were related to their volume fraction as shown in eq. (7.7). and eq.(7.9) respectively.

$$\frac{E}{E_s} = 0.85\left(volumefraction\right)^{2.38} \text{ (MPa)} \qquad \text{eq. (7.7)}$$

$$\frac{\sigma_{ucs}}{\sigma_{ys}} = 0.39\left(volumefraction\right)^{2.04} \text{ (MPa)} \qquad \text{eq. (7.9)}$$

However, these equations were not valid for Concept produced porous scaffolds. Thus, the equations are machine dependent, and not technique dependent or valid for all SLM produced Ti6Al4V porous scaffolds.

8. Micro-CT combined with in situ loading

Micro-CT combined with in situ loading was carried out on the porous scaffolds produced by the LM machine. As mentioned in previous paragraphs, Concept produced scaffolds were discarded for this type of testing due to their lower mechanical properties compared to the LM produced ones.

The choice of the stopping points of the loading at which the intermediate micro-CT scanning would be carried out was done based on the data from the continuous compression tests. Another important issue in this chapter was to see whether the mechanical behavior of the scaffolds was the same under continuous and stepwise loading; in other words, whether data derived from continuous and stepwise loading resulted in the same mechanical properties.

Another interesting topic was to focus on the morphological characterization of the scaffolds when preloaded to see what the actual morphological difference was between the scaffolds on which the only difference was the designed pore size.

From the biomedical point of view, the change in morphological parameters due to loading was important to be assessed, since cell growth highly depends on the morphological parameters of the scaffold.

8.1. Method

Micro-CT with Skyscan reconstruction software combined with in situ loading was used to characterize the morphology and compressive behavior of the scaffolds. Technical details on the micro-CT device can be read in Table8.1.

Table8.1. Technical details on the micro-CT device.

X-ray source voltage	15-160 kV
Maximum current	3.2 mA
Microfocal spot	From 5 to 200 μm
Minimum spatial resolution	10 μm (5 μm voxel size)
Detector	CCD camera with a resolution of 1024x1024 pixels and a 12 bit dynamic range
Maximum sample dimensions	20 cm width and 20 cm height

The cross sectional imaging of a sample from data obtained from many different directions is called tomography. In the case of micro-CT, the physical excitation in order to obtain the images is X-rays(Van de Casteele [2004]). X-rays are electromagnetic waves consisting of photons, each with an energy E inversely proportional to its wavelength.

$$E = \frac{hc}{\lambda} = h\upsilon \qquad \text{eq. (8.1)}$$

Where $h = 6.6261 \cdot 10^{-20}$Js is Planck's constant, $c = 3 \cdot 10^{8}$ m/s is the speed of light and υ is the frequency (Hz). The wavelength of the X-ray radiation ranges from 0 to 130 kV or expressed in photon energies from 0 to 300 μA.

An X-ray source, depicted in Fig.8.1 consists of a cathode and an anode inside a vacuum tube. When the cathode filament is heated, electrons are ejected from its surface. An electrical potential between the cathode and the anode forces the electrons to accelerate towards the anode. When these electrons impinge on the heavy metal atoms of the target, they interact with these atoms. The interactions result in a conversion of kinetic energy into thermal energy or electromagnetic energy in the form of X-rays.

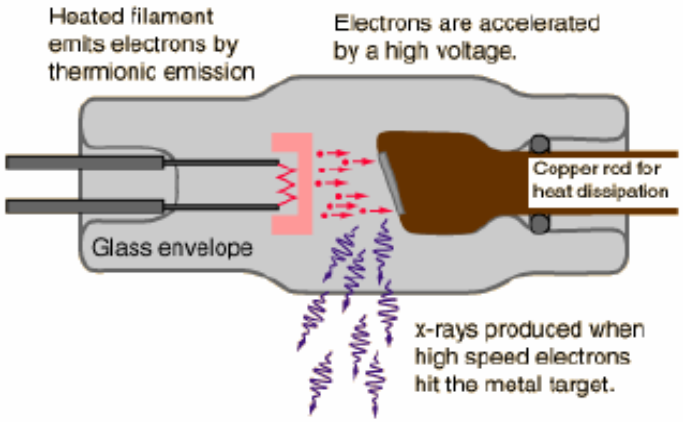

Fig.8.1. Schematic overview of an X-ray source and its components (Van de Casteele [2004]).

When the electrons interact with the outer shell electrons of the target atoms but do not transfer enough energy to ionize them, the kinetic energy of the electrons is converted into heat. This occurs because the outer shell electrons of the target atoms are simply raised to a higher energy level but immediately drop back to their normal energy state with the emission of infrared radiation. Generally, more than 99% of the kinetic energy of the electrons ejected from the cathode is converted to thermal energy. The remaining less than 1% is converted to X-ray radiation in two different ways.

First, if the electron interacts with an inner shell electron of the target, being the interaction strong enough so as to ionize the target atom by total removal of the inner shell electron, the appearing hole will be filled with an outer shell electron. The transition of an orbital electron from an outer shell to an inner shell is accompanied by the emission of an X-ray photon, with energy equal to the difference in the binding energies of the orbital electrons involved. Obviously, this kind of radiation is material dependent and it is known as characteristic X-rays.

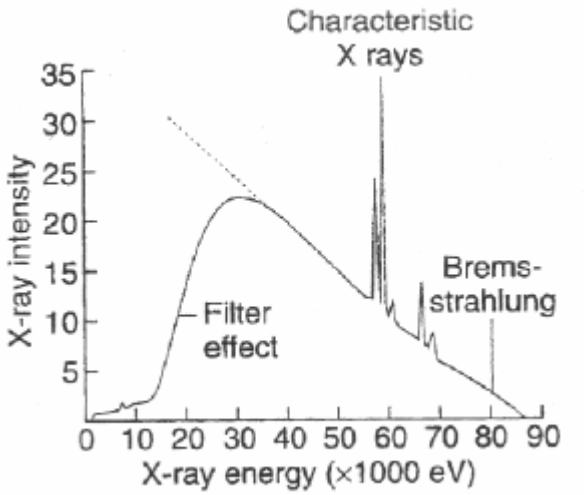

Fig.8.2. X-ray polychromatic spectrum of a tungsten source (Van de Casteele [2004]).

The second process of X-ray production is caused by the interaction of the electron with the nucleus of a target atom. As the colliding electron passes by the nucleus of an anode atom, it is slowed down and deviated in its course, leaving with reduced energy in a different direction. This loss in kinetic energy reappears as an X-ray photon. These types of X-rays are called Bremsstrahlung.

While the characteristic radiation results in a discrete X-ray spectrum of characteristic peaks, the Bremsstrahlung provides a continuous spectrum. The source generates a polychromatic spectrum (Fig.8.2) of X-ray intensities in function of the photon energies, which is dependent on the acquisition parameters. These parameters are the voltage, the current and the use of a filter, in front of the detector or right behind the source.

Once the X-rays have been produced, they are directed so as to interact with the sample that needs to be analyzed.

The photon-matter interactions of primary importance in the energy ranges used in X-ray imaging in microtomography are photoelectric effect and Compton scattering. The photoelectric effect causes an incident X-ray to interact with an electron within an inner shell. Due to the interaction the electron will be ejected from the atom. If the photon carries more energy than is necessary to eject the electron, it will transfer this residual energy to the ejected electron in the form of kinetic energy. The X-ray is thus completely absorbed. The Compton scattering, also known as incoherent scattering, occurs when the incident X-ray photon interacts with an outer electron. This will lead to the X-ray to be scattered in a different direction at a lower energy.

For monoenergetic X-rays, the attenuation in matter is given by Lambert-Beer's law of absorption, which states that each layer of equal thickness absorbs an equal fraction of the radiation that traverses it. Mathematically, this is expressed as follows:

$$\frac{dI}{I} = -\mu dx \qquad \text{eq. (8.2)}$$

with I the intensity of the incident radiation, $\frac{dI}{I}$ the fraction of radiation removed from the beam as it traverses a small thickness, dx, of material and μ the linear attenuation coefficient that will be caused by the photoelectric effect and the Compton scattering.

After passing through the object, the X-rays are detected by the detection system. The ideal detector for X-ray imaging should detect every incident photon of the complete band of X-ray energies and its response should be linear over a large range of intensities. The detection system has a scintillator that converts energetic radiation (electrons and X-rays) into photons to be transferred to a light sensitive sensor, thus, a CCD camera by optical fibers.

The outcome of the detector is an X-ray shadow image that corresponds to a two dimensional (2D) projection from a 3D object. Using a reconstruction algorithm, those images can be converted to 2D images of the section of the sample to be then stuck together to form a 3D image.

Thus, micro-CT allows visualizing the 3D, internal structure of objects in a non-destructive way.

In the present project, a batch of five samples per design was analyzed via micro-CT combined with in situ loading, while only one sample was analyzed for S0.1p1Concept.

The following steps were followed for the analysis of each sample:

1. Measuring the dimensions of the sample with an electronic caliper.
2. Preloading the sample in the in situ loading stage at load 0.01 kN.
3. Rotation of the sample to allow it to settle before scanning in order to avoid movement during scanning, which would have impoverished the scanning data.
4. 3D scanning of the sample at 90 kV, the maximum allowed intensity (mA), with an aluminum filter of 1 mm right behind the source(Kerckhofs et al. [2006]), with a frame averaging of 16 and an angular increment of 0.5°. The time required to make a complete 3D image and increment the strain was just under 20 min.
5. Each sample was scanned six or seven times; the first one when preloaded, and the following for displacement increments of 0.2 mm, as shown in Fig8.3.

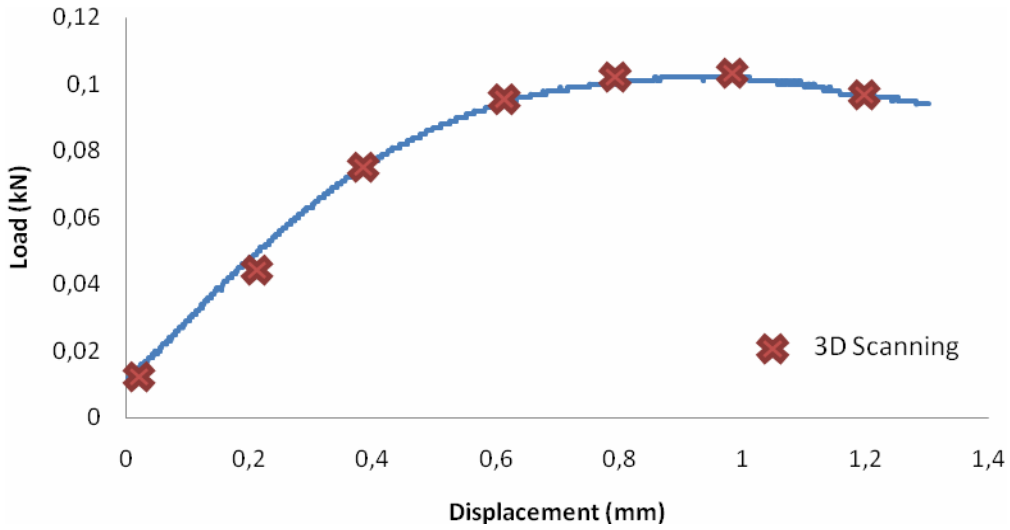

Fig8.3. 3D scanning of the scaffolds was done at preload and displacement increments of 0.2 mm.

6. Conversion of the radiographic files to 8-bit grayscale tiff-files in order to be able to reconstruct them using SkyScan's volumetric reconstruction software Nrecon, which creates a set of cross-section slices through the object from the set of acquired angular projections. Finally, CTAn was used to run a 3D analysis on the dataset obtained with Nrecon.

8.2. Stepwise loading

Stepwise loading was carried out on the porous scaffolds to allow intermediate micro-CT scanning at different displacements. A typical stress strain curve for stepwise loading is shown in Fig.8.4.

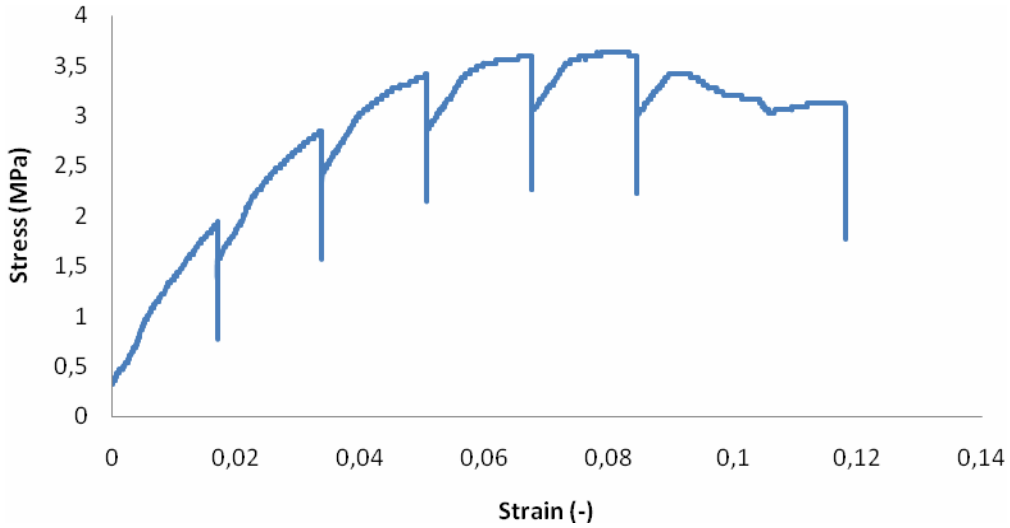

Fig.8.4. Typical stress strain curve for stepwise loading.

In order to be able to compare the E modulus of the stepwise loading with the one from continuous loading the same procedure was followed to calculate it.

Therefore, the points of the curve corresponding to scanning and relaxation time were deleted using a "logical function" in Excel (eq. 8.1).

IF (stress X+1 < stress X, stress X, stress X+1) eq. (8.1)

Eq. (8.1) stands for the following: if the value of the stress in one point is smaller than in the previous point, the stress value of the previous point is taken; if not, the actual value of stress is taken. This meant that once the ultimate compressive strength was reached, the stress value would never go down again (Fig.8.5). However, it would not affect the calculation of the mechanical properties.

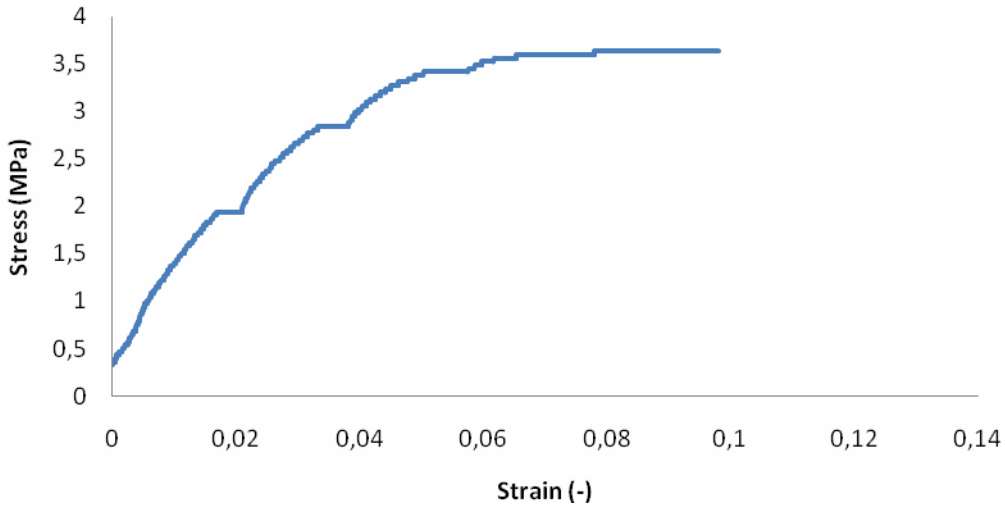

Fig.8.5. Stress-strain curve for stepwise loading from which the points corresponding to scanning and relaxation time were deleted.

The points corresponding to the relaxation or scanning time were deleted for all the samples. Fig.8.6 shows typical stress strain curves for s0.1p0.8, s0.1p1 and s0.1p1.2.

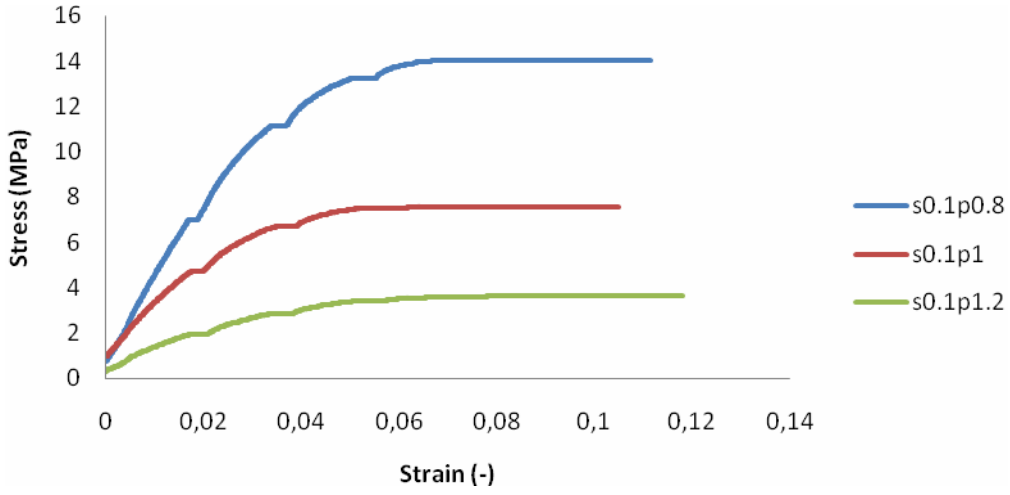

Fig.8.6. Stress-strain curves for stepwise loading from which the points corresponding to scanning and relaxation time were deleted for s0.1p0.8, s0.1p1 and s0.1p1.2.

The results for the mechanical properties from the stepwise loading are summarized in Table8.2, Table8.3 and Table8.4 together with the ones from the continuous loading and the p-values corresponding to the comparison between both.

Table8.2. Results from the continuous and stepwise compression tests with the in situ loading stage for Young's modulus. (n=5)

	Young's modulus (MPa)		
	Continuous	**Stepwise**	**p-value**
s0.1p0.8	369.76 ± 29.83	481.77 ± 28.12	0.014
s0.1p1	237.74 ± 16.40	267.06 ± 28.81	0.094
s0.1p1.2	81.89 ± 4.92	108.17 ± 8.22	0.007

Table8.3. Results from the continuous and stepwise compression tests with the in situ loading stage for the ultimate compressive strength. (n=5)

	Ultimate compressive strength (MPa)		
	Continuous	**Stepwise**	**p-value**
s0.1p0.8	14.81 ± 1.41	14.49 ± 0.95	0.36
s0.1p1	8.04 ± 0.22	7.78 ± 0.18	0.071
s0.1p1.2	3.87 ± 0.22	3.69 ± 0.13	0.257

Table8.4. Results from the continuous and stepwise compression tests with the in situ loading stage for strain at ultimate compressive strength. (n=5)

	Strain at ultimate compressive strength (%)		
	Continuous	**Stepwise**	**p-value**
s0.1p0.8	7.27 ± 0.35	7.19 ± 0.65	0.36
s0.1p1	7.16 ± 0.39	6.54 ± 0.08	0.018
s0.1p1.2	8.24 ± 0.17	7.71 ± 0.57	0.06

Results for the continuous and the stepwise loading were consistent when referring to the ultimate compressive strength and the strain at ultimate compressive strength, except for s0.1p1, for which the p-value is lower than 0.05. However, they are significantly different concerning the E modulus. Being the ultimate compressive strength and the strain at ultimate compressive strength the same for continuous and stepwise loading, from Hooke's law (eq. 8.2), E modulus should also be consistent.

$$\sigma_{ucs} = E \cdot \varepsilon_{ucs} \qquad \text{eq. (8.2)}$$

This indicates that the way E modulus was calculated is correct since the assessed material is non linear elastic, but this procedure induces errors when stepwise loading is being carried out.

8.3. Analysis of the micro-CT imaging at preload

A study was done on the morphological parameters of the porous scaffolds when preloaded to see what the actual morphological difference was between scaffolds on which the only difference was the designed pore size. Fig.8.7 shows one radiograph per design of the preloaded samples.

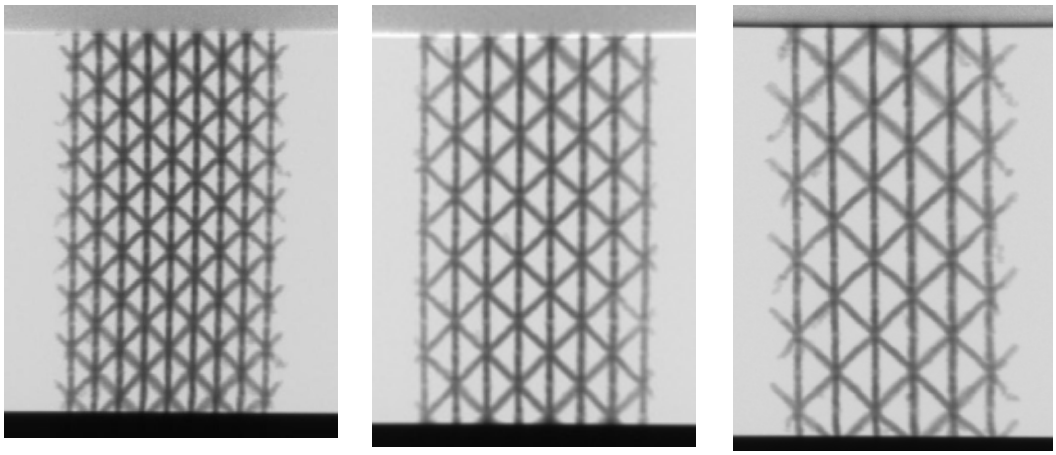

(a) s0.1p0.8 *(b)* s0.1p1 *(c)* s0.1p1.2

Fig.8.7. Preloaded radiograph of a sample of *(a)* s0.1p0.8. *(b)* s0.1p1 and *(c)* s0.1p1.2.

A description of the morphological parameters obtained by micro-CT is shown in Table8.5.

Table8.5. Morphological parameters from micro-CT.

Porosity (%)	The volume that belongs to pores divided by the total volume of the scaffold.
Specific surface (1/mm)	Surface area divided by the volume of the scaffold.
Anisotropy	Measures the presence or absence of preferential alignment of structures along a particular directional axis. It is represented by a number between 0 and 1, where 0 means the analyzed structure is isotropic.
Avg. Strut diameter (μm)	Determined as an average of the local thickness at each voxel representing solid(Hildebrand and Ruegsegger [1997]).
Avg. Pore diameter (μm)	Determined as an average of the local thickness at each voxel representing solid, binarizing the image opposite as to calculate the strut diameter.
Interconnectivity (%)	Percentage of pores of the scaffold reachable from the outside. It is calculated as Interconnectivity (%) = 100 - Closed porosity (%)

The results for the porosity from micro-CT are shown in Table8.6. The porosity obtained from micro-CT analysis was slightly lower than the one obtained by Archimedes. This was an expected result, since errors due to the partial volume effect(De Man et al. [1999; De Man et al. [2000]) or the limited resolution are inherently present in micro-CT images. However, both results fit reflecting that the bigger the designed pore size, the higher the porosity of the scaffolds. The fact that the micro-CT porosity is consistent with Archimedes, the physical reference, proved that the measurements done by micro-CT were correct.

Table8.6. Porosity data from Archimedes and micro-CT for s0.1p0.8, s0.1p1 and s0.1p1.2. (n=5)

	Porosity (%)	
	Archimedes	**Micro-CT**
s0.1p0.8	85.28 ± 0.49	80.52 ± 1.08
s0.1p1	88.13 ± 0.10	85.43 ± 0.33
s0.1p1.2	92.24 ± 0.15	90.71 ± 1.14

Morphological parameters measured via micro-CT in the preloaded stage are presented in Table8.7. The low variation on the morphological parameters within the same design proofs the high repeatability and robustness of the LM machine and hence the production technique (SLM).

Table8.7. Morphological parameters obtained via micro-CT for the preloaded stage. (n=5)

	s0.1p0.8	**s0.1p1**	**s0.1p1.2**
Porosity (%)	80.52 ± 1.08	85.43 ± 0.33	90.71 ± 1.14
Specific surface (1/mm)	21.94 ± 0.65	21.59 ± 0.63	22.75 ± 0.67
Anisotropy	0.59 ± 0.02	0.61 ± 0.02	0.68 ± 0.10
Avg. Pore diameter (μm)	480 ± 8	601 ± 4	776 ± 12
Avg. Strut diameter (μm)	187 ± 5	601 ± 4	181 ± 5
Interconnectivity (%)	100	100	100

Specific surface, anisotropy and interconnectivity are important morphological parameters from the biomedical point of view, since cell seeding and growth is strongly affected by them. It can be seen that those parameters hardly varied from one designed pore size to the other in the preloaded state. Nevertheless, they are very important values since their evolution may differ when the scaffold is loaded depending on the designed pore size.

From the engineering point of view the most important parameters to analyze are interconnectivity, pore diameter distribution and strut diameter distribution.

The fact that interconnectivity was 100%, as designed, gives again an idea of how robust the SLM processing is with the LM machine in the case of the porous Ti6Al4V scaffolds being assessed.

Fig.8.8, Fig.8.9 and Fig.8.10 show the pore diameter distribution for scaffolds of s0.1p0.8, s0.1p1 and s0.1p1.2. The pore diameter distribution was not constant for the different samples within design s0.1p1.2. Since the samples were 6 mm in diameter, only about 5 unit cells would be present in the width. And, because, for micro-CT analysis, a volume of interest was chosen not taking into account the edges, too few unit cells were present in the micro-CT datasets to attain quantitative data. Therefore, it was concluded that for further research, wider samples should be assessed for s0.1p1.2.

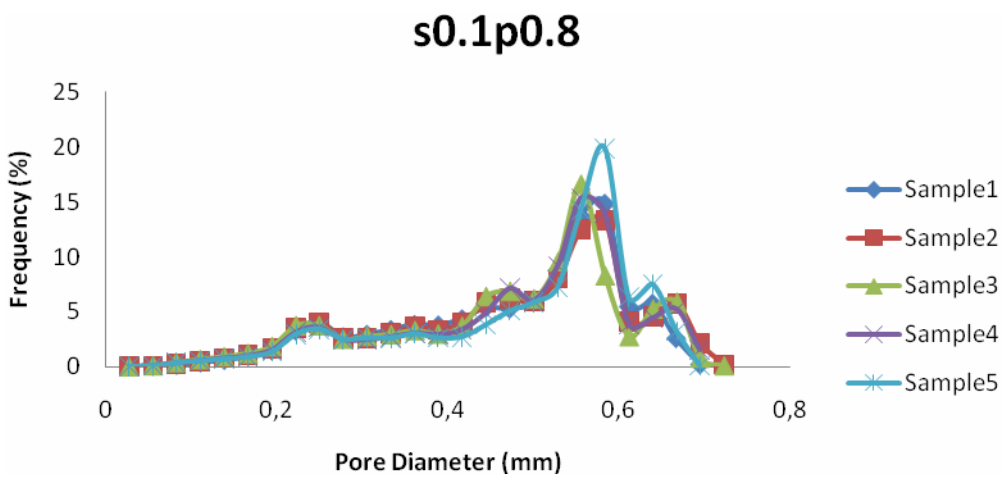

Fig.8.8. Pore diameter distribution of samples of s0.1p0.8.

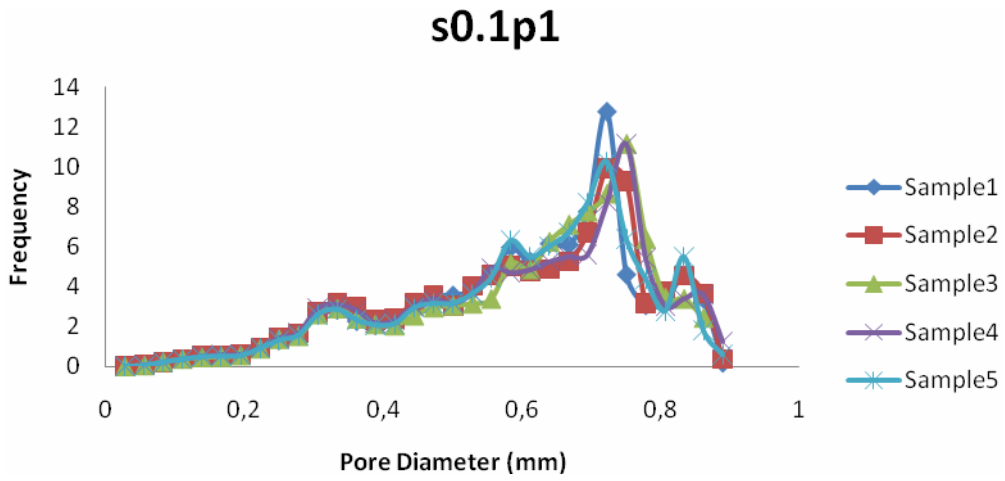

Fig.8.9. Pore diameter distribution of samples of s0.1p1.

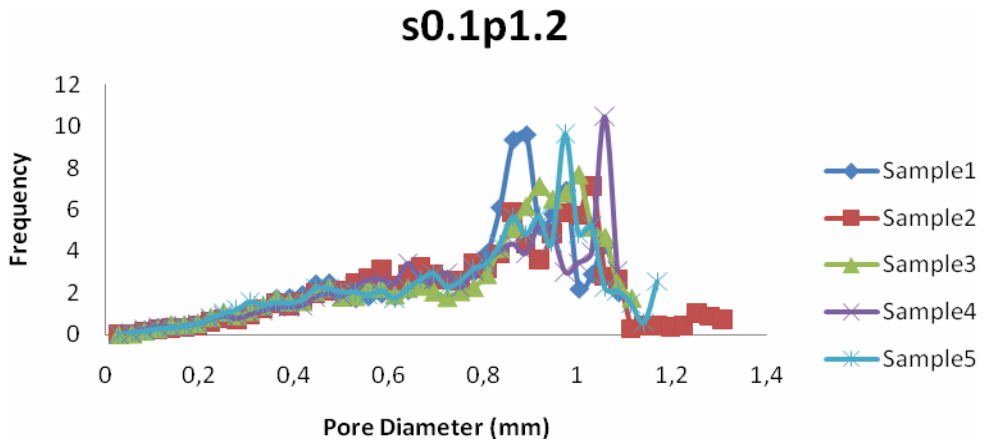

Fig.8.10. Pore diameter distribution of samples of s0.1p1.2.

Fig.8.11 *(a)* shows a unit cell of the bone scaffold whereas Fig.8.11 *(b)* shows a simplification of the unit cell in which the designed pore size is defined by the black arrow.

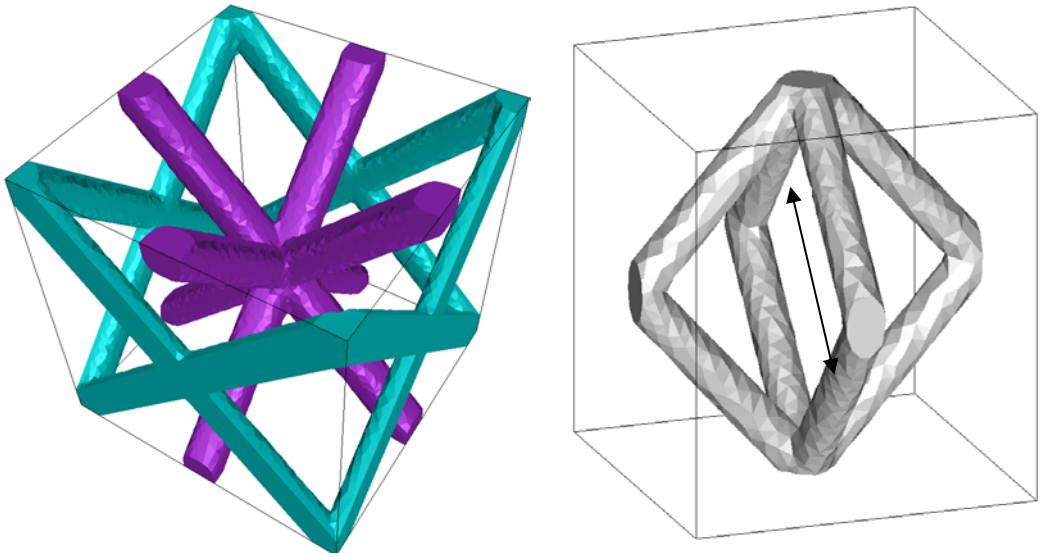

(a) *(b)*

Fig.8.11. *(a)* unit cell of the bone scaffold *(b)* simplified unit cell of the bone scaffold in which the designed pore diameter is defined by an arrow.

At present, it was not yet possible to establish the correspondence between the peaks on the graphs of the data obtained via micro-CT and the physical pores to which they correspond. This is ongoing work.

The only difference in the design of s0.1p0.8, s0.1p1 and s0.1p1.2 was the designed pore size, being the production method and machine the same. The strut diameter was designed to be 0.1 mm. Thus, it should be the same for every batch, independently of the designed pore size. Fig.8.12, Fig.8.13 and Fig.8.14 show the strut diameter and the frequency with which each appears for the different designs.

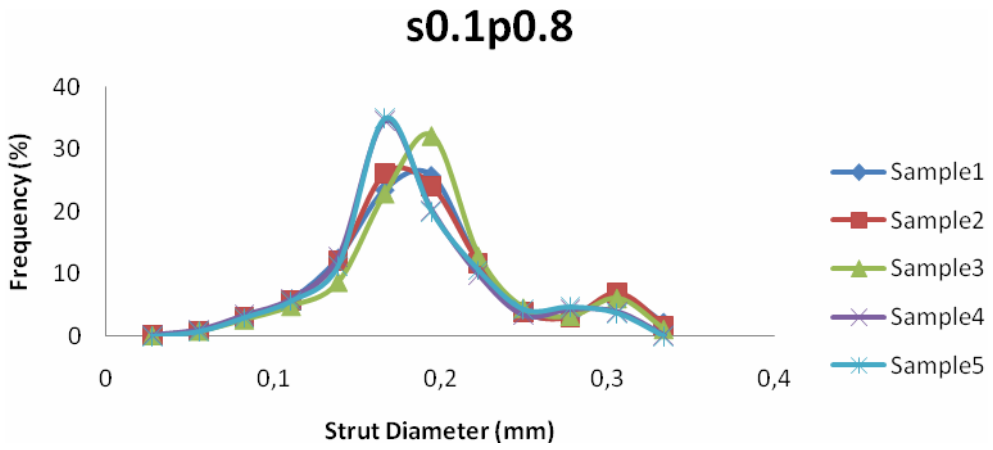

Fig.8.12. Strut diameter distribution of samples of s0.1p0.8.

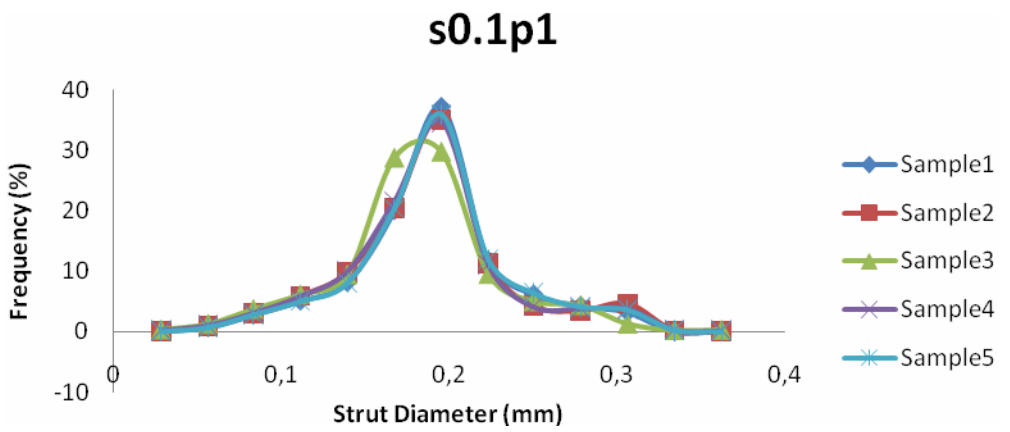

Fig.8.13. Strut diameter distribution of samples of s0.1p1.

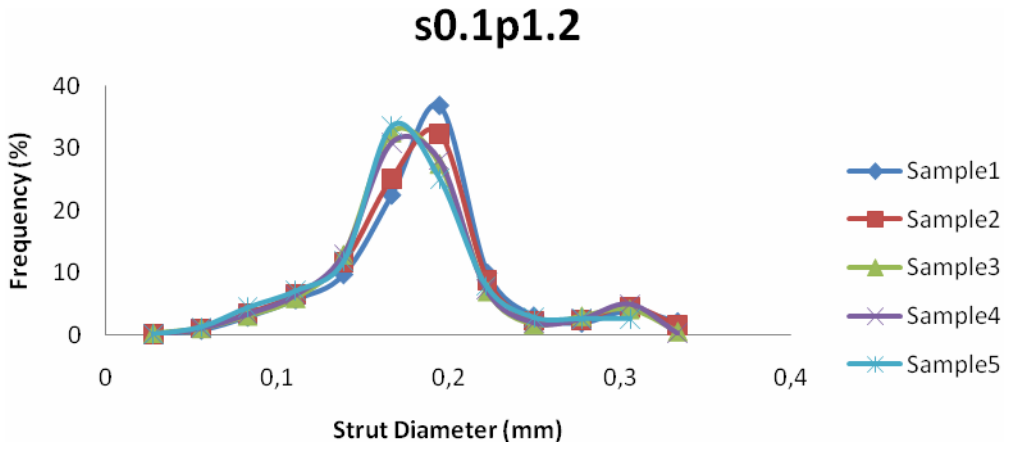

Fig.8.14. Strut diameter distribution of samples of s0.1p1.2.

Every graph in Fig.8.12, Fig.8.13 and Fig.8.14 shows two peaks. The highest one corresponded to the actual strut diameter (Fig.8.15 *(a)*), whereas the smallest one on its right represented the diameter of the nodes (Fig.8.15 *(b)*), thus, the points at which four struts met.

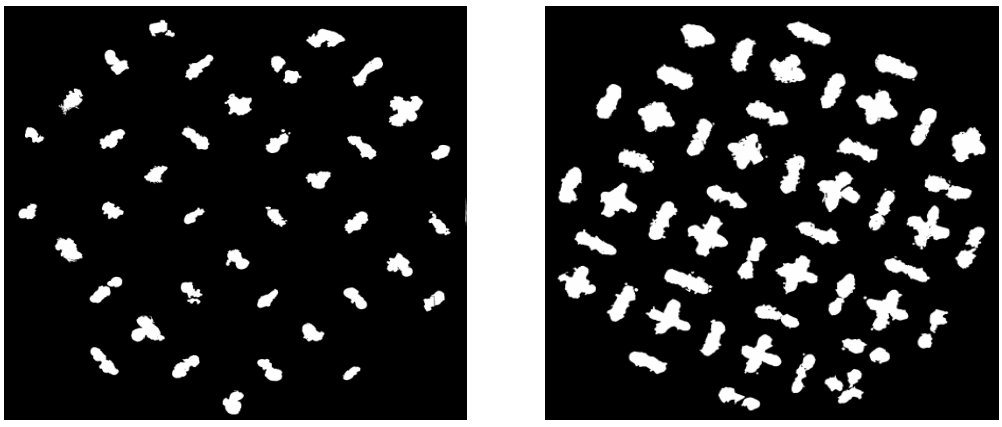

(a) *(b)*

Fig.8.15.*(a)* cross-section of scaffold in which struts can be seen *(b)* cross-section of scaffold in which nodes can be seen, each surrounded by four struts.

Table8.8 summarizes the actual and the designed strut diameter. Fig.8.16 shows the average strut diameter distribution for the different designs at preload indicating that the diameter of the struts was constant no matter what the designed pore size was, which confirmed the repeatability and robustness of the production technique (SLM). However, the actual strut diameter was almost twice the designed one. This was attributed to the fact that the designed value was very close to the physical production limits.

Table8.8. Strut diameter for s0.1p0.8, s0.1p1 and s0.1p1.2 at preload. (n=5)

	Strut diameter (mm)
s0.1p0.8	0.179 ± 0.006
s0.1p1	0.188 ± 0.004
s0.1p1.2	0.180 ± 0.005
Design	0.100

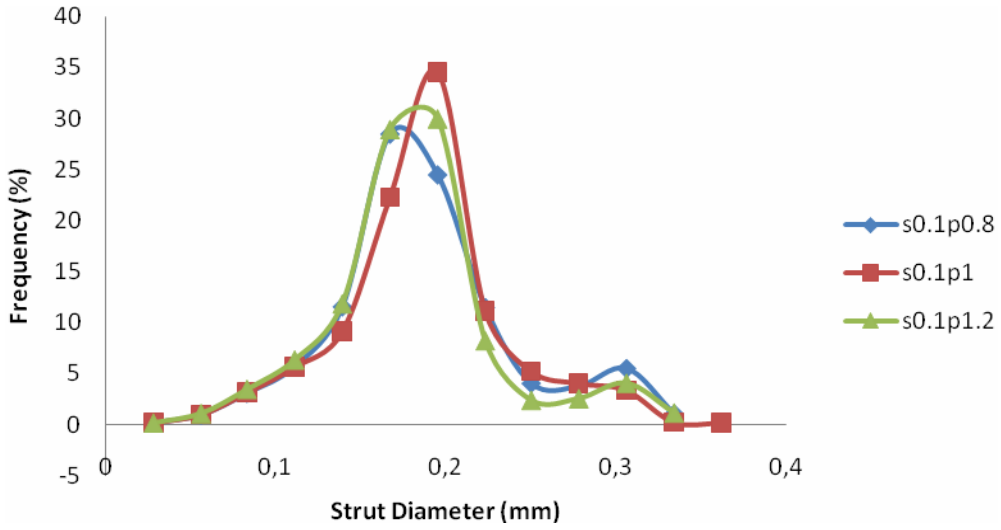

Fig.8.16. Mean strut diameter distribution for s0.1p0.8, s0.1p1 and s0.1p1.2.

8.4. Stepwise loading combined with micro-CT imaging

Stepwise loading combined with micro-CT imaging allowed studying the evolution of the morphological parameters of the scaffold under varying compressive load, thus, for different strain values. Because of the low variability on the morphological parameters within the scaffolds of the same design and the lack of time, only data for one sample per design was analyzed.

Fig.8.17 shows, for one sample per design, how porosity changed through the different loading steps. It was seen that porosity increased, in all cases, until strain 5%, which corresponded to a stress just prior to the ultimate compressive strength. Porosity increased due to the bulking out of the structure when compressed (Fig.8.18), which might indicate buckling of the struts. However, from strain 5% on the porosity either remained constant or slightly decreased as a consequence of the struts coming together due to the compressive load, making the pores smaller.

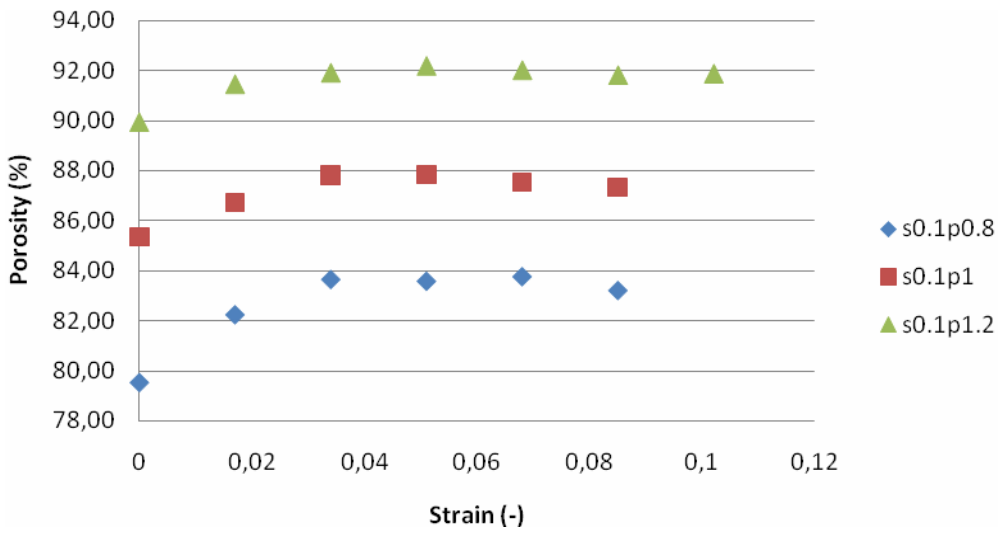

Fig.8.17. Porosity vs. strain for one sample per design.

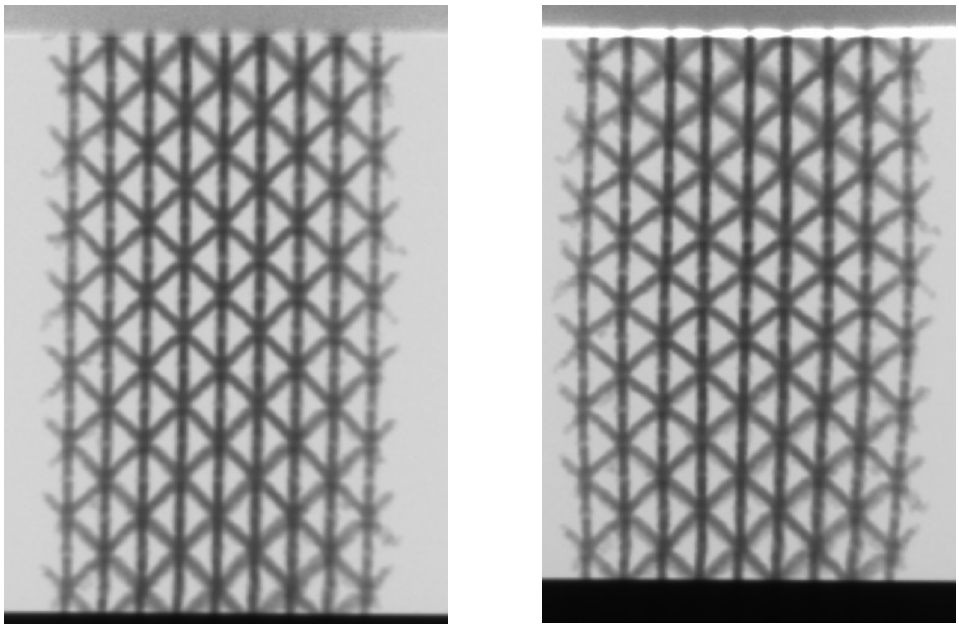

(a) *(b)*

Fig.8.18. *(a)* scaffold at preload (strain 0%) *(b)* scaffold at strain 5%.

Concerning the variation of the strut diameter, only the data of one sample was analyzed, since in the case of the strut diameter the variability was low not only within the same design, but also between different designs. Fig.8.19 shows the variation of the strut diameter through the different loading steps. It was seen that it remained the same, in other words, the strut diameter did not change when the scaffold was stepwise loaded in compression.

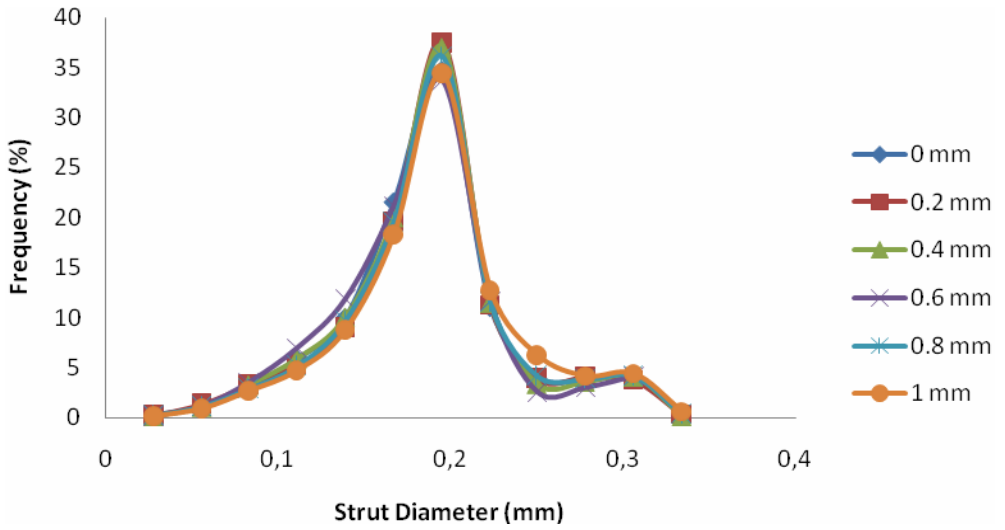

Fig.8.19. Distribution of strut diameter at different displacement values for one sample.

Fig.8.20 shows, for one sample per design, how anisotropy varied through the different loading steps. The evolution of anisotropy followed the same path for designs s0.1p0.8 and s0.1p1.2, i.e. it increased when increasing the strain. Nevertheless, it kept increasing until strain 5% and then decreased to a lower value than the initial one for design s0.1p1.

This indicated that the anisotropy of the scaffolds varied with the strain value, and that it might be reflected in the radiographic images, which, was not yet verified, due to the lack of time. It is ongoing work. However, this data were indicative of how data obtained via micro-CT for different loading steps might lead to the comprehension of the relations between failure and morphological parameters of the porous RP Ti6Al4V scaffolds.

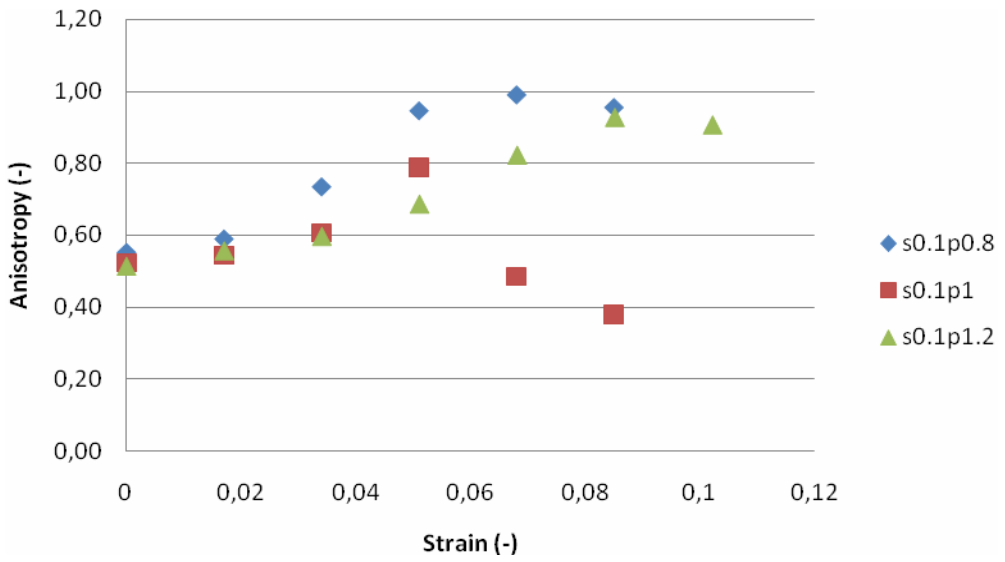

Fig.8.20. Anisotropy vs. strain for one sample per design.

8.4.1. Failure mechanisms

The radiographs of the loaded samples can serve as a tool to define and/or check the failure mechanisms occurring during loading. From the radiographs it seemed there were some differences in the failure mechanisms between the different designs (Fig.8.21). The larger the designed pore size, the less evident the shear banding was.

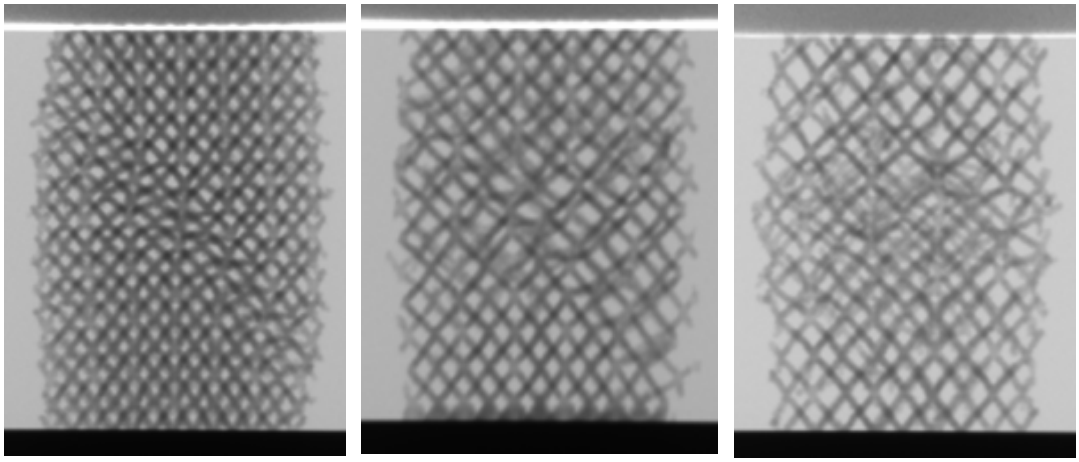

(a) *(b)* *(c)*

Fig.8.21. ***(a)*** **s0.1p0.8** ***(b)*** **s0.1p1** ***(c)*** **s0.1p1.2**

Moreover, the upper and bottom part of the scaffold did not register any changes, being the middle part the one that deformed (Fig.8.22). The buckling of the struts, highlighted with red circles, can be appreciated in the pictures.

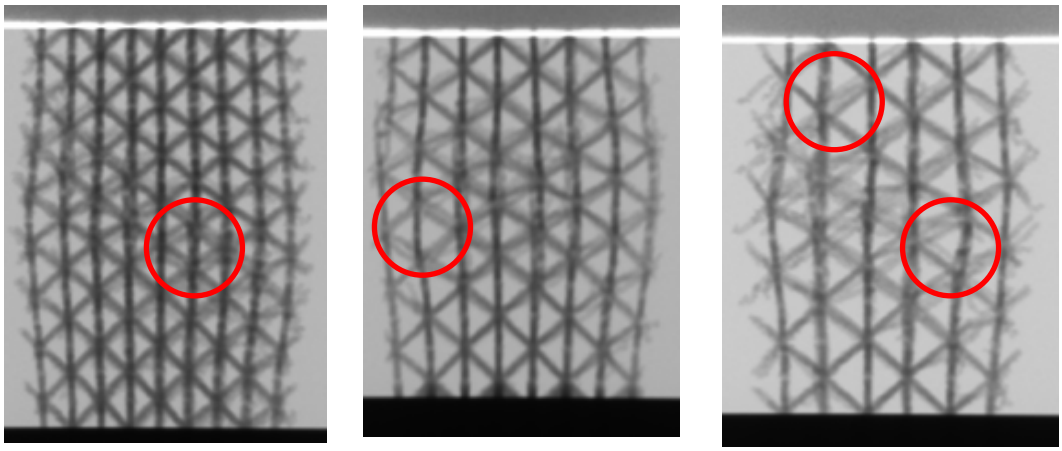

(a) *(b)* *(c)*

Fig.8.22. ***(a)*** **s0.1p0.8** ***(b)*** **s0.1p1** ***(c)*** **s0.1p1.2**

A deeper analysis of the data obtained via micro-CT was not yet possible due to the lack of time. Nevertheless, it was concluded that the location of the onset of failure and a thorough understanding and/or characterization of the failure mechanisms of the porous RP Ti6Al4V bone scaffolds might be possible by studying the radiographic images corresponding to the different loading steps.

8.5. Conclusion

Stepwise compression loading was concluded to be significantly different to the continuous for porous RP Ti6Al4V bone scaffolds. The ultimate compressive strength and the strain at ultimate tensile strength were the same for both loading ways. Thus, applying Hooke's law, E modulus would have also been consistent. However, the assessed material was non linear elastic so Hooke's law was not applied and the values obtained for the E modulus were different for stepwise and continuous loading. Therefore, the porous RP Ti6Al4V scaffolds were considered to behave differently in stepwise and continuous loading.

Morphological characterization of the assessed scaffolds was carried out at the preloaded stage. Micro-CT was proven to be an accurate method for the morphological characterization of the porous RP Ti6Al4V bone scaffolds, using volume fraction measured via Archimedes as a physical reference. The actual strut diameter was almost twice the designed one, which was attributed to the fact that the designed value was close to the physical production limits. Nevertheless, the variability of the data on strut diameter was small, which indicated a good repeatability of the LM machine. Concerning the porosity, it was at present not yet possible to establish the correspondence between the peaks on the graphs of the data obtained via micro-CT and the physical pores to which they corresponded due to the complexity of the unit cell. Furthermore, the variability was significant for design s0.1p1.2 since only a few unit cells were present in the 6 mm of width of the samples. Thus, for further research, wider samples would be advisable.

Stepwise loading combined with micro-CT imaging allowed studying the evolution of the morphological parameters, such as porosity, strut diameter and anisotropy, of the scaffolds under varying compressive load, thus, for different strain values, as well as deriving the failure mechanisms.

The strut diameter was found to be independent of the applied compressive strength. However, porosity and anisotropy varied under compressive loading. Porosity first increased due to the bulking out of the structure when compressed, which might indicate buckling of the struts. And from strain 5% on it either remained constant or slightly decreased as a consequence of the struts coming together due to the compressive load, making the pores smaller. This information was derived from the graphs, though not yet proven by analyzing the corresponding images, which is ongoing work.

In spite of being ongoing work, from a first analysis of the radiographs of the loaded samples it seemed that the larger the designed pore size, the less evident the shear banding was. Moreover, the mid part of the scaffolds seemed to be the one deforming, whereas the upper and bottom part did not register any changes. The location of the onset of failure and a thorough understanding and/or characterization of the failure mechanisms of the porous RP Ti6Al4V bone scaffolds might be possible by studying the radiographic images corresponding to the different loading steps.

To sum up, it was concluded that micro-CT itself or stepwise loading combined with micro-CT imaging offer the possibility to thoroughly characterize porous RP Ti6Al4V scaffolds morphologically and mechanically under varying

compressive loading, locate the onset of failure and derive the failure mechanisms.

9. General conclusion

RP techniques are very suitable for the production of bone scaffolds since they allow a high control over the morphological parameters, which are of main importance for the seeding and growth of cells. In the present project, porous Ti6Al4V bone scaffolds produced via SLM, a RP technique, with two different machines, LM and Concept, were analyzed.

The performance of the SLM RP technique was assessed by mechanically characterizing bulk Ti6Al4V structures. The mechanical properties, in compression, for the bulk Ti6Al4V structures produced via SLM were found to be significantly lower than the theoretical ones, which induced to conclude that apart from the microporosity of 0.5%, there might not exist a perfect bonding between particles via SLM. This might be an interesting input for the FE modeling, since it allows further knowledge on the properties of the Ti6Al4V structures processed via SLM.

Mechanical and morphological characterization of the porous RP Ti6Al4V bone scaffolds produced with LM machine was carried out, via several methods, amongst which stepwise loading combined with micro-CT should be mentioned, with the final goal of finding a correlation between them. In the present project, a novel in situ loading stage was placed inside the micro-CT to avoid the transfer of the samples. Validation of the novel in situ loading stage was performed demonstrating that there was no significant difference between loading the samples on an Instron 4505, which is a conventional loading device, and the in situ loading stage. Thus, for future work, only the in situ loading stage could be used for mechanical characterization of the porous RP Ti6Al4V bone scaffolds.

Mechanical characterization of porous RP Ti6Al4V scaffolds produced with Concept machine was also carried out, resulting in worse mechanical properties and a rougher surface (verified via microscopy) for the same design parameters. The power of the laser of LM machine was higher, which led to a better melting and bonding between particles and, therefore, to higher mechanical properties and better surface finish. Therefore, Concept produced scaffolds were discarded, thus, no micro-CT combined with in situ loading was carried out on them.

Microhardness tests revealed that the hardness of the Ti6Al4V scaffolds produced via SLM with the LM machine was 398.5±14.9 HV, independent of the designed pore diameter. The actual hardness value was higher than the theoretical one, due to the presence of a martensitic phase in the microstructure.

Cyclic loading did not reveal any reliable results, due to technical problems. However, for future work, it would be advisable to use a load cell smaller than 30 kN and go further in strain value, approaching the yielding point.

Results from the continuous compression tests and Archimedes allowed finding a correlation between both the E modulus and the strength with the volume fraction for porous RP Ti6Al4V bone scaffolds produced with LM

machine. It was verified that Concept produced scaffolds did not fit these equations. Thus, they were not technique dependent, but machine dependent. These equations allowed predicting the E modulus and strength of porous RP Ti6Al4V bone scaffolds produced with LM machine, when knowing the volume fraction. Moreover, when another material is used with the same design and production parameters, the same equations can be applied.

$$\frac{E}{E_s} = 0.85\left(volumefraction\right)^{2.38} \text{ (MPa)} \qquad \text{eq. (7.7)}$$

$$\frac{\sigma_{ucs}}{\sigma_{ys}} = 0.39\left(volumefraction\right)^{2.04} \text{ (MPa)} \qquad \text{eq. (7.9)}$$

Values for the mechanical and morphological parameters always showed a small variation within the same design, which not only is indicative of the repeatability and good performance of SLM, but also meant that, for further research, a random scaffold could be considered as representative of those produced with the same designed parameters.

Morphological characterization of the assessed scaffolds was carried out at the preloaded stage, on the in situ loading stage placed inside the micro-CT. Micro-CT was proven to be an accurate method for the morphological characterization of the porous RP Ti6Al4V bone scaffolds, using volume fraction measured via Archimedes as a physical reference.

Stepwise compression loading combined with micro-CT imaging allowed studying the evolution of the morphological parameters of the scaffold under varying compressive load, thus, for different strain values, as well as deriving the failure mechanisms. Stepwise compression loading was concluded to be significantly different to the continuous one for porous RP Ti6Al4V bone scaffolds, since they are non linear elastic.

The strut size was found to be constant for every design and under any compressive load, which is indicative, again, of the repeatability and good performance of SLM in the production of porous Ti6Al4V bone scaffolds.

A first approach was done to the comprehension of the dependence of variables such as anisotropy or porosity on compressive load. However, it was not yet proven by analyzing the corresponding images, which is ongoing work. From a first analysis of the radiographic images, a dependence of the failure mechanism on the designed pore size was derived. However, it was concluded that the location of the onset of failure and a thorough understanding and/or characterization of the failure mechanisms of the porous RP Ti6Al4V bone scaffolds might be possible by studying the radiographic images corresponding to the different loading steps.

To sum up, a protocol was set up for further investigation on porous RP Ti6Al4V bone scaffolds via stepwise loading combined with intermediate micro-CT imaging.

10. Reference list

1988 Gibson, L. J. and M. F. Ashby, "Cellular Solids. Structure & Properties."1988.

1994 Boyer, R., G. Welsch and E. W. Collings, "Materials properties handbook: titanium alloys",ASM international, 1994.

1997 Hildebrand, T. and P. Ruegsegger, "A new method for the model independent assessment of thickness in three dimensional images." J.Microsc., 185,(67-75, 1997.

1998 Bart-Smith, H., A. F. Bastawros, D. R. Mumm, A. G. Evans, D. J. Sypeck and H. N. G. Wadley, "Compressive deformation and yielding mechanisms in cellular Al alloys determined using X-ray tomography and surface strain mapping." Acta Materialia, 46,(10): 3583-3592, 1998.

1999 De Man, B., J. Nuyts, P. Dupont, G. Marchal and P. Suetens, "Metal streak artifacts in X-ray computed tomography: A simulation study." Ieee Transactions on Nuclear Science, 46,(3): 691-696, 1999.

1999 Ding, M., A. Odgaard and I. Hvid, "Accuracy of cancellous bone volume fraction measured by micro-CT scanning." Journal of Biomechanics, 32,(3): 323-326, 1999.

1999 Schrooten, J., "Ontwikkeling en evaluatie van een Ti6Al4- oraal implantaat met een bioactieve glasdeklaag." Departement Metaalkunde, Katholieke Universiteit Leuven, 1999.

2000 De Man, B., J. Nuyts, P. Dupont, G. Marchal and P. Suetens, "Reduction of metal streak artifacts in x-ray computed tomography using a transmission maximum a posteriori algorithm." Ieee Transactions on Nuclear Science, 47,(3): 977-981, 2000.

2001 Kinney, J. H., G. W. Marshall, S. J. Marshall and D. L. Haupt, "Three-Dimensional Imaging of Large Compressive Deformations in Elastomeric Foams", Journal of Applied Polymer Science, 80,(1746-1755, 2001.

2002 Muller, R., T. Bösch, D. Jarak, M. Stauber, A. Nazarian, M. Tantillo and S. Boyd, "Micro-mechanical evaluation of bone microstructures under load." Proceedings of SPIE, 4503,(189-200, 2002.

2003 Hollander, D. A., T. Wirtz, M. Von Walter, R. Linker, A. Schultheis and O. Paar, "Development of Individual Three-Dimensional Bone Substitutes Using "Selective Laser Melting"." Eurpean Journal of Trauma, 2003.

2003 Kruth, J. P., Advances in selective laser sintering, International Conference on Advanced Research in Virtual an Rapid-prototyping, 2003.

2003 Sachlos, E. and J. T. Czernuszka, "Making tissue engineering scaffolds work. Review on the application of solid freeform fabrication technology to the production of tissue engineering scaffolds." European Cells and Materials, 5,(2003.

2004 Hutmacher, D. W., M. Sittinger and M. V. Risbud, "Scaffold-based tissue engineering: rationale for computer-aided design and solid free-form fabrication systems." Trends in Biotechnology, 22,(7): 354-362, 2004.

2004 Nazarian, A. and R. Muller, "Time-lapsed microstructural imaging of bone failure behavior." Journal of Biomechanics, 37,(1): 55-65, 2004.

2004 Van de Casteele, E., "Model-based approach for Beam Hardening Correction and Resolution Measurements in Microtomography." Faculteit Wetenschappen, Departement Natuurkunde, Universiteit Antwerpen, 2004.

2004 Yeong, W. Y., C. K. Chua, K. F. Leong and M. Chandrasekaran, "Rapid prototyping in tissue engineering: challenges and potential." Trends in Biotechnology, 22,(12): 643-652, 2004.

2005 Benouali, A. H., L. Froyen, T. Dillard, S. Forest and F. N'Guyen, "Investigation on the influence of cell shape anisotropy on the mechanical

performance of closed cell aluminium foams using micro-computed tomography." Journal of Materials Science, 40,(22): 5801-5811, 2005.

2005 Dillard, T., F. N'Guyen, E. Maire, L. Salvo, S. Forest, Y. Bienvenu, J. D. Bartout, M. Croset, R. Dendievel and P. Cloetens, "3D quantitative image analysis of open-cell nickel foams under tension and compression loading using X-ray microtomography." Philosophical Magazine, 85,(19): 2147-2175, 2005.

2005 Nagaraja, S., T. L. Couse and R. E. Guldberg, "Trabecular bone microdamage and microstructural stresses under uniaxial compression." Journal of Biomechanics, 38,(4): 707-716, 2005.

2005 Nazarian, A., M. Stauber and R. Muller, "Design and implementation of a novel mechanical testing system for cellular solids." Journal of Biomedical Materials Research Part B-Applied Biomaterials, 73B,(2): 400-411, 2005.

2006 Kerckhofs, G., J. Schrooten, M. Wevers, P. Van Marcke and V. Cleynenbreugel, "Standardisation and Validation of Micro-CT for the Morphological Characterisation of Porous Structures." ECNDT, 2006.

2006 Li, J. P., J. R. de Wijn, C. A. van Blitterswijk and K. de Groot, "Porous..." Biomaterials, 27,(1223-1235, 2006.

2006 Ohgaki, T., H. Toda, M. Kobayashi, K. Uesugi, M. Niinomi, T. Akahori, T. Kobayash, K. Makii and Y. Aruga, "In situ observations of compressive behaviour of aluminium foams by local tomography using high-resolution X-rays." Philosophical Magazine, 86,(28): 4417-4438, 2006.

2007 Li, J. P., P. Habibovic, M. van den Doel, C. E. Wilson, J. R. de Wijn, C. A. van Blitterswijk and K. de Groot, "Bone ingrowth in porous titanium implants produced by 3D fiber deposition." Biomaterials, 28,(18): 2810-2820, 2007.

Anexo. Resumen en español

Índice

Abstract

The present project dealt with the morphological and mechanical characterization of Ti6Al4V bone scaffolds produced by Selective Laser Melting, via micro-CT combined with in situ compressive loading. The in situ loading stage was first validated by proving that there was no difference between compressing the bone scaffolds on a conventional loading device, or on the in situ loading stage. Then, the effect of stepwise loading on the derived mechanical properties was assessed, showing a significant difference for the E-modulus, since the structures were non-linear elastic. It was seen that the variation of mechanical and morphological parameters for scaffolds with the same design within one production batch was neglectable. Thus, for future work, one random scaffold might be considered as representative for those produced with the same design. The influence of varying the pore size while keeping the strut size constant was assessed both morphologically and mechanically, setting up a protocol for future assessment of the scaffolds. The combination of micro-CT and in situ loading allowed to relate the failure mechanisms to the design and to locate the onset of failure by the change in morphological parameters.

Resumen

El presente proyecto trata de la caracterización morfológica y mecánica, vía micro-CT combinado con ensayos de compresión in situ, de escafoides para implantación ósea de Ti6Al4V fabricados por Selective Laser Melting. La máquina de compresión in situ fue validada comprobando que no existían diferencias entre la realización de ensayos de compresión en una máquina de ensayo convencional y la máquina in situ. A continuación se evaluó el efecto de la compresión escalonada en las propiedades mecánicas, que indicó una diferencia significativa en el módulo E debido a que las estructuras tenían un comportamiento elástico no lineal. Se constató que la variación de las propiedades mecánicas y morfológicas era pequeña para escafoides con el mismo diseño y del mismo lote. De este modo, en el futuro, un escafoide escogido al azar podría considerarse representativo del lote de aquellos fabricados a partir del mismo diseño. La influencia de variar el tamaño de poro de los escafoides manteniendo constante el tamaño de columna fue evaluada tanto morfológica como mecánicamente, estableciendo un protocolo para trabajos futuros. La combinación de ensayos de compresión in situ con la toma de imágenes por micro-CT permitió relacionar el mecanismo de fractura con el diseño, además de la localización del instante de inicio de la fractura mediante el cambio en los parámetros morfológicos.

1. Antecedentes

1.1. Introducción

Un sólido poroso es aquel formado por una red interconectada de láminas o columnas sólidas que constituyen los lados o caras de los poros. Los materiales porosos son muy comunes en la naturaleza: la madera, el corcho, la materia ósea o la esponja. El hombre se ha valido de ellos durante siglos y, más recientemente, ha creado algunos nuevos. Entre ellos pueden encontrarse los materiales con estructura nido de abeja y las espumas metálicas, poliméricas o cerámicas. Hoy en día se puede hacer espuma de casi cualquier material. Además, se pueden fabricar materiales porosos a partir de metales, cerámicos, vidrios e incluso de materiales compuestos.

La característica más notable de un sólido poroso es su *densidad relativa* ρ^*/ρ_s; esto es, la densidad del material poroso, ρ^*, dividida por la densidad del sólido que compone las paredes de los poros, ρ_s. La baja densidad de los materiales porosos da lugar a altas propiedades específicas. El aislamiento térmico, el embalaje, el uso estructural y la flotabilidad han sido tradicionalmente las cuatro áreas en las que más se han empleado los materiales porosos. Sin embargo, el uso biomédico está adquiriendo importancia últimamente.

Los materiales porosos podrían conducir a grandes mejoras usados para imitar a la naturaleza, que es el objetivo principal de la Ingeniería de Tejidos (IT) (Sachlos and Czernuszka [2003; Yeong et al. [2004]). La IT es un campo interdisciplinar que aplica los principios de la ingeniería y las ciencias biosanitarias en el desarrollo de sustitutos biológicos que restauran, mantienen o mejoran la función de un tejido. Esto se consigue implantando células en matrices porosas conocidas como escafoides. Dicho de otro modo, los escafoides tratan de imitar la función de la matriz intercelular natural proporcionando un sustento temporal para el crecimiento del tejido.

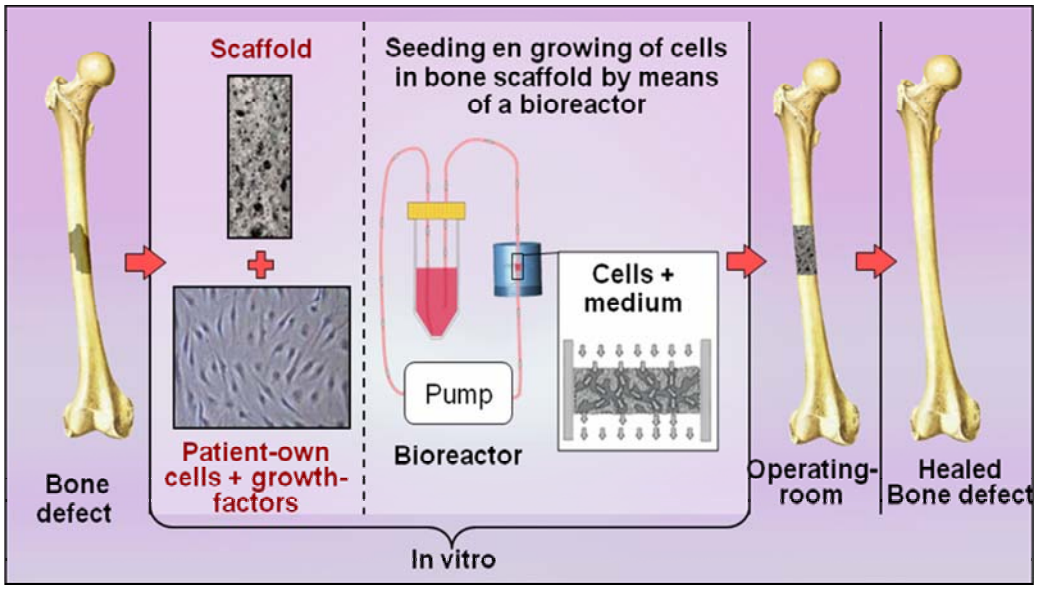

Fig.1.1. Visión esquemática general de la ingeniería ósea de tejidos.

Además de la densidad son numerosas las características que han sido calificadas como cruciales en la producción de escafoides para IT (Sachlos and Czernuszka [2003]). Éstos deberían:

- Poseer poros interconectados de dimensiones (tamaño de poro, geometría de poro y tamaño de porosidad interconectada) tales que favorezcan la integración y vascularización del tejido.
- Estar fabricados de un material bioinerte, como el Ti6Al4V, o con una biodegradabilidad controlada de manera que finalmente el tejido nuevo restaure sus funciones y deje de necesitar el escafoide como soporte.
- Tener una química de superficie que favorezca el acoplamiento, diferenciación y proliferación del tejido.
- No inducir reacciones adversas.
- Ser fácilmente fabricados en una gran variedad de geometrías y tamaños.
- Tener unas propiedades mecánicas acordes con el lugar de implantación.

Se observa que las características que los escafoides han de poseer pueden clasificarse en dos grupos: el relativo al campo médico y el relacionado con la ingeniería.

Este proyecto se ha centrado en la parte que a la ingeniería concierne y, más concretamente, en la combinación de ensayos de compresión con toma de imágenes vía micro-CT con el objetivo de determinar la morfología y las consiguientes propiedades mecánicas de escafoides para implantación ósea de Ti6Al4V. La ingeniería de huesos es un campo que pertenece a la IT. Tras una fractura, enfermedad ósea u otras condiciones que derivan en pérdida ósea, los materiales porosos ofrecen la posibilidad de sustituir la materia ósea de manera casi impecable. Conviene no olvidar que el hecho de que se utilicen materiales porosos en este campo se debe a que los huesos son materiales porosos.

1.2. Métodos de producción

Los métodos convencionales de producción de escafoides de IT incluyen, entre otros, las siguientes técnicas: solvent-casting particulate-leaching, gas foaming, fiber meshes and fiber bonding, phase separation, melt molding, emulsion freeze drying, solution casting or freeze drying.

No obstante, estas técnicas tienen una capacidad reducida en lo que a control de la geometría del poro y a la interconectividad y distribución espacial de los poros se refiere.

En la IT la tendencia es dejar de lado el uso de espumas de microestructuras aleatorias en favor de estructuras de geometría altamente controlable que permitan una mayor comprensión del papel que juegan los aspectos morfológicos y mecánicos de los escafoides en la práctica.

Las técnicas de Rapid Prototyping (RP) permiten lograr ese control sobre el diseño de las estructuras. RP engloba un grupo de técnicas que pueden generar una estructura física partiendo de información en CAD (Computer Aided

Design). El hecho de que, basándose en un modelo 3D en CAD, un programa corte en rodajas de grosor constante la pieza virtual (Hollander et al. [2003]) permite fabricar escafoides con la forma exterior deseada y una morfología interna predefinida y reproducible (Sachlos and Czernuszka [2003]) posibilitando una IT adaptable a necesidades individuales (Hutmacher et al. [2004]). Además, el uso de técnicas RP podría reducir el tiempo y coste de fabricación de los escafoides significativamente en comparación con las técnicas convencionales (Hollander et al. [2003]).

El potencial de 3D fiber deposition (3DFD) ha sido demostrado en la fabricación de escafoides tridimensionales de Ti6Al4V con una aquitectura regular y repoducible que satisface los requisitos de la IT. También se ha estudiado cómo influyen las características estructurales (porosidad, geometría del poro) de estos escafoides en el crecimiento óseo (Li et al. [2006]).

Para este proyecto se han fabricado escafoides de Ti6Al4V mediante una técnica RP llamada Selective Laser Melting (SLM). La Fig.1.2. muestra un escafoide poroso de los que han sido analizados.

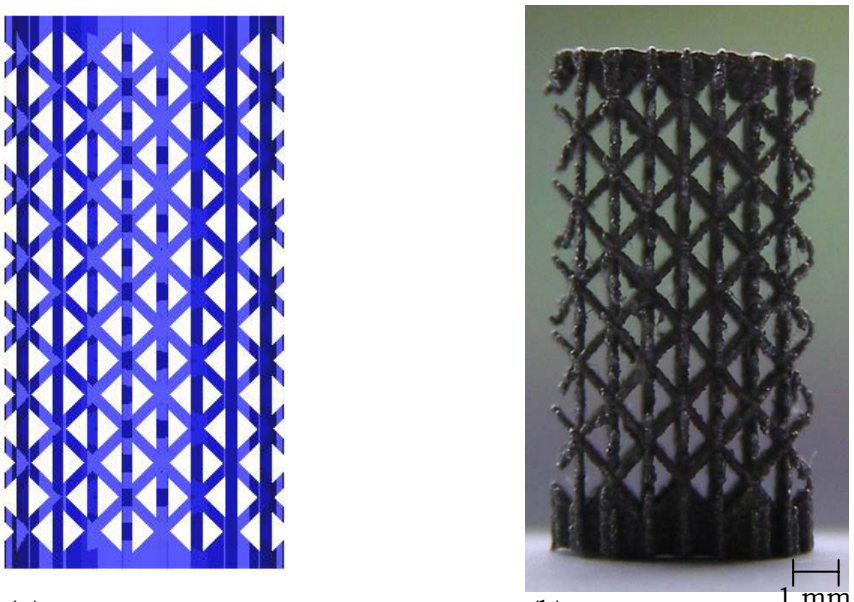

(a) *(b)*

Fig.1.2. *(a)* Diseño en CAD de un escafoide poroso de Ti6Al4V *(b)* Fotografía de un escafoide poroso de Ti6Al4V fabricado por SLM.

El punto de partida del SLM es un modelo tridimensional generado por CAD que a continuación es subdividido en rodajas de un grosor definido. La pieza física se genera mediante un proceso repetitivo en el que se aplican nuevas capas de material al que se transfiere la información sobre el área y el contorno utilizando un haz láser (Fig.1.3)(Hollander et al. [2003]). El proceso se traduce en una unión completa entre capas y una densidad de aproximadamente el 100%. Este método ya ha sido empleado para la fabricación de sustitutos óseos biocompatibles de Ti6Al4V (Hollander et al. [2003]).

Se ha de tener en cuenta que la resolución de las técnicas RP es limitada, lo cual introduce cierta variabilidad en la geometría de la estructura fabricada. Esta variabilidad podría ser relativamente alta, sobre todo si se trabaja cerca de los límites físicos de producción. En el caso de la IT es esencial trabajar en torno

a esos límites, puesto que no se debe olvidar que el fin último es implantar los escafoides y que las células crezcan en él. Por ello, aunque es bien sabido que el Ti6Al4V es un material biocompatible, es necesario estudiar las propiedades mecánicas de los escafoides fabricados por SLM. Además, sería muy útil caracterizarlos también morfológicamente para ver cuán robusta y exacta es la técnica de producción.

Desde un punto de vista más global, el modelo en CAD podría servir como dato de entrada para un FEA (Finite Element Análisis), cuyo objetivo es predecir el comportamiento mecánico de una estructura bajo cualquier estado tensional. Puesto que es probable que el SLM no reproduzca perfectamente el modelo CAD, el modelo de FE (Finite Element) podría completarse y mejorarse con la información obtenida de la caracterización mecánica y morfológica de los escafoides. Cuando el FEA fuese capaz de simular la realidad (no el modelo en CAD), sería una fuente fiable de la que extraer el diseño que mejor satisfaga los requisitos ingenieriles, médicos y biológicos deseados. Ese diseño "perfecto" podría entonces ser convertido a CAD y posteriormente fabricado.

1.3. Técnicas de caracterización empleadas hasta el momento

En este proyecto se han analizado, mediante ensayos de compresión in situ combinados con la toma de imágenes vía micro-CT, las propiedades morfológicas y mecánicas de escafoides porosos para implantación ósea de Ti6Al4V producidos por SLM. Micro-CT es una técnica relativamente nueva para la caracterización de materiales porosos.

El micro-CT proporciona un mapa tridimensional de alta resolución del coeficiente de absorción μ de un material, lo cual permite visualizar y analizar su microestructura. No obstante, también puede llevarse a cabo un análisis cuantitativo de imágenes 3D del mapa. Mediante la combinación de micro-CT y el análisis de imágenes 3D puede obtenerse una amplia descripción de la microestructura de un material poroso que no sería posible mediante otros métodos (Benouali et al. [2005]).

Por otro lado, el análisis mecánico de los materiales porosos es esencial para cualquier aplicación estructural. El ensayo de compresión está muy extendido y provee de información útil como el módulo de Young (E), la tensión de rotura (σ_R) y la deformación de rotura (ε_R). Este ensayo resulta muy apropiado para materiales como el Ti6Al4V fabricado por RP, que tiene un comportamiento muy poco reproducible a tracción.

Los ensayos de compresión, combinados con la toma de imágenes vía micro-CT, han sido utilizados en numerosas ocasiones para el estudio de materiales porosos. Como puede leerse a continuación, la combinación de ambas técnicas permite estudiar en profundidad la relación entre morfología, propiedades mecánicas y el comportamiento a rotura de los materiales porosos. En este caso, sin embargo, se han realizado ensayos de compresión escalonados para estudiar la evolución del material bajo estados incrementales de tensión. Por ello, no se debería olvidar que el comportamiento del material podría diferir de aquel en ensayos continuos de compresión.

Los mecanismos de deformación de espumas de aluminio de porosidad abierta y cerrada bajo estados de compresión fueron establecidos por Bart-Smith et al. [Ref.] mediante el uso de CT de rayos-X y "surface strain mapping". La máquina de compresión no estaba situada dentro de la máquina de CT, lo cual implicó traslados de una a otra. Se concluyó que la deformación parecía estar estrechamente relacionada con la geometría del poro. Por lo tanto, la mejora de las propiedades mecánicas pasaría por controlar la geometría de los poros durante el proceso de fabricación, que es algo que el SLM permite.

Dillard et al. [Ref.] emplearon una máquina de tensión-compresión especialmente diseñada para permitir la observación de la deformación mediante micro-CT, lo que posibilitó el análisis del mecanismo de deformación y fractura de una espuma de porosidad abierta de níquel.

El hueso trabecular también ha sido objeto de numerosos estudios llevados a cabo mediante micro-CT y análisis mecánico.

Nagaraja et al. [Ref.] evaluaron el mecanismo de deformación y fractura de hueso trabecular bajo diferentes niveles de compresión uniaxial mediante la combinación de micro-CT y "sequential fluorescent staining". Cabe destacar que, en este caso, los mecanismos de deformación y fractura no difirieron en compresión y compresión escalonada. Es más, no es el primer artículo sobre hueso trabecular en afirmar este hecho. También lo han hecho Nazarian et al. [Ref.], Nazarian y Muller [Ref.] y Nazarian y Muller [Ref.]. Si esto es o no aplicable a los escafoides de Ti6Al4V fabricados por RP es todavía una incógnita.

Nazarian y Muller [Ref.] emplearon la microcompresión escalonada combinada con la toma de imágenes vía micro-CT para el análisis de la progresión de la fractura del hueso trabecular. Tras cada etapa de deformación se iniciaba una etapa de relajación de los especímenes de una duración de 20 minutos, que permitía su asentamiento antes de su traslado a la máquina de micro-CT.

Muller et al. [Ref.] emplearon el micro-CT combinado con ensayos de tracción para visualizar, cuantificar y analizar los mecanismos de propagación de la fractura del hueso trabecular. La máquina de tracción no estaba situada dentro de la micro-CT. El tener que trasladar la muestra de una máquina a otra se tradujo en que los escaneos del micro-CT no estaban siempre alineados de igual manera respecto al sistema global de coordenadas definido por el micro-CT. Este artificio pudo ser subsanado, pero no ocurriría de estar la máquina de tracción dentro del micro-CT. Es decir, situar la máquina de tracción dentro de la máquina de micro-CT evitaría los errores derivados del traslado de la muestra.

2. Objetivos del proyecto

De los estudios realizados hasta este momento se puede concluir que el SLM, que es una técnica de RP, es muy adecuado para la fabricación de escafoides, pues permite un alto control del tamaño, geometría, interconectividad y distribución de los poros. También ha sido demostrado que los escafoides de Ti6Al4V producidos de esta manera son biocompatibles. Sin embargo, es muy importante verificar que el proceso de producción es robusto en lo que a parámetros mecánicos y morfológicos se refiere, lo cual es uno de los objetivos del proyecto. Se empleará para ello la toma de imágenes vía micro-CT, el análisis

de las mismas y los ensayos de compresión in situ. Con el objetivo de eludir los problemas derivados del traslado de la muestra de la micro-CT a la máquina de compresión y viceversa, se ha desarrollado una nueva máquina de compresión que puede situarse dentro de la micro-CT. El estudio de la exactitud y fiabilidad de esta nueva máquina forma también parte de este proyecto.

Se afirmó que en el caso del hueso trabecular no existen diferencias entre los resultados obtenidos tras la compresión continua y la escalonada. En este proyecto se analizará si esto ocurre para el caso de los escafoides porosos de Ti6Al4V fabricados por SLM.

El método de producción (SLM) será evaluado mediante: (i) la comparación de escafoides fabricados a partir del mismo diseño con dos máquinas diferentes (ii) el estudio de la variabilidad dentro de un mismo lote, fabricado en la misma máquina y partiendo de igual diseño.

En primer lugar se fabricarán escafoides macizos con dos máquinas distintas, lo que permitirá comparar los valores experimentales obtenidos de los ensayos de compresión con los teóricos para el Ti6Al4V. Los escafoides para uso biomédico son siempre porosos, por lo que tras este primer análisis se procederá al estudio de únicamente escafoides porosos, fabricados con ambas máquinas.

Se llevará a cabo una comparación entre los resultados obtenidos de los ensayos de compresión en la máquina de ensayos recién desarrollada y una máquina convencional para demostrar la fiabilidad de la primera.

Con el objetivo de relacionar las características morfológicas de diseño, las experimentales y las propiedades mecánicas de los escafoides, y comprobar si existen diferencias entre los ensayos de compresión continuos y los escalonados, se llevarán a cabo idénticos ensayos en escafoides fabricados con la misma máquina pero con diferentes tamaños de poro.

Este proyecto pretende, finalmente, establecer un protocolo para el análisis de escafoides porosos para implantación ósea de Ti6Al4V fabricados vía SLM. El presente trabajo y futuros estudios podrían además, emplearse para mejorar el diseño de los escafoides, su modelado en Elementos Finitos y conocer la relación entre diseño y escafoide fabricado, con el fin últimos de fabricar el escafoide perfecto desde el punto de vista ingenieril, médico y biológico.

3. Proceso experimental

3.1. Materiales empleados

Los escafoides estudiados en este proyecto fueron producidos a partir de polvo de Ti6Al4V recocido, cuyas características se especifican en la Tabla.3.1. La información de dicha tabla debería considerarse meramente indicativa, pues corresponde a Ti6Al4V recocido mientras que, tras el SLM, el Ti6Al4V tendrá características más cercanas al templado.

Tabla3.1. Especificaciones del polvo de Ti6Al4V.

Densidad	4.42 g/cm³
Tensión Máxima	1000 MPa
Límite Elástico	920 MPa
Deformación Máxima	12%
Módulo E	110 GPa
Temperatura de Fusión	1649°C
Tamaño de partícula medio	35 μm

Se fabricaron, vía SLM, escafoides a partir del citado polvo de Ti6Al4V partiendo de cuatro diseños en CAD. En la Fig.3.1 se muestran el diseño de un escafoide en CAD (punto de partida para la fabricación por SLM) y un escafoide fabricado. La única diferencia entre los distintos diseños en CAD estriba en el tamaño de poro. Todas las muestras tenían la misma celda unidad (Fig.3.1) y eran cilíndricas, de radio de 3.00 ± 0.05 mm y altura de 12.0 ± 0.5 mm. Se disponía, en la Katholieke Universiteit Leuven (Bélgica), de dos máquinas (LM y Concept) capaces de fabricar los escafoides vía SLM. Por ello, se decidió emplear ambas máquinas para ciertos diseños en CAD, con el objetivo de compararlas. La LM es una máquina que se desarrolló en la propia Katholieke Universiteit Leuven, mientras que la Concept es una máquina disponible en el mercado.

Tabla3.2. Características de los diseños de los escafoides.

	Diámetro de columna (mm)	**Tamaño de poro (mm)**	**Máquina SLM**
s0.1p0.8	0.1	0.8	LM
s0.1p1	0.1	1	LM
s0.1p1Concept	0.1	1	Concept
s0.1p1.2	0.1	1.2	LM
BulkLM	-	0 (escafoide macizo)	LM
BulkConcept	-	0 (escafoide macizo)	Concept

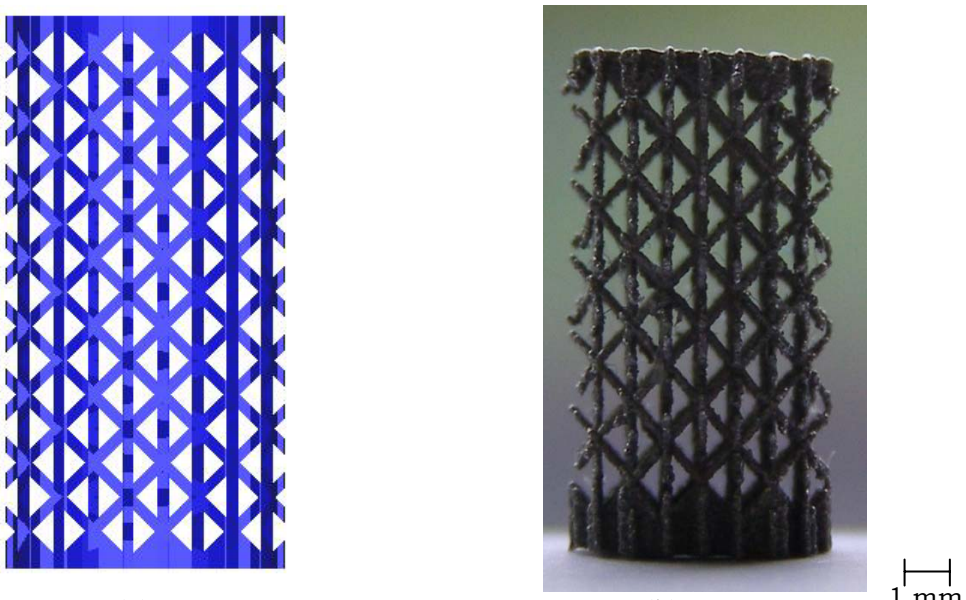

(a) (b)

Fig.3.1. *(a)* Diseño en CAD de un escafoide poroso *(b)* Fotografía de un escafoide poroso de Ti6Al4V fabricado vía SLM.

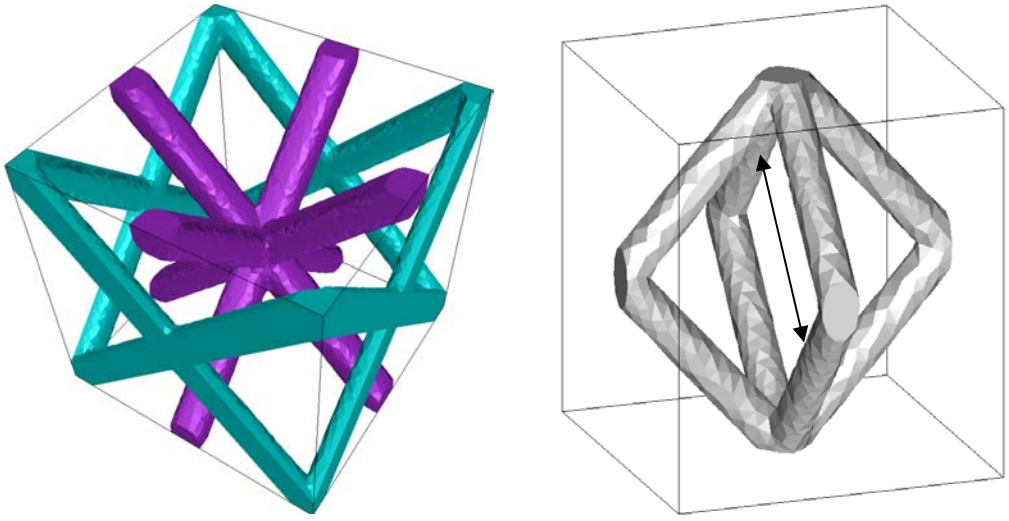

(a) *(b)*

Fig.3.2. *(a)* celda unidad del escafoide. *(b)* celda unidad simplificada del escafoide en la que el tamaño de poro está definido con una flecha negra.

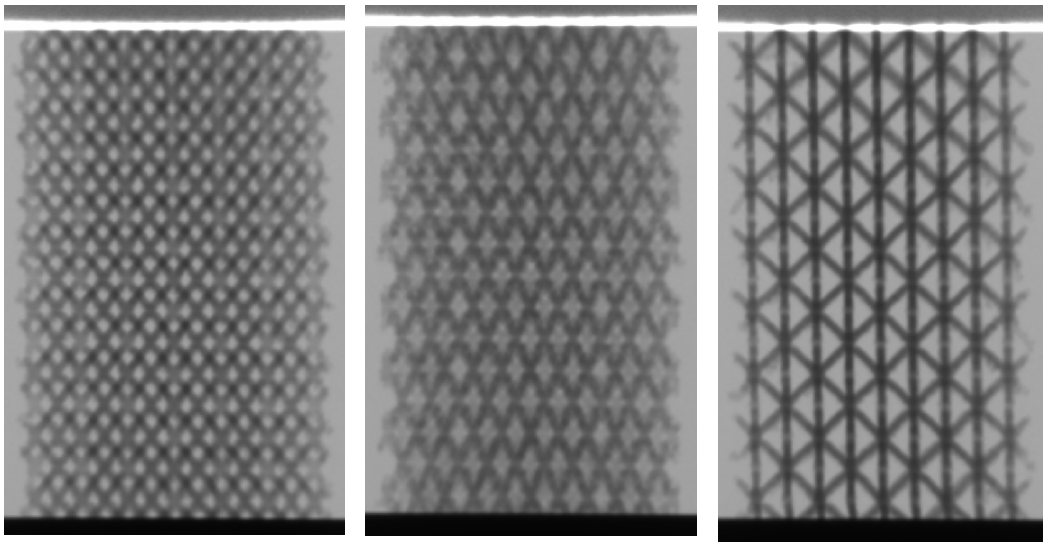

Fig.3.3.Imágenes radiográficas tomadas vía micro-CT de una muestra s0.1p0.8.

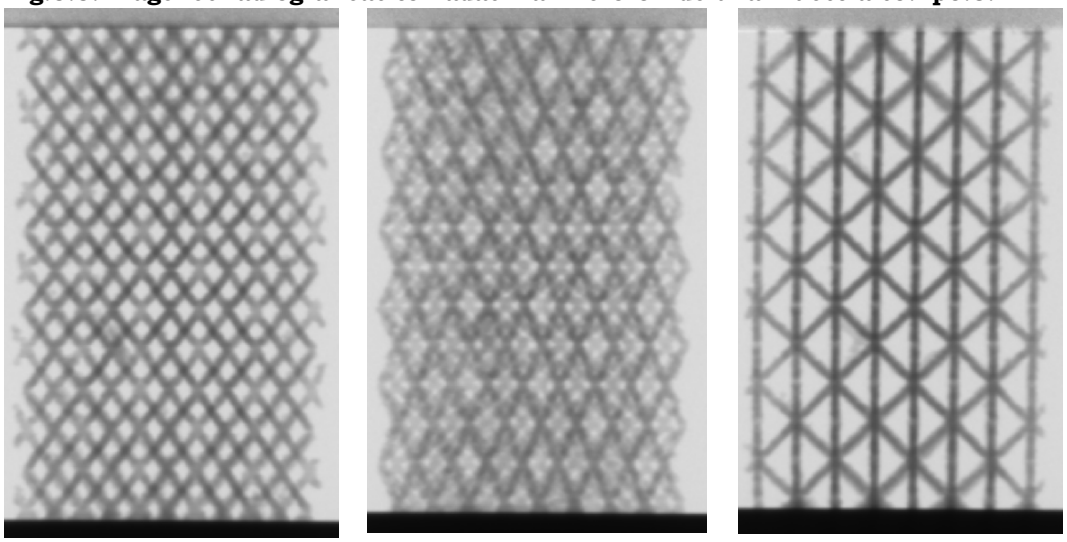

Fig.3.4. Imágenes radiográficas tomadas vía micro-CT de una muestra s0.1p1.

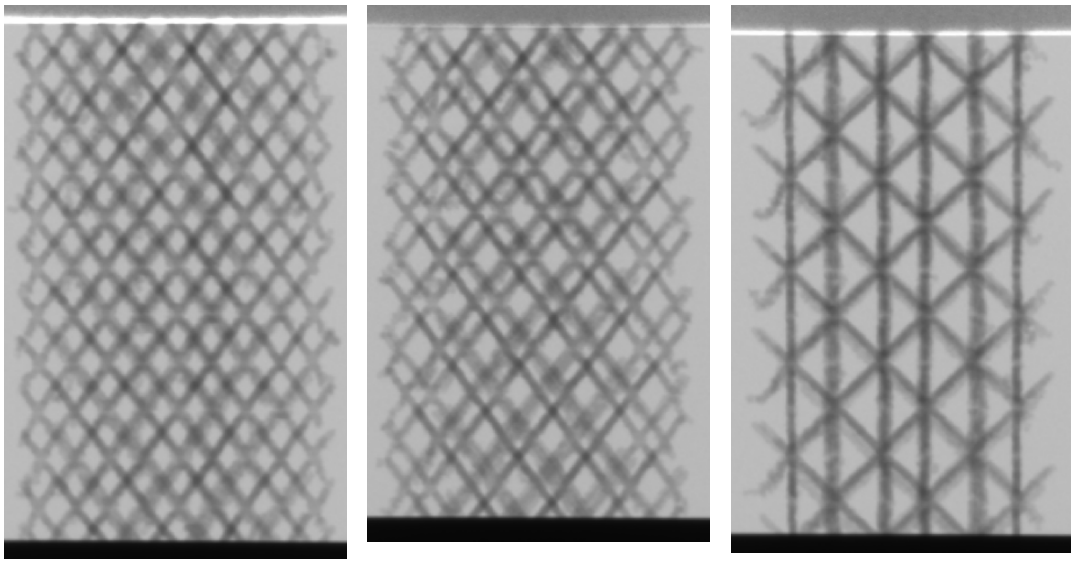

Fig.3.5. Imágenes radiográficas tomadas vía micro-CT de una muestra s0.1p1.2.

3.2. Técnicas empleadas

A continuación se detallan las técnicas que se emplearon para la caracterización mecánica y morfológica de los escafoides de Ti6Al4V fabricados vía SLM.

3.2.1. Medida de densidad por Arquímedes

Se realizaron ensayos de Arquímedes con una Sartorious YDK 01, YDK 01-0D Density Determitation Kit, con el objetivo de determinar la porosidad de los escafoides porosos.

3.2.2. Análisis por microscopía

Se analizó un escafoide poroso por cada tamaño de poro mediante microscopía. Para ello se hizo la siguiente preparación de las muestras:

1. Medición de las dimensiones de la muestra con una calibre electrónico.

2. Embuticióon de las muestras.

3. Cortado, desbaste y pulido.

4. Microscopía: fotografiado de la superficie pulida.

   Se tomaron entre 20 y 24 imágenes de la superficie de cada muestra con la menor magnificación disponible (PL 8x1) con un microscopio óptico (Metalloplan, Germany) al que se había acoplado una cámara CCD.

5. Pegado y binarización de las imágenes.

   La reconstrucción de cada superficie se hizo, a partir de las 20-24 fotografías, utilizando Panavue Image Assembler, que es un software para el pegado de fotos digital (http://www.panavue.com). Posteriormente las fotografías fueron convertidas a imágenes de 8 bits mediante Corel PHOTO-PAINT X3 para luego binarizarlas con CTAnalyzer [Skyscan NV, Kontich, Belgium].

3.2.3. Microdureza

Se realizaron ensayos de microdureza Vickers con una Leitz Durimet con una carga de 100g en las muestras que habían sido previamente analizadas por microscopía. Las mediciones de dureza se llevaron a cabo vía ocular con la ayuda de una cámara CCD.

3.2.4. Ensayos mecánicos

Los ensayos mecánicos son requisito indispensable para cualquier aplicación estructural. En este caso se escogió realizar ensayos de compresión y ensayos cíclicos para la caracterización mecánica de los escafoides de Ti6Al4V. El motivo de ensayar a compresión es que los materiales metálicos como el Ti6Al4V tienen un comportamiento más estable y menos disperso a compresión que a tracción.

Como se describe en apartados posteriores, se realizaron ensayos de compresión en una Instron4505 y en la nueva máquina de ensayo in situ (in situ loading stage) en todos los escafoides porosos (s0.1p0.8, s0.1p1, s0.1p1.2 y s0.1p1Concept). La razón de que se llevaran a cabo idénticos ensayos en las dos máquinas es que la máquina de ensayo in situ, en la que posteriormente se realizarían los ensayos de compresión escalonados combinados con la toma de imágenes por micro-CT necesitaba todavía ser calibrada y validada.

El objetivo principal de los ensayos de compresión era obtener las propiedades mecánicas de los escafoides porosos dependiendo de su tamaño de poro y ver si se podía encontrar una relación entre ambos. No obstante, la información obtenida permitió profundizar en temas tales como: (i) comparación de las dos máquinas de SLM mediante la comparación de los diseños s0.1p1 y s0.1p1Concept, (ii) evaluación de la robustez de la técnica de producción (SLM) mediante la comparación de muestras de igual diseño en CAD del mismo lote, (iii) comparación de los resultados obtenidos en las dos máquinas de compresión y (iv) comparación de los ensayos de compresión continuos y escalonados (ambos llevados a cabo en la máquina de ensayos in situ).

Conviene no olvidar que el objetivo final es la implantación de los escafoides para sustituir materia ósea situación en la que trabajarán bajo tensiones cíclicas. Es por ello que se ha pretendido hacer un análisis de los escafoides mediante ensayos cíclicos de compresión-relajación.

En ambos ensayos se evaluaron los siguientes tres parámetros mecánicos para cada muestra:

1. **E** (MPa), Módulo de Young.

La estructura a analizar no tiene un comportamiento elástico lineal, lo que significa que el módulo E no se puede hallar con la ley de Hooke. Esto dificulta definir un único módulo E por lo que se escogió el método descrito por Kinney et al. [Ref.], que se aplicó al cálculo del módulo E de espumas elastoméricas con un acusado comportamiento elástico no lineal. El procedimiento para el cálculo del módulo E de los escafoides de Ti6Al4V fue el siguiente:

I. Se ajustó un polinomio de cuarto orden a la curva de tensión-deformación entre el primer punto de la gráfica y la tensión de rotura (Fig.3.6).

II. Se representó la derivada del polinomio (es decir, E) en función de la deformación.

III. Se tomó como módulo de Young el máximo de la gráfica arriba descrita (Fig.3.7)

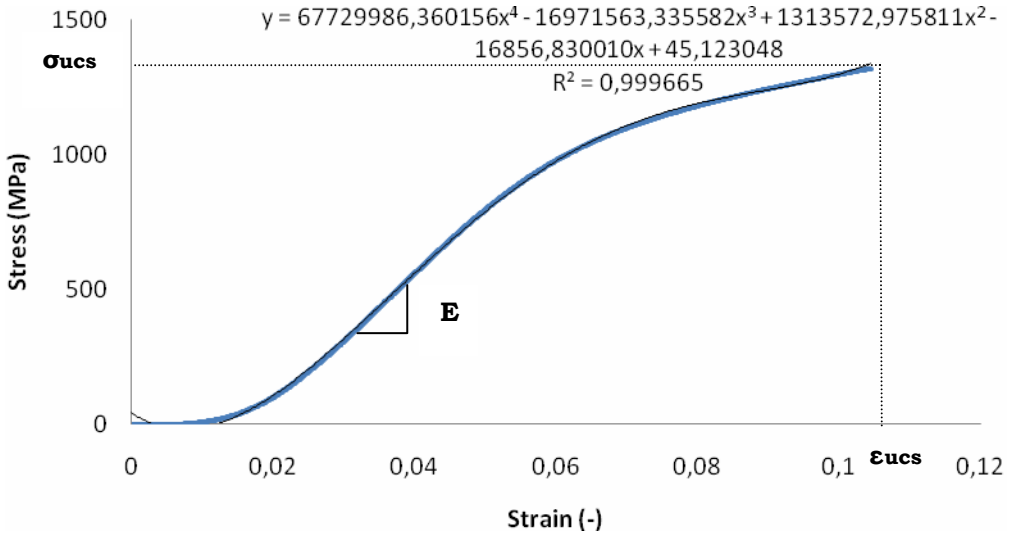

Fig.3.6. Curva tensión-deformación a la que se ha ajustado un polinomio de orden 4.

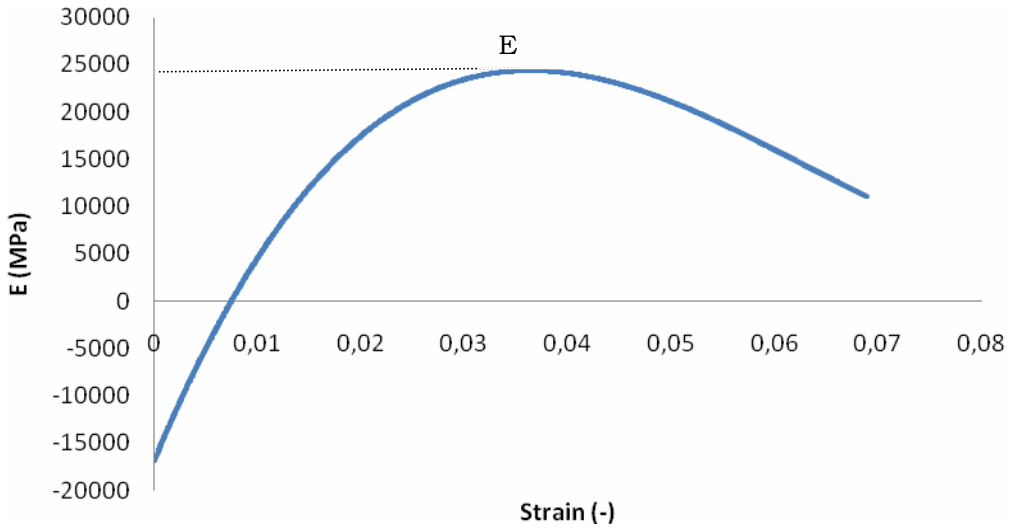

Fig.3.7. Representación de la variación de E con la deformación. Se ha asumido el máximo de esta gráfica como módulo E de la muestra.

2. σ_R (MPa), tensión de rotura.

3. ε_R, deformación de rotura.

3.2.4.1. Ensayos de compresión continuos con máquina de ensayos convencional

Tanto en las muestras porosas como en las macizas se llevaron a cabo ensayos continuos de compresión en una INSTRON 4505. En todos los casos la velocidad de ensayo fue de 0.15 mm/min y la precarga la menor posible, que no puedo ser siempre la misma puesto que tenía que ser aplicada manualmente mediante la inducción de pequeños desplazamientos. La única diferencia fue que

se empleó una célula de carga de 100 kN en el caso de los escafoides macizos y una de 5 kN para los porosos.

3.2.4.2. Ensayos de compresión continuos, cíclicos y escalonados (combinados con micro-CT) con la máquina in situ.

La máquina de ensayos in situ se situó dentro de la máquina de micro-CT, tal y como se muestra en la Fig.3.8. Se empleó para realizar ensayos de compresión continuos, escalonados y cíclicos en estructuras porosas s0.1p0.8, s0.1p1, s0.1p1Concept y s0.1p1.2.

Fig.3.8. Máquina de ensayos in situ, situada dentro del micro-CT, del cual puede verse la fuente de rayos-X.

Los ensayos de compresión continuos, en los que la variable sobre la que se podía actuar era la carga, se realizaron a una velocidad de ensayo de 0.2 mm/min y con una precarga de 0.01 kN.

En los ensayos cíclicos las muestras se sometieron a 10 ciclos (20 etapas) de compresión-relajación, en los que la variable sobre la que se podía actuar era el desplazamiento, a una velocidad de ensayo de 0.2 mm/min, etapas de desplazamiento 0.25 mm y una precarga de 0.01 kN.

En los ensayos de compresión escalonados la velocidad de ensayo fue de 0.2 mm/min, escalones de desplazamiento de 0.2 mm (6-7 escalones por muestra) y una precarga de 0.01 kN, siendo el desplazamiento la variable sobre la que se podía actuar. Para caracterizar la morfología y el comportamiento a

compresión de los escafoides porosos de Ti6Al4V se empleó la micro-CT (junto con el software de reconstrucción de imágenes Skyscan) combinada con ensayos de compresión escalonados. Se decidió analizar únicamente los escafoides fabricados con la máquina LM debido a que sus propiedades mecánicas eran mejores que las de los escafoides fabricados con la Concept.

El procedimiento con cada muestra fue el siguiente:

1. Medición de las dimensiones de la muestra con un calibre electrónico.

2. Precarga de la muestra a 0.01 kN en la máquina de ensayos in situ.

3. Rotación de la muestra para permitir su asentamiento antes del escaneo y evitar movimientos durante el escaneo.

4. Escaneo 3D de la muestra a 90 kV y la máxima intensidad (mA) permitida con un filtro de aluminio de espesor 1 mm detrás de la fuente de rayos-X (Kerckhofs et al. [Ref.]), "frame averaging" de 16 y un incremento angular de 0.5º. El tiempo empleado para realizar un escaneo tridimensional completo junto con el correspondiente incremento de desplazamiento era de alrededor de 20 minutos.

5. Repetición del escaneo 6 o 7 veces. La primera de ellas tras la aplicación de la precarga y las siguientes en intervalos de incremento de desplazamiento de 0.2 mm, tal y como muestra la Fig.3.9.

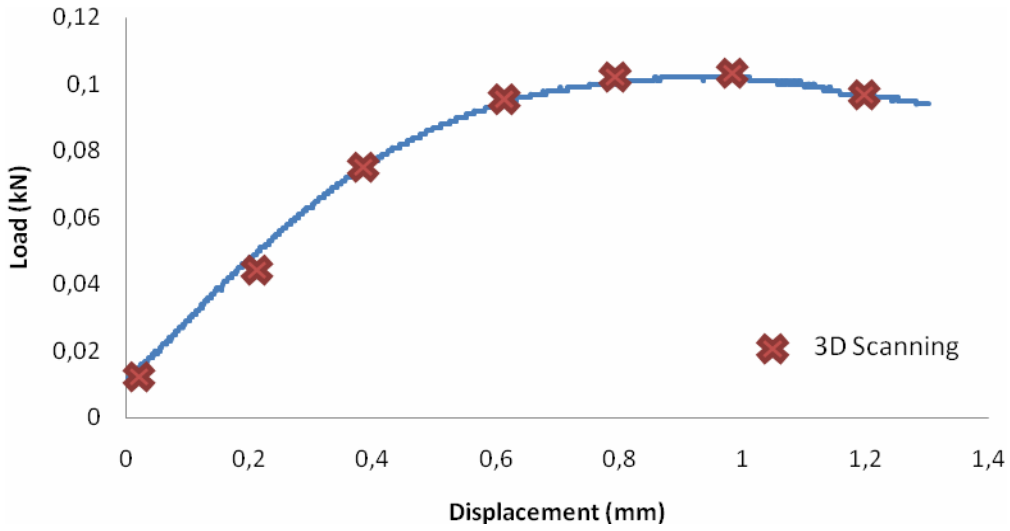

Fig.3.9. El escaneo 3D se realizaba en estado de precarga e intervalos de incremento de desplazamiento de 0.2 mm.

6. Conversión de los archivos radiográficos a archivos tiff de 8 bits en escala de grises para posibilitar su posterior reconstrucción utilizando el software de reconstrucción volumétrica de Skyscan, denominado Nrecon. Nrecon genera un grupo de rodajas trasversales a lo largo del objeto partiendo de las proyecciones angulares obtenidas vía micro-CT. Finalmente, se utilizó un programa informático llamado CTAn para hacer un análisis tridimensional de los datos generados por Nrecon.

El objetivo principal de escalonar el ensayo de compresión fue permitir la toma de imágenes de los escafoides vía micro-CT a diferentes niveles de deformación. Sin embargo, también dio lugar a la comparación de las propiedades mecánicas derivadas de los ensayos continuos y los escalonados. En la Fig.3.10 se muestra una curva de tensión deformación típica producto del ensayo de compresión escalonado sobre uno de los escafoides.

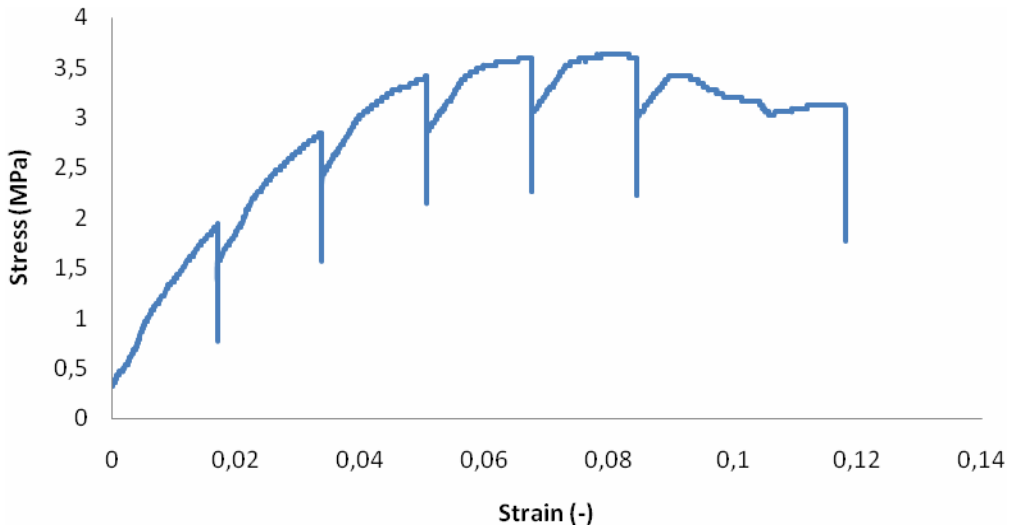

Fig.3.10. Curva típica de tensión deformación en un ensayo de compresión escalonado.

El módulo E se calculó de igual manera que en los ensayos de compresión continuos para permitir la comparación de las propiedades mecánicas derivadas de ambos. Para ello hubo que suprimir los puntos de las gráficas correspondientes al tiempo de escaneo y relajación utilizando una función lógica de Excel (ec.3.1).

IF(stress X+1 < stress X, stress X, stress X+1) ec.(3.1)

4. Resultados y discusión.

A continuación se detallan los resultados y discusión consecuencia de aplicar las técnicas descritas en el apartado anterior en los escafoides de Ti6Al4V producidos por SLM.

4.1. Medida de densidad por Arquímedes

El objetivo de realizar ensayos de medida de densidad por Arquímedes fue conocer la porosidad de los escafoides porosos de Ti6Al4V fabricados por SLM. Los resultados se muestran en la Tabla4.1.

Tabla4.1. Resultados de los ensayos de Arquímedes. (n=5)

	Porosidad (%)
s0.1p0.8	85.28 ± 0.49
s0.1p1	88.13 ± 0.10
s0.1p1Concept	89.76 ± 0.08
s0.1p1.2	92.24 ± 0.15

A pesar de que los parámetros de diseño fueron los mismos para s0.1p1 y s0.1p1Concept, es decir, se partió del mismo diseño en CAD para su producción, se observa que la porosidad de los escafoides difiere dependiendo de la máquina con que se han fabricado.

En general, los resultados muestran que la porosidad aumenta al incrementar el tamaño de poro del diseño.

Los datos obtenidos de los ensayos de Arquímedes se emplearon para definir el rango óptimo para la reconstrucción de las imágenes obtenidas vía micro-CT (Ding et al. [Ref]).

4.2. Análisis por microscopía

El objetivo inicial de la toma de imágenes con el microscopio era hacer un análisis bidimesional de las imágenes y comparar los resultados con aquellos obtenidos mediante un análisis 2D de la información obtenida vía micro-CT. De esta manera, las imágenes tomadas con el microscopio servirían de referencia física para el micro-CT. Para eso, el análisis 2D debería haberse llevado a cabo en el micro-CT en el mismo plano que el corte físico que se había analizado por microscopía. Sin embargo, fue imposible relacionar la altura a la que se había analizado la sección por microscopía con un plano del micro-CT debido a que la regularidad de la estructura a estudiar se tradujo en que la diferencia entre planos o rodajas trasversales en la micro-CT era inapreciable.

De las Fig.4.1 y Fig.4.2 se deduce que existen diferencias entre los escafoides porosos fabricados con la LM y la Concept. El acabado superficial parece ser mejor en el caso de los escafoides fabricados con la LM. La potencia del láser de la máquina LM es mayor que la de la Concept, lo que pudo resultar en una mejor fusión del polvo y, por tanto, en un mejor acabado superficial.

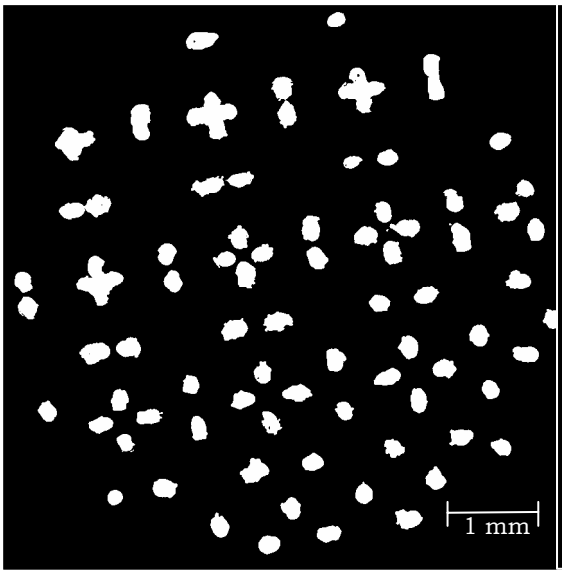

Fig.4.1. Imagen microscópica de un corte trasversal de un escafoide s0.1p1.

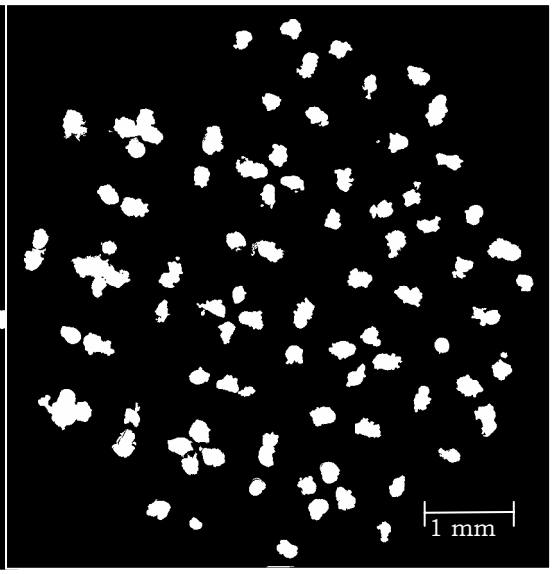

Fig.4.2. Imagen microscópica de un corte trasversal de un escafoide s0.1p1Concept.

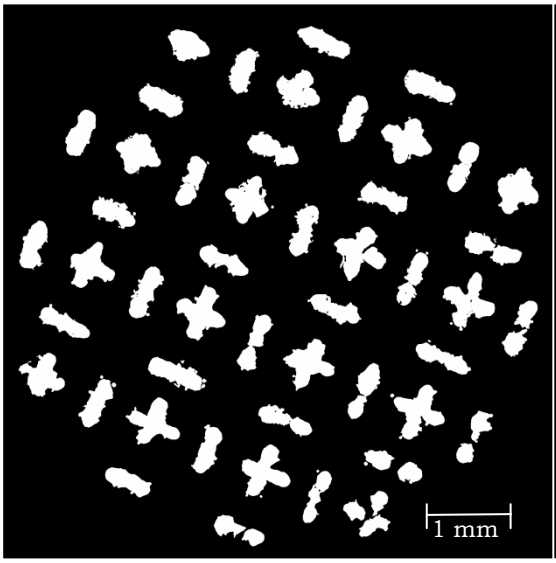

Fig.4.3. Imagen microscópica de un corte trasversal de un escafoide s0.1p0.8.

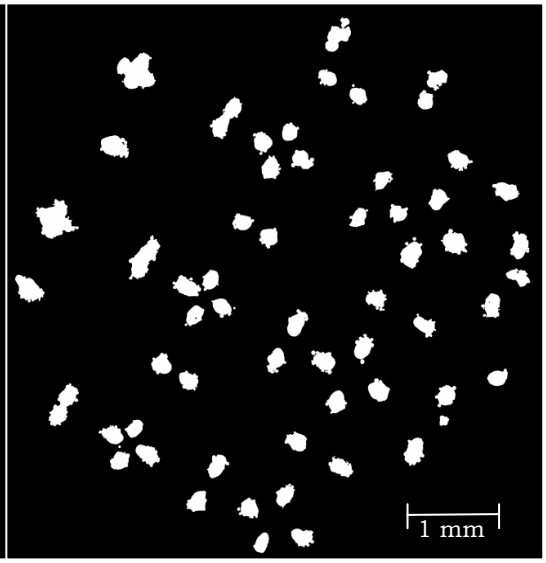

Fig.4.4. Imagen microscópica de un corte trasversal de un escafoide s0.1p1.2.

Por otro lado, las Fig.4.1, Fig.4.3 y Fig.4.4 atestiguan que la diferencia en el tamaño de poro en el diseño se traduce en una diferencia física.

4.3. Microdureza.

Los resultados de los ensayos de microdureza Vickers se presentan en la Tabla4.2. Los resultados experimentales muestran un valor de dureza significativamente superior al valor teórico del polvo del que fueron fabricados los escafoides.

Table4.2. Resultados de los ensayos de microdureza. (n=5)

	Microdureza (HV)
s0.1p0.8	401.28 ± 15.13
s0.1p1	393.92 ± 16.20
s0.1p1Concept	411.93 ± 22.91
s0.1p1.2	403.01 ± 11.23
Teórico (Recocido)	349

El método de fabricación y los tratamientos térmicos influyen mucho en la microestructura de las aleaciones de titanio (Fig.4.5). La microestructura de los escafoides fabricados por SLM se asemeja más a la del templado que a la del revenido debido a que está expuesto a un enfriamiento rápido a partir del momento en el que el láser deja de aplicarse. La presencia de martensita se constató por microscopía (Fig.4.6), lo cual puede ser la causa de esta elevada dureza.

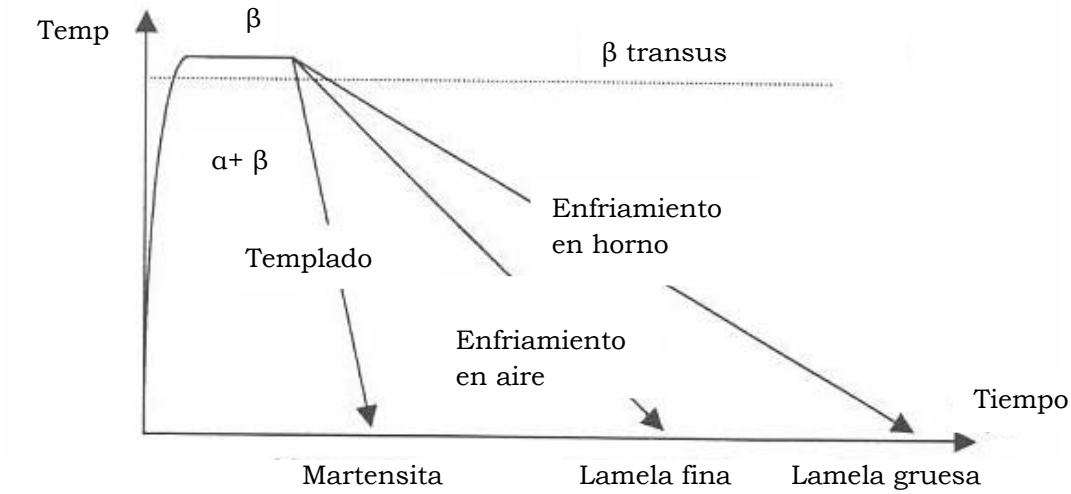

Fig.4.5. Diagrama de los distintos enfriamientos posibles y microestructuras obtenidas en el Ti6Al4V. (Schrooten [1999]).

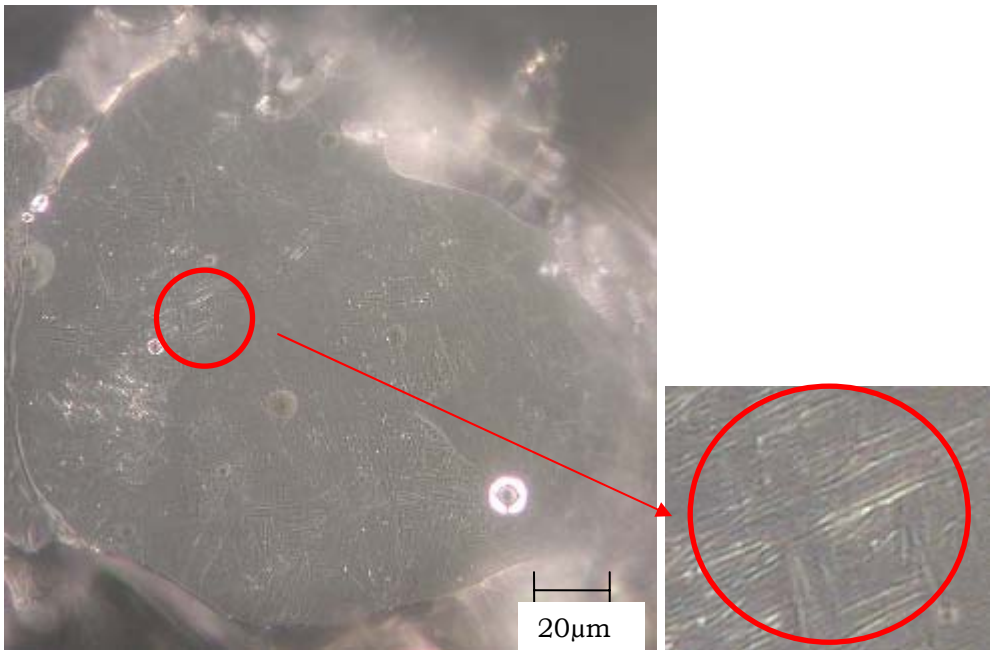

Fig.4.6. Imagen microscópica de una columna con estructura martensítica realzada con un círculo rojo.

Un test Anova para tres poblaciones reflejó que la dureza de los escafoides porosos fabricados con la LM es independiente del diseño y variables estudiados en este proyecto.

Mediante un test Anova para cuatro poblaciones se concluyó que la dureza de los escafoides porosos fabricados con la Concept es ligeramente superior a la dureza de los producidos con la LM. Este hecho podría deberse a una mayor presencia de oxígeno durante el proceso de fabricación en la Concept, que podría traducirse en la formación de óxidos de titanio, que son más duros, en la superficie del escafoide.

4.4. Ensayos mecánicos

4.4.1. Escafoides macizos

El objetivo de realizar ensayos de compresión en escafoides macizos era comparar los resultados experimentales con los teóricos y poder evaluar la ejecución de la técnica SLM en la fabricación de escafoides de Ti6Al4V. También se pretendía comparar las dos máquinas, LM y Concept, empleadas para fabricar los escafoides.

Los resultados de los ensayos se muestran en la Tabla3.3 y en la Fig.3.9 se puede ver una gráfica típica de dos muestras macizas (bulk), una de ellas fabricada con la máquina LM y la otra con la Concept.

Tabla4.3. Resultados de los ensayos de compresión en la Instron4505 de los escafoides macizos (bulk). (n=5)

	E (GPa)	**σ_{ucs} (GPa)**	**ε_{ucs} (%)**
Bulk LM	26.04 ± 0.24	1.77 ± 0.031	13.9 ± 1.3
Bulk Concept	19.07 ± 1.73	1.54 ± 0.045	20.0 ± 1.0
Teórico	113.8	-	-

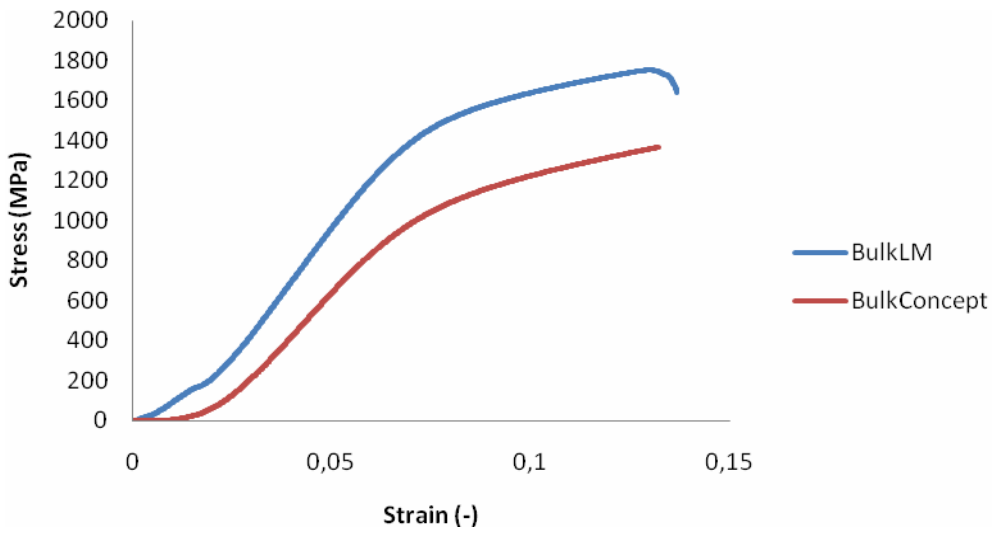

Fig.4.9. Curvas tensión deformación de escafoides macizos (bulk) medidos en la Instron4505.

La gran diferencia entre los valores teóricos esperados y los experimentales podría deberse a las siguientes dos razones. El valor teórico corresponde al Titanio Ti6Al4V (Grado 5), Recocido, el polvo a partir del cual se fabricaron los escafoides. Sin embargo, ha de tenerse en cuenta que la aleación no estará recocida, sino templada tras el proceso de fabricación por SLM debido al enfriamiento rápido tras dejar de aplicarse el haz láser. Además, el criterio escogido para determinar el valor teórico del módulo E es desconocido.

Los escafoides fabricados con la máquina LM muestran unas propiedades mecánicas superiores a aquellos fabricados con la Concept, a pesar de que en ambos casos se partió del mismo diseño y las dos máquinas emplean la misma técnica de fabricación. No obstante, la potencia del láser de la LM es mayor que la de la Concept, lo que podría traducirse en una mejor unión entre partículas y, por ende, en unas mejores propiedades mecánicas.

4.4.2. Escafoides porosos

4.4.2.1. Ensayos de compresión

Los resultados de los ensayos de compresión en la Instron y en la máquina de ensayo in situ (in situ loading stage) se muestran en las Tabla4.4, Tabla4.5 y Tabla4.6.

Tabla4.4. Resultados del módulo de Young E de los ensayos continuos de compresión de los escafoides porosos. (n=5)

	Módulo de Young (MPa)		
	Instron	**In Situ Loading Stage**	**p-valor**
s0.1p0.8	389.68 ± 22.64	369.76 ± 29.83	0.32
s0.1p1	225.56 ± 20.46	237.74 ± 16.40	0.10
s0.1p1Concept	102.09 ± 8.948	101.17 ± 9.08	0.89
s0.1p1.2	79.93 ± 5.15	81.89 ± 4.92	0.53

Tabla4.5. Resultados de tensión de rotura de los ensayos continuos de compresión de los escafoides porosos. (n=5)

	Tensión de rotura (MPa)		
	Instron	**In Situ Loading Stage**	**p-valor**
s0.1p0.8	15.70 ± 0.30	14.81 ± 1.41	0.17
s0.1p1	8.05 ± 0.28	8.04 ± 0.22	0.87
s0.1p1Concept	3.46 ± 0.07	3.44 ± 0.09	0.54
s0.1p1.2	3.97 ± 0.09	3.87 ± 0.22	0.44

Tabla4.6. Resultados de deformación de rotura de los ensayos continuos de compresión de los escafoides porosos. (n=5)

	Deformación de rotura (%)		
	Instron	**In Situ Loading Stage**	**p-valor**
s0.1p0.8	9.2 ± 0.5	0.073 ± 0.4	0.001
s0.1p1	7.3 ± 0.2	7.2 ± 0.4	0.53
s0.1p1Concept	4.7 ± 0.3	4.7 ± 0.3	0.78
s0.1p1.2	9.0 ± 0.6	8.2 ± 0.2	0.44

La comparación de los resultados de la Instron y la máquina de ensayos in situ (in situ loading stage) muestra un p-valor mayor de 0.05 para todos los casos, excepto el de la deformación de rotura en el caso de los escafoides s0.1p0.8. Debido a esto, se dio por validada y calibrada máquina de ensayos in situ, por no existir diferencias significativas entre ensayar las muestras en esta máquina o en la Instron4505. Esto significa que en futuros estudios sería suficiente con realizar los ensayos de compresión en la máquina de ensayo in situ, que es en la que posteriormente se llevaría a cabo el ensayo de compresión escalonado para permitir la toma de imágenes vía micro-CT.

En la Tabla4.7 y Fig.4.10 se observa que existen diferencias en las propiedades mecánicas de los escafoides según se hayan fabricado con la máquina LM o la Concept.

Tabla4.7. Resultados de los ensayos de compresión realizados en la máquina de ensayo in situ para s0.1p1 y s0.1p1Concept. (n=5)

	E (MPa)	**σ_R (MPa)**	**ε_R (%)**
s0.1p1	237.74 ± 16.40	8.04 ± 0.22	7.2 ± 0.4
s0.1p1Concept	101.17 ± 9.08	3.44 ± 0.09	4.7 ± 0.3

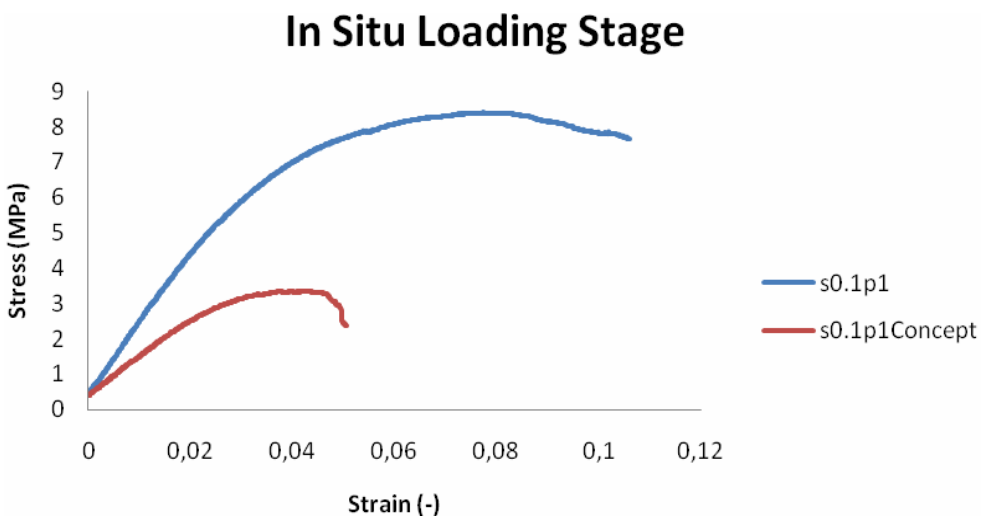

Fig.4.10. Curva tensión deformación típica obtenida en la máquina de ensayo in situ para muestras s0.1p1 y s0.1p1Concept.

El módulo E y la tensión de rotura de los escafoides porosos fabricados con la LM casi doblan el valor de aquellos fabricados con la Concept y la deformación de rotura es también ligeramente superior. Se concluyó que a pesar de emplear la misma técnica (SLM), los escafoides fabricados con la máquina LM presentan mejores propiedades mecánicas que aquellos producidos con la Concept, debido seguramente a que la potencia del láser es mayor en la LM.

En cuanto a los escafoides porosos fabricados con la LM, los resultados de los ensayos de compresión en la máquina de ensayo in situ se muestran en la Tabla4.8. La Fig.4.11 muestra una curva tensión deformación típica de cada diseño.

Tabla4.8. Resultados de los ensayos de compresión llevados a cabo en la máquina de ensayo in situ para muestras s0.1p0.8, s0.1p1 y s0.1p1.2. (n=5)

	E (MPa)	**σ_{ucs} (MPa)**	**ε_{ucs} (%)**
s0.1p0.8	369.76 ± 29.83	14.81 ± 1.41	7.3 ± 0.4
s0.1p1	237.74 ± 16.40	8.04 ± 0.22	7.2 ± 0.4
s0.1p1.2	81.89 ± 4.92	3.87 ± 0.22	8.2 ± 0.2

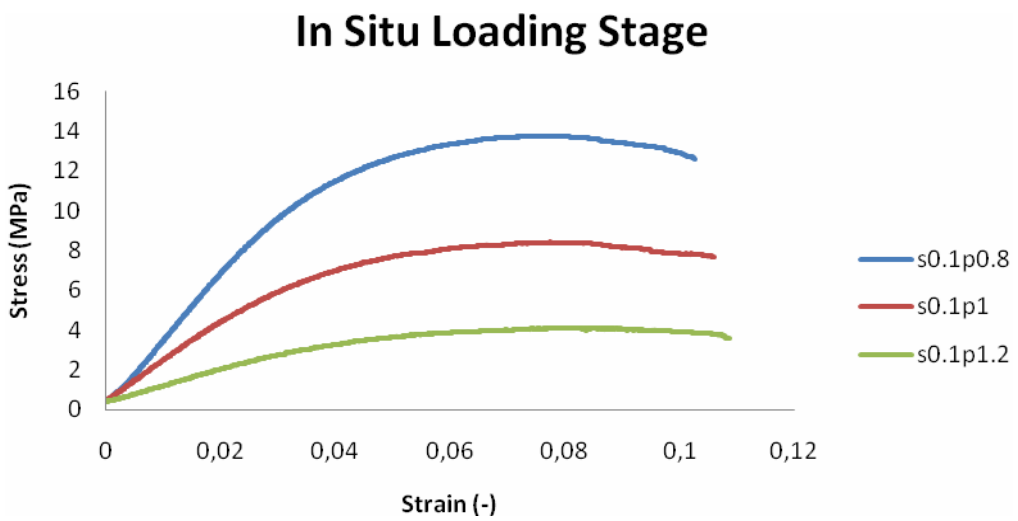

Fig.4.11. Curvas típicas tensión deformación para una muestra de cada diseño s0.1p0.8, s0.1p1 y s0.1p1.2.

De la Tabla4.8 se puede deducir que la variación o desviación típica de las propiedades mecánicas de los escafoides de un mismo lote de igual diseño es siempre inferior al 10%, lo cual indica que la técnica de fabricación es robusta.

Además, los resultados indican que a mayor tamaño de poro, menores son las propiedades mecánicas. Recordar que el tamaño de poro está representado por el número que aparece tras la p en el nombre empleado para identificar los escafoides. Gibson y Ashby [Ref.] describen la relación entre densidad específica y propiedades mecánicas como el módulo E o la tensión de rotura (σ_R) para estructuras de celda abierta (Fig.4.12(a)) y estructuras nido de abeja (Fig.4.12(b)). La celda unidad de los escafoides porosos de Ti6Al4V para este proyecto se muestra en la (Fig.3.11(c)).

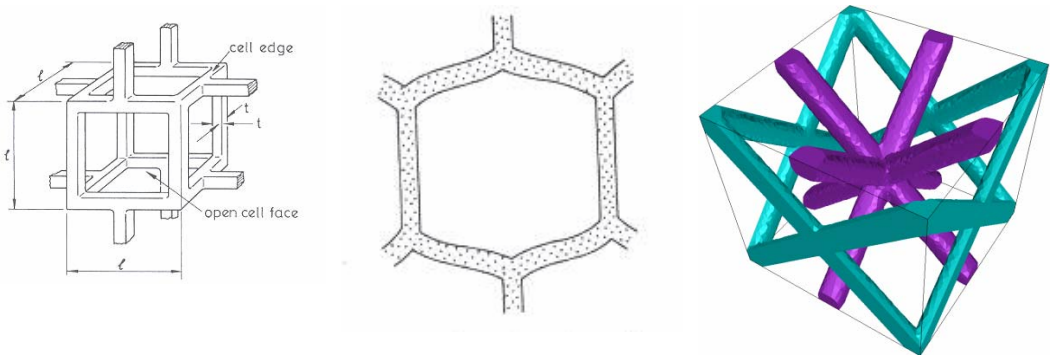

(a) ***(b)*** ***(c)***

Fig.4.12. *(a)* celda abierta, *(b)* nido de abeja, *(c)* celda unidad de un escafoide poroso de Ti6Al4V.

Para estructuras tipo celda abierta, la ecuación (4.1) relaciona la densidad específica con el modulo E, mientras que la ecuación (4.2) relaciona la densidad específica con la tensión de rotura.

$$\frac{E}{E_s} = \left(\frac{\rho}{\rho_s} \right)^2 \qquad \text{ec. (4.1)}$$

donde E es el módulo de Young de la estructura de celda abierta, ρ es la densidad de la estructura de celda abierta y E_s y ρ_s son, respectivamente, el módulo de Young y la densidad del material macizo del que está hecho el material poroso.

$$\frac{\sigma_R}{\sigma_y} = C\left(\frac{\rho}{\rho_s} \right)^{2/3} \qquad \text{ec. (4.2)}$$

donde σ_R es la tensión de rotura de la estructura de celda abierta, σ_y es el límite elástico del material macizo del que está hecho el material poroso, y C es una constante.

Para estructuras nido de abeja, la ecucación (4.3) relaciona la densidad específica con el modulo E, mientras que la ecuación (4.4) relaciona la densidad específica con la tensión de rotura.

$$\frac{E}{E_s} = 2.3\left(\frac{\rho}{\rho_s} \right)^3 \qquad \text{ec. (4.3)}$$

$$\frac{\sigma_R}{\sigma_y} = \frac{2}{3}\left(\frac{\rho}{\rho_s} \right)^2 \qquad \text{ec. (4.4)}$$

Las ecuaciones en el caso de la celda unidad de los escafoides porosos de Ti6Al4V quedan de la siguiente manera (puede verse cómo se obtuvieron en el proyecto completo en inglés):

$$\frac{E}{E_s} = 0.85\left(\frac{\rho}{\rho_s} \right)^{2.38} \text{(MPa)} \qquad \text{ec.(4.5)}$$

$$\frac{\sigma_R}{\sigma_y} = 0.39\left(\frac{\rho}{\rho_s} \right)^{2.04} \text{(MPa)} \qquad \text{ec.(4.6)}$$

Si se comparan las ecuaciones (4.1), (4.3) y (4.5) se observa que el valor del exponente de la ecuación (4.5) está entre los valores de los exponentes de las otras dos ecuaciones. Esto quiere decir que, en lo que a módulo de Young se refiere, el comportamiento a compresión de los escafoides porosos de celda unidad la de la Fig.4.12(c) de Ti6Al4V fabricados vía SLM con la máquina LM se encuentra entre aquel de las estructuras de celda abierta y nido de abeja.

Si se comparan las ecuaciones (4.2), (4.4) y (4.6) se observa que el valor del exponente de la ecuación (4.6) es muy cercano al valor del exponente de la ecuación (4.4). Esto quiere decir que, en lo que a tensión de rotura se refiere, el comportamiento a compresión de los escafoides porosos de celda unidad la de la

Fig.4.12(c) de Ti6Al4V fabricados vía SLM con la máquina LM es muy parecido a aquel de las estructuras nido de abeja.

Se comprobó si los escafoides porosos de Ti6Al4V fabricados con la Concept cumplían las ecuaciones (4.5) y (4.6) y el resultado fue negativo. Esto quiere decir que las ecuaciones no dependen de la técnica de fabricación sino de la máquina con la que se fabriquen.

4.4.2.2. Ensayos cíclicos

Se ha decidido omitir el apartado correspondiente a los ensayos cíclicos en el resumen debido a que, por problemas técnicos, no se pudo extraer información relevante.

4.5. Micro-CT combinado con ensayos de compresión

Se realizaron ensayos de compresión escalonados combinados con la toma de imágenes vía micro-CT en los escafoides porosos fabricados con la máquina LM. Los fabricados con la Concept se descartaron debido a que sus propiedades mecánicas son más bajas. Los puntos de parada en los que se llevaría a cabo la toma de imágenes mediante micro-CT fueron escogidos basándose en los datos de los ensayos continuos de compresión.

4.5.1. Compresión escalonada

La Fig.4.13 muestra curvas típicas de tensión deformación resultantes de ensayos de compresión escalonados para una muestra aleatoria de cada lote s0.1p0.8, s0.1p1 y s0.1p1.2.

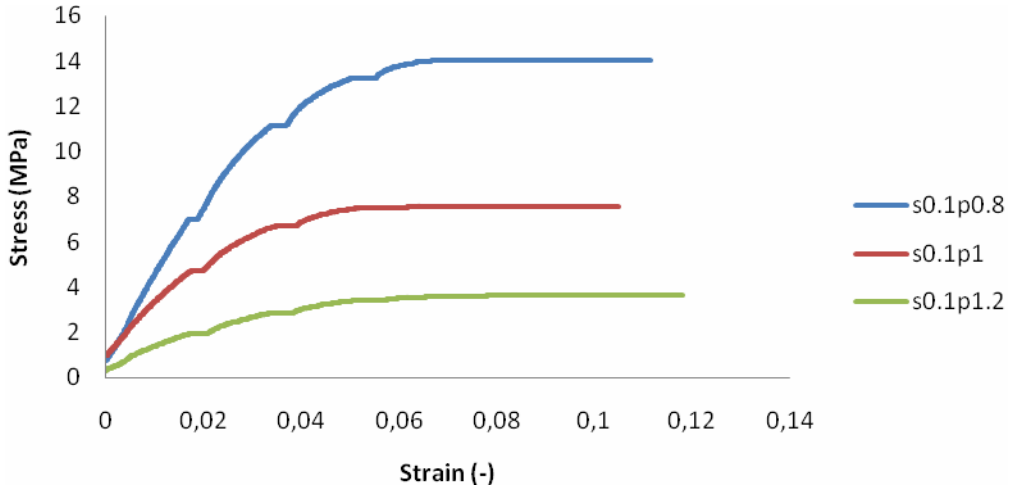

Fig.4.13. Curvas tension deformación de muestras s0.1p0.8, s0.1p1 y s0.1p1.2, resultantes de ensayos de compresión escalonados, en las que los puntos correspondientes al tiempo de escaneo y la relajación han sido suprimidos.

Las propiedades mecánicas derivadas del ensayo de compresión escalonado se resumen en las Tabla4.9, Tabla4.10 y Tabla4.11 junto con aquellas correspondientes a los ensayos continuos y los p-valores resultantes de la comparación de ambos.

Tabla4.9. Resultados para el módulo de Young de los ensayos de compresión continuos y escalonados llevados a cabo con la máquina de ensayos in situ. (n=5)

	Módulo de Young (MPa)		
	Continuo	**Escalonado**	**p-valor**
s0.1p0.8	369.76 ± 29.83	481.77 ± 28.12	0.014
s0.1p1	237.74 ± 16.40	267.06 ± 28.81	0.094
s0.1p1.2	81.89 ± 4.92	108.17 ± 8.22	0.007

Tabla4.10. Resultados para la tensión de rotura de los ensayos de compresión continuos y escalonados llevados a cabo con la máquina de ensayos in situ. (n=5)

	Tensión de rotura (MPa)		
	Continuo	**Escalonado**	**p-valor**
s0.1p0.8	14.81 ± 1.41	14.49 ± 0.95	0.36
s0.1p1	8.04 ± 0.22	7.78 ± 0.18	0.071
s0.1p1.2	3.87 ± 0.22	3.69 ± 0.13	0.257

Tabla4.11. Resultados para la deformación de rotura de los ensayos de compresión continuos y escalonados llevados a cabo con la máquina de ensayos in situ. (n=5)

	Deformación de rotura (%)		
	Continuo	**Escalonado**	**p-valor**
s0.1p0.8	7.27 ± 0.35	7.19 ± 0.65	0.36
s0.1p1	7.16 ± 0.39	6.54 ± 0.08	0.018
s0.1p1.2	8.24 ± 0.17	7.71 ± 0.57	0.06

Los valores referidos a la tensión de rotura y deformación de rotura no presentan diferencias significativas en los ensayos continuos y escalonados, excepto en las muestras de diseño s0.1p1, para el que el p-valor es menor de 0.05. No obstante, los resultados difieren para el módulo E en función del ensayo. Siendo la tensión de rotura y la deformación de rotura iguales, el módulo de E debería también ser el mismo según la ley de Hooke (ec.(3.8)).

$$\sigma_R = E \cdot \varepsilon_R \qquad \text{ec. (4.8)}$$

Esto indica que fue una decisión acertada la de no calcular el módulo de Young a partir de la ley de Hooke, pues el material no tiene un comportamiento elástico lineal. Sin embargo, el procedimiento escogido para el cálculo del módulo E induce errores en el caso de los ensayos de compresión escalonados.

Por lo tanto, no podría considerarse que el comportamiento mecánico de los escafoides porosos de Ti6Al4V fabricados vía SLM es igual en carga continua y carga escalonada.

4.5.2. Análisis de las imágenes de micro-CT en el estado de precarga.

Se realizó un estudio de los parámetros morfológicos de los escafoides porosos en estado de precarga con el objetivo de ver cuáles son las diferencias morfológicas entre escafoides de igual diseño, salvo por el tamaño de poro. La Fig.(4.14) muestra una radiografía de un escafoide de cada diseño.

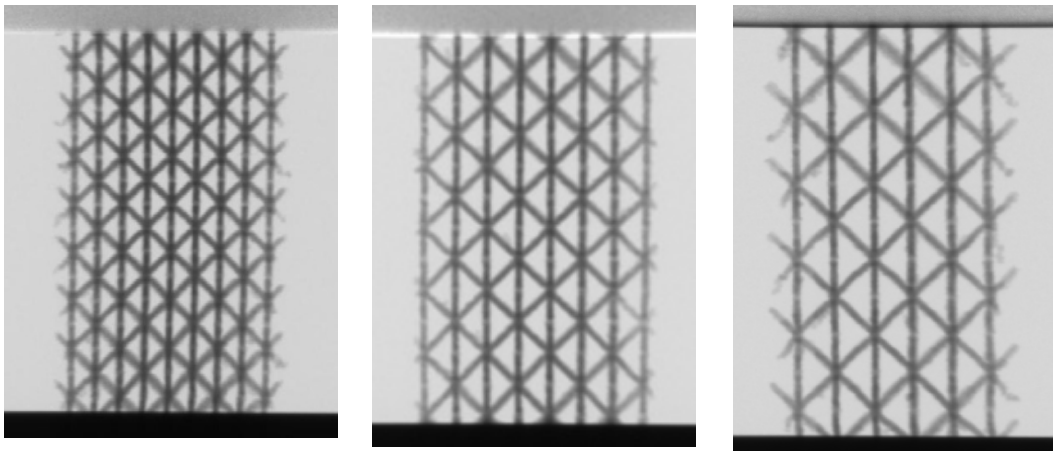

(a) s0.1p0.8 *(b)* s0.1p1 *(c)* s0.1p1.2

Fig.4.14. Radiografía en estado de precarga de muestras de diseño *(a)* s0.1p0.8. *(b)* s0.1p1 y *(c)* s0.1p1.2.

La Tabla(4.12) resume algunos de los parámetros morfológicos que se pueden obtener vía micro-CT.

Tabla4.12. Parámetros morfológicos obtenidos vía micro-CT.

Porosidad (%)	Volumen ocupado por los poros dividido por el volumen total del escafoide.
Superficie específica (1/mm)	Área de superficie dividida por el volumen total del escafoide.
Anisotropía preferencial	Medida de la presencia o ausencia de un alineamiento de la estructura a lo largo de un eje direccional particular. Está representado por un número entre 0 y 1. Cero significa que la estructura es isotrópica.
Diámetro de columna medio (µm)	Se determina como el grosor local medio en cada voxel que representa materia sólida (Hildebrand and Ruegsegger [1997]).
Diámetro de poro medio (µm)	Se determina como el grosor local medio en cada voxel que representa materia sólida, binarizando la imagen al contrario de como se hace para calcular el diámetro de columna.
Interconectividad (%)	Porcentaje de poros del escafoide al que se puede acceder desde el exterior. Se calcula como: Interconectividad (%) = 100 – Porosidad cerrada (%)

Los valores de porosidad obtenidos vía micro-CT se presentan en la Tabla(4.13). La porosidad dada por el micro-CT fue ligeramente inferior a la calculada por Arquímedes. Este resultado era de esperar debido al efecto parcial de volumen tal y como lo reflejan De Man et al. [Ref.] [Ref.] y la resolución limitada, que son inherentes a las imágenes tomadas vía micro-CT. No obstante, los resultados reflejan que a mayor tamaño de poro, mayor es la porosidad de los escafoides.

Tabla4.13. Resultados de la porosidad obtenida por Arquímedes y micro-CT para s0.1p0.8, s0.1p1 y s0.1p1.2. (n=5)

	Porosidad (%)	
	Arquímedes	**Micro-CT**
s0.1p0.8	85.28 ± 0.49	80.52 ± 1.08
s0.1p1	88.13 ± 0.10	85.43 ± 0.33
s0.1p1.2	92.24 ± 0.15	90.71 ± 1.14

La Tabla(4.14) muestra los parámetros morfológicos correspondientes a los escafoides porosos en estado de precarga. La baja variabilidad de los datos para muestras de igual diseño es prueba de la alta repetibilidad y robustez de la máquina LM y, por tanto, de la técnica de fabricación (SLM).

Tabla4.14. Parámetros morfológicos obtenidos vía micro-CT en estado de precarga. (n=5)

	s0.1p0.8	**s0.1p1**	**s0.1p1.2**
Porosidad (%)	80.52 ± 1.08	85.43 ± 0.33	90.71 ± 1.14
Superficie específica (1/mm)	21.94 ± 0.65	21.59 ± 0.63	22.75 ± 0.67
Anisotropía	0.59 ± 0.02	0.61 ± 0.02	0.68 ± 0.10
Diámetro de poro medio (μm)	480 ± 8	601 ± 4	776 ± 12
Diámetro de columna medio (μm)	187 ± 5	601 ± 4	181 ± 5
Interconectividad (%)	100	100	100

La superficie específica, la anisotropía y el grado de interconectividad son parámetros morfológicos desde el punto de vista biomédico, ya que afectan directamente al crecimiento de las células. Se observa que dichos parámetros apenas varían de un diseño a otro en el estado de precarga. No obstante, son parámetros muy a tener en cuenta puesto que su evolución bajo diferentes estados de compresión podría diferir.

Los parámetros que más interés suscitan desde el punto de vista de la ingeniería son la interconectividad, el diámetro de poro y el diámetro de columna.

El hecho de que la interconectividad fuese del 100%, tal y como se había diseñado, vuelve a dar una idea de cuán robusta es la técnica de fabricación para el caso de los escafoides porosos de Ti6Al4V estudiados.

Las Fig. (4.15), Fig.(4.16) y Fig.(4.17) muestran las distribución del diámetro de poro para las cinco muestras de escafoides de los diferentes diseños.

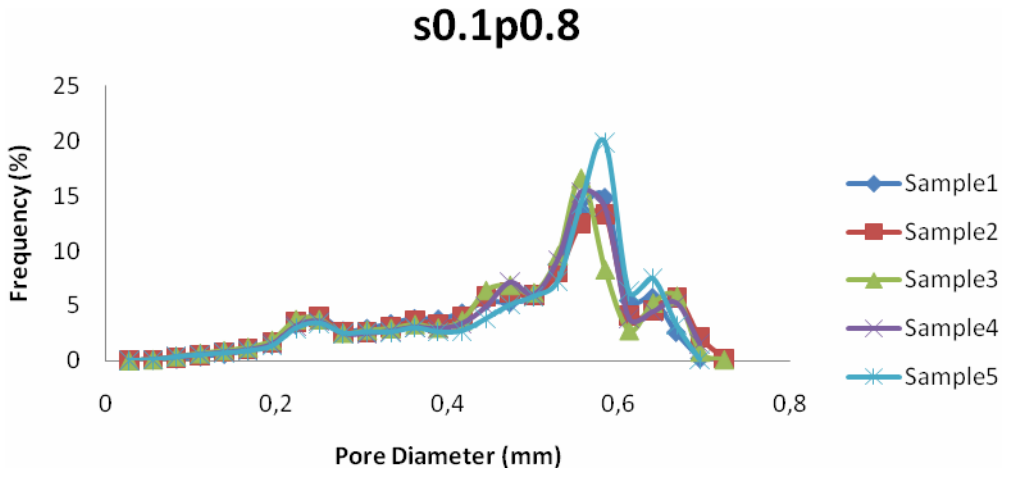

Fig.4.15. Distribución del diámetro de poro para las muestras s0.1p0.8.

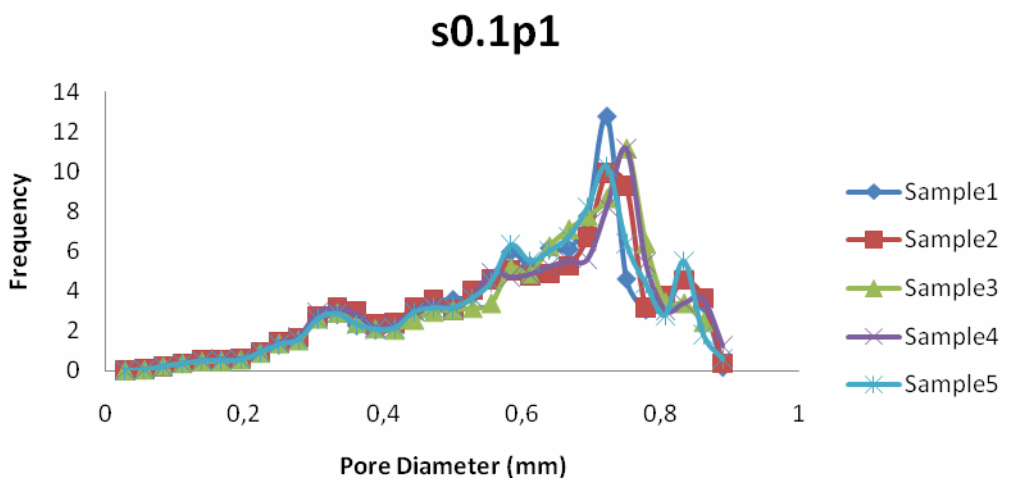

Fig.4.16. Distribución del diámetro de poro para las muestras s0.1p1.

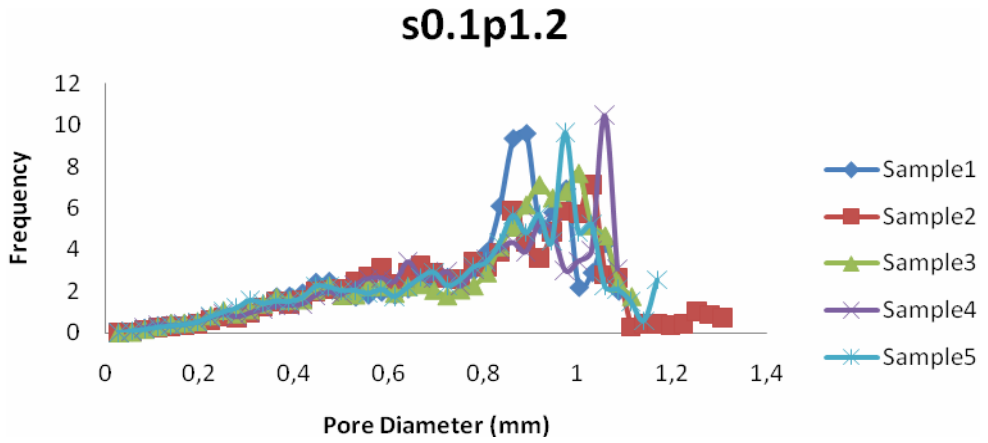

Fig.4.17. Distribución del diámetro de poro para las muestras s0.1p1.2.

A la vista de los gráficos puede apreciarse que la distribución del diámetro de poro no es constante en la diferentes muestras de diseño s0.1p1.2. En este caso la muestra solo albergaba en torno a cinco celdas unidad, pues el diámetro de los escafoides era de 6 mm. Además, se escogía, para el análisis por micro-CT, un volumen de interés omitiendo las esquinas, resultando en el caso de los escafoides s0.1p1.2 en muy pocas celdas unidad de las que obtener información cuantitativa fiable. Se concluyó, por tanto, que para futuros trabajos sería recomendable emplear muestras de mayor diámetro para el diseño s0.1p1.2.

La Fig.(4.18(a)) muestra una celda unidad de un escafoide poroso de Ti6Al4V, mientras que la Fig.(4.18(b)) muestra una simplificación de la celda unidad en la que se ha indicado, mediante una flecha, lo que se definió como tamaño de poro al hacer el diseño en CAD.

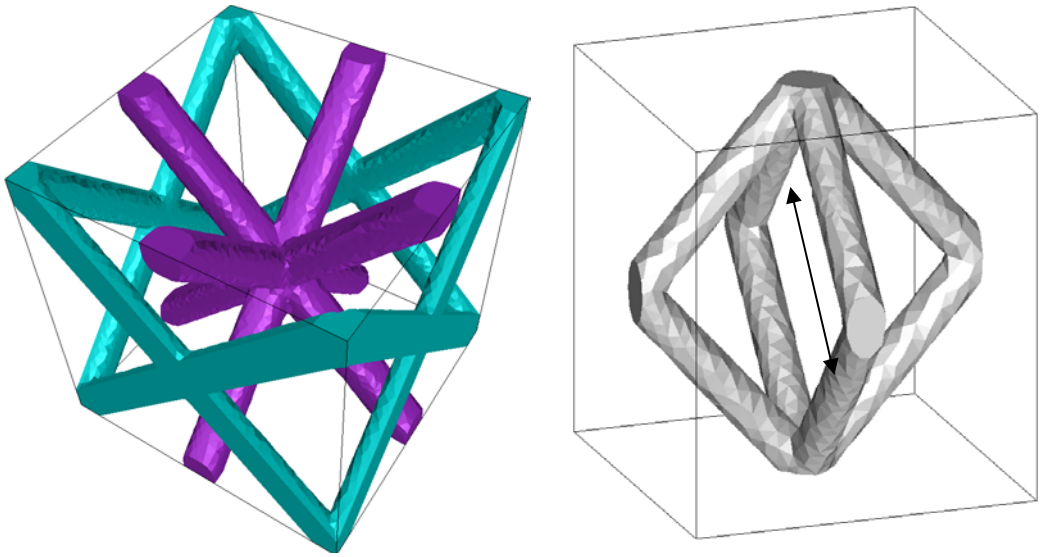

(a) *(b)*

Fig.4.18. *(a)* celda unidad del escafoide. *(b)* celda unidad simplificada del escafoide en la que lo que se definió como el tamaño de poro al diseñar la pieza en CAD está definido con una flecha negra.

Hasta el momento no ha sido posible establecer una correspondencia entre los picos de las gráficas y los poros físicos a los que corresponden. Se trata de trabajo que se está desarrollando en la actualidad.

El diámetro de columna se diseño para ser de 0.1 mm en todos los escafoides, independiente del diámetro de poro. Debería, por tanto, ser el mismo independientemente del lote al que pertenezcan las muestras. En la Tabla(4.15) y la Fig.(4.19) puede observarse que así ocurre. Este hecho vuelve a dar fe de la repetibilidad de la técnica de producción. Sin embargo, el diámetro real de las columnas era casi el doble de lo que se había diseñado que fuese; lo cual fue atribuido a que el valor de diseño estaba muy cerca de los límites físicos de producción.

Tabla4.15. Diámetro de columna medio para s0.1p0.8, s0.1p1 y s0.1p1.2 en estado de precarga. (n=5)

	Diámetro medio de columna (mm)
s0.1p0.8	0.179 ± 0.006
s0.1p1	0.188 ± 0.004
s0.1p1.2	0.180 ± 0.005
Diseño	0.100

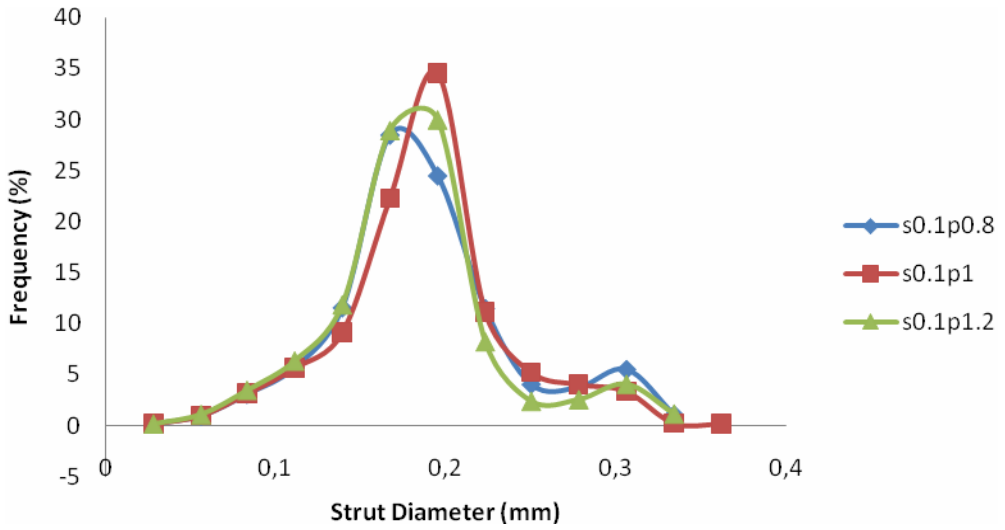

Fig.4.19. Distribución del diámetro medio de columna para s0.1p0.8, s0.1p1 y s0.1p1.2.

En la gráfica se diferencian dos picos. El más alto se corresponde con el diámetro de columna real (Fig.(4.20(a)), mientras que el más pequeño, a su derecha, se corresponde con el diámetro de nodo, punto en el que coinciden cuatro columnas (Fig.4.20(b)).

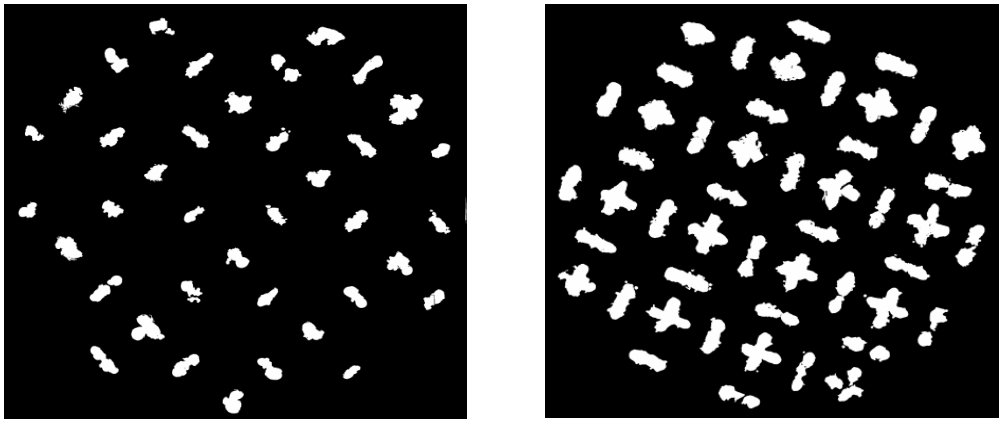

(a) *(b)*

Fig.4.20.*(a)* sección de escafoide en la que pueden apreciarse las columnas *(b)* sección de escafoide en la que pueden apreciarse los nodos, cada uno rodeado de cuatro columnas.

4.5.3. Carga escalonada combinada con toma de imágenes vía micro-CT.

Los ensayos escalonados de compresión, combinados con la toma de imágenes vía micro-CT, permitieron estudiar la evolución de los parámetros morfológicos bajo diferentes cargas de compresión o, lo que es lo mismo, para diferentes grados de deformación. Debido a la falta de tiempo y valiéndose de la baja variabilidad en los parámetros morfológicos de las muestras de igual diseño, solo se analizó la información correspondiente a una muestra por diseño.

Tratándose de un resumen, se comentarán únicamente los resultados de las variables de mayor interés desde el punto de vista de la ingeniería, es decir, la porosidad y el diámetro de columna.

En la Fig.(4.21.) se muestra la variación de la porosidad, bajo los diferentes estados de carga para una muestra de cada diseño. Se observó que la porosidad aumentaba en todos los casos hasta que se alcanzaba una deformación del 5%, que se corresponde con la tensión inmediatamente anterior a la de rotura. La porosidad crecía debido al "bulking out" de la estructura, lo que podría indicar "buckling" de las columnas (Fig.(4.22.)). A partir de la deformación de 5%, sin embargo, el valor de la porosidad permanecía constante o bien decrecía, debido seguramente al acercamiento de las columnas que se traduce en una disminución del tamaño de poro.

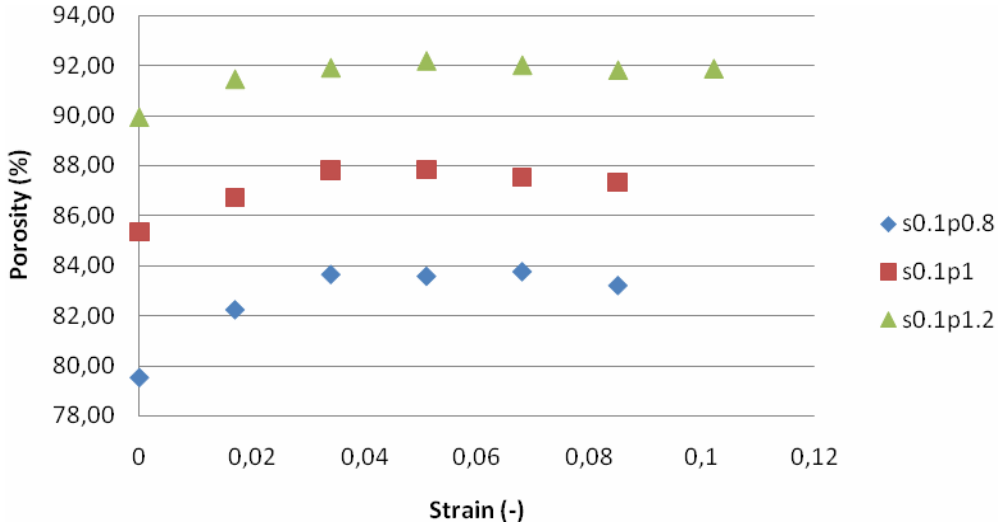

Fig.4.21. Porosidad frente a deformación para una muestra por diseño.

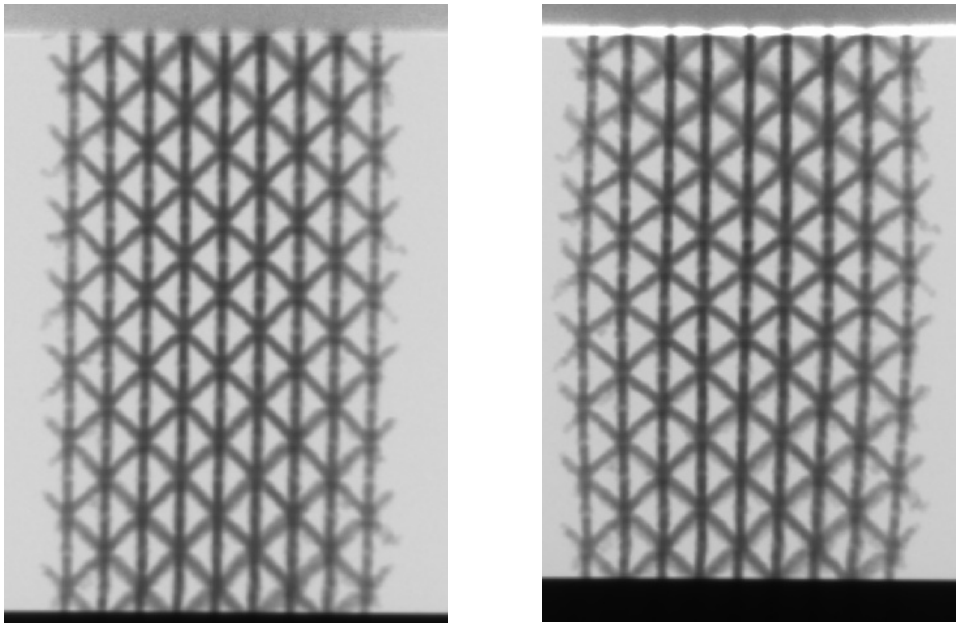

(a) *(b)*

Fig.4.22. *(a)* escafoide en estado de precarga (deformación 0%) *(b)* escafoide en deformación 5%.

En lo que a la variación del diámetro de columna se refiere se analizó una sola muestra, puesto que la variabilidad del diámetro de columna no solo era baja en las muestras de igual diseño, sin que también lo era para los distintos diseños. En la Fig.(4.23) se muestra la variación del diámetro de columna bajo los diferentes escalones de compresión. Se observó que éste permanecía invariable, es decir, el diámetro de columna no cambiaba al someter al escafoide a una compresión escalonada.

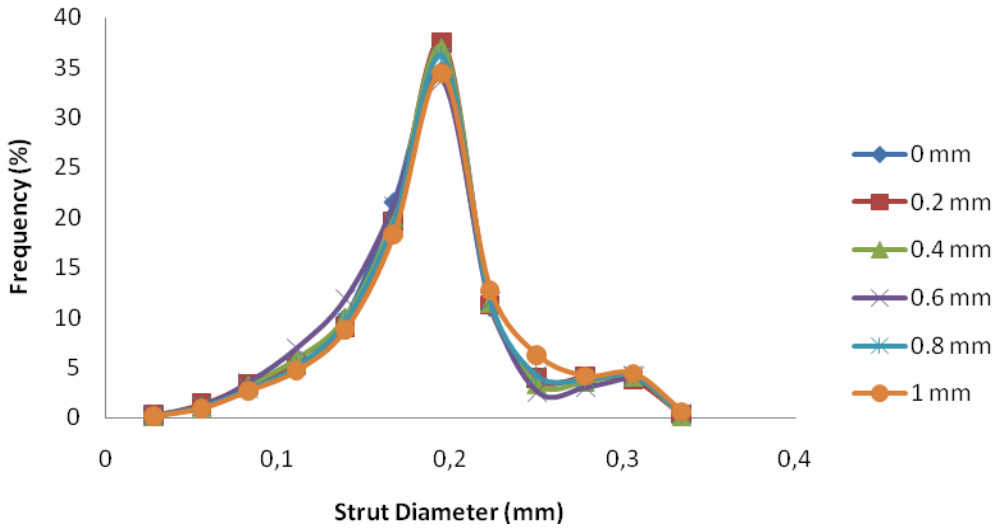

Fig.4.23. Distribución del diámetro de columna de una muestra bajo distintos estados de deformación.

4.5.3.1. Mecanismos de fractura.

Las imágenes radiográficas de los escafoides porosos bajo sucesivos estados de carga podrían servir para definir o comprobar los mecanismos de fractura.

Las radiografías parecían mostrar algunas diferencias en el mecanismos de fractura dependiendo del diseño, es decir, dependiendo del tamaño de poro (Fig.(4.23)). A mayor tamaño de poro, “shear banding” era menos evidente.

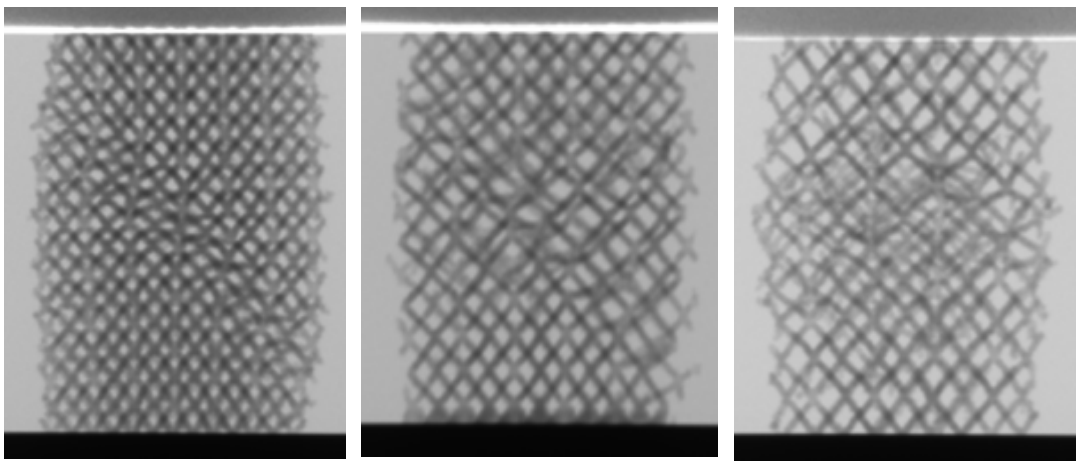

(a) *(b)* *(c)*

Fig.4.23. ***(a)*** **s0.1p0.8** ***(b)*** **s0.1p1** ***(c)*** **s0.1p1.2**

Además, las partes superior e inferior del escafoide no registraron cambio alguno, siendo la parte central la única que se deformó. El "buckling" de las columnas, marcado con círculos rojos, puede apreciarse en la Fig.(3.24.)

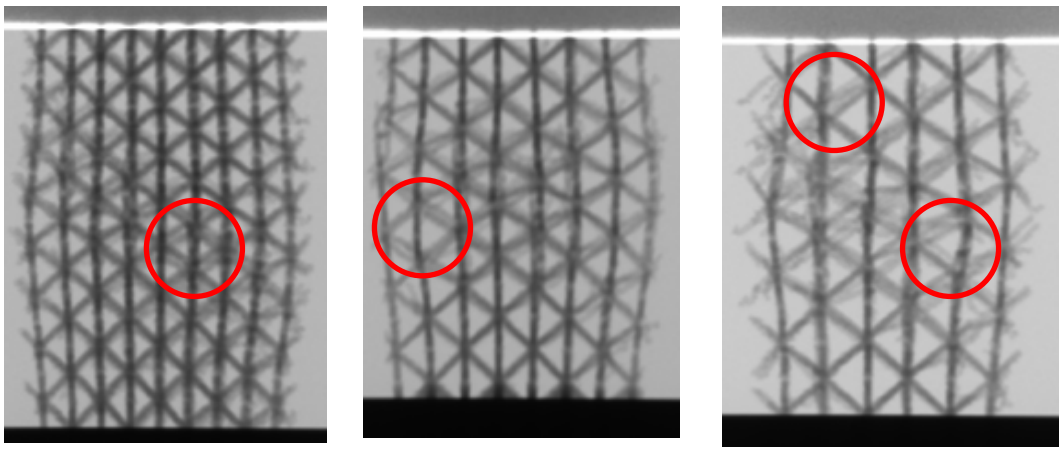

(a) *(b)* *(c)*

Fig.4.24. ***(a)*** **s0.1p0.8** ***(b)*** **s0.1p1** ***(c)*** **s0.1p1.2**

La falta de tiempo imposibilitó un análisis más detallado de los datos obtenidos vía micro-CT. No obstante, se concluyó que el estudio de imágenes radiográficas correspondientes a distintos estados de carga podría conducir a la comprensión y caracterización de los mecanismos de fractura de los escafoides porosos de Ti6Al4V fabricados vía SLM.

5. Conclusiones

Las técnicas RP son muy adecuadas para la fabricación de escafoides para implantación ósea, pues permiten un alto control de los parámetros morfológicos, que juegan un papel importante en el crecimiento de las células. En este proyecto se estudiaron escafoides porosos para implantación ósea de Ti6Al4V producidos por SLM, que es una técnica de RP, con dos máquinas diferentes, LM y Concept.

La ejecución de SLM, la técnica de RP, fue evaluada mediante la caracterización mecánica de estructuras macizas de Ti6Al4V. Las propiedades mecánicas de las estructuras macizas resultaron ser significativamente inferiores a las teóricas, lo cual invitó a pensar que, además de una microporosidad del 0.5%, el SLM podría no traducirse en una unión perfecta entre partículas. Sería muy interesante tener este hecho en cuenta en el modelo de Elementos Finitos, ya que aporta un conocimiento más profundo de las propiedades del Ti6Al4V procesados vía SLM.

La caracterización mecánica y morfológica de los escafoides porosos para implantación ósea de Ti6Al4V fabricados vía SLM con la máquina LM se llevó a cabo mediante diversos métodos, entre los que cabe destacar el ensayo de compresión escalonado combinado con la toma de imágenes vía micro-CT, con el

fin último de encontrar una correlación entre las propiedades morfológicas y mecánicas de los escafoides.

En este proyecto se instaló una máquina de ensayo nueva dentro de la micro-CT para evitar el traslado de las muestras. La nueva máquina de ensayo se validó demostrando que los resultados obtenidos no diferían significativamente al compararlos con aquellos obtenidos de los ensayos en una máquina convencional (Instron4505). De este modo, en trabajos futuros podría emplearse únicamente la nueva máquina de ensayo para llevar a cabo la caracterización mecánica de escafoides porosos para implantación ósea de Ti6Al4V fabricados por SLM.

También se caracterizaron mecánicamente escafoides porosos para implantación ósea de Ti6Al4V fabricados por SLM con la máquina Concept. Los resultados mostraron que con esta última las propiedades mecánicas eran inferiores y la superficie más rugosa que la de los escafoides producidos con la máquina LM. La potencia del láser de la LM es mayor que la de la Concept, lo que se tradujo en mejores propiedades mecánicas y mejor acabado superficial debido, probablemente, a una mayor unión entre partículas. Es por ello que se descartó realizar una investigación más profunda, mediante ensayos de compresión escalonados combinados con la toma de imágenes vía micro-CT, en los escafoides fabricados con la Concept.

Los ensayos de microdureza revelaron que la dureza de los escafoides fabricados con la LM era independiente del tamaño de poro. El valor experimental excedió al teórico debido a la presencia de una fase martensítica en la microestructura.

Los ensayos cíclicos no aportaron información fiable debido a problemas técnicos. Sin embargo, para futuros trabajos, sería recomendable utilizar una célula de carga menor que la utilizada en este proyecto (30 kN) y alcanzar el límite elástico en cada ciclo.

Los resultados de los ensayos de compresión continuos y la medida de densidad por Arquímedes permitieron establecer una correlación entre la porosidad, el módulo E y la tensión de rotura para los escafoides fabricados en la LM. Se verificó que los escafoides producidos con la Concept no cumplían estas ecuaciones, lo que quiere decir que las ecuaciones no dependen de la técnica de fabricación, sino de la máquina empleada. Estas ecuaciones permitirían predecir el módulo E (eq.4.1.)y la tensión de rotura (eq.4.2.) de escafoides porosos de Ti6Al4V de igual celda unidad que los de este proyecto, fabricados con la LM.

$$\frac{E}{E_s} = 0.85\left(volumefraction\right)^{2.38}(MPa)$$

ec.(4.1)

$$\frac{\sigma_R}{\sigma_y} = 0.39\left(volumefraction\right)^{2.04}(MPa)$$

ec.(4.2)

Los parámetros mecánicos y morfológicos presentaron siempre variaciones pequeñas en muestras de igual diseño, lo que implica no sólo que el SLM es una técnica fiable y de alta repetibilidad sino que, además, en futuros trabajos, un escafoide escogido aleatoriamente de un determinado lote podría considerarse representativo de aquellos del mismo lote, fabricados a partir del mismo diseño.

La caracterización morfológica de los escafoides objeto de este estudio se realizó en estado de precarga en la nueva máquina de ensayo, situada dentro de la micro-CT. Se constató que la micro-CT es una técnica precisa para la caracterización morfológica de escafoides porosos para implantación ósea de Ti6Al4V fabricados vía SLM, empleando la fracción volumétrica medida vía Arquímedes como referencia física.

Los ensayos de compresión escalonados, combinados con la toma de imágenes vía micro-CT, permitieron estudiar la evolución de los parámetros morfológicos de los escafoides bajo distintos estados de compresión y en el momento de la fractura. Se concluyó que los ensayos de compresión escalonados se traducen en propiedades mecánicas significativamente distintas de aquéllas obtenidas en ensayos continuos en el caso de los escafoides porosos de Ti6Al4V fabricados vía SLM.

El diámetro de columna, que se diseñó de igual tamaño para todas las muestras, resultó ser constante bajo cualquier carga compresiva independientemente del diseño del escafoide, lo cual es una muestra más de la buena ejecución de la técnica SLM. Se realizó un primer acercamiento a la comprensión de la dependencia de variables como la porosidad o la anisotropía con la variación de la carga de compresión. No obstante, no pudo corroborarse mediante el análisis de las imágenes correspondientes, un trabajo que se está llevando a cabo en la actualidad. De un primer análisis de las imágenes radiográficas se concluyó que el mecanismo de fractura podría depender del tamaño de poro. Un estudio en mayor profundidad podría encaminar hacia la localización y comprensión de los mecanismos de fractura.

Resumiendo, finalmente se ha establecido un protocolo para futuros estudios en los que se vaya a emplear el ensayo de compresión escalonado

combinado con la toma de imágenes vía micro-CT en escafoides porosos para implantación ósea de Ti6Al4V fabricados por RP.

6. Bibliografía

1988 Gibson, L. J. and M. F. Ashby, "Cellular Solids. Structure & Properties."1988.

1994 Boyer, R., G. Welsch and E. W. Collings, "Materials properties handbook: titanium alloys",ASM international, 1994.

1997 Hildebrand, T. and P. Ruegsegger, "A new method for the model independent assessment of thickness in three dimensional images." J.Microsc., 185,(67-75, 1997.

1998 Bart-Smith, H., A. F. Bastawros, D. R. Mumm, A. G. Evans, D. J. Sypeck and H. N. G. Wadley, "Compressive deformation and yielding mechanisms in cellular Al alloys determined using X-ray tomography and surface strain mapping." Acta Materialia, 46,(10): 3583-3592, 1998.

1999 De Man, B., J. Nuyts, P. Dupont, G. Marchal and P. Suetens, "Metal streak artifacts in X-ray computed tomography: A simulation study." Ieee Transactions on Nuclear Science, 46,(3): 691-696, 1999.

1999 Ding, M., A. Odgaard and I. Hvid, "Accuracy of cancellous bone volume fraction measured by micro-CT scanning." Journal of Biomechanics, 32,(3): 323-326, 1999.

1999 Schrooten, J., "Ontwikkeling en evaluatie van een Ti6Al4- oraal implantaat met een bioactieve glasdeklaag." Departement Metaalkunde, Katholieke Universiteit Leuven, 1999.

2000 De Man, B., J. Nuyts, P. Dupont, G. Marchal and P. Suetens, "Reduction of metal streak artifacts in x-ray computed tomography using a transmission maximum a posteriori algorithm." Ieee Transactions on Nuclear Science, 47,(3): 977-981, 2000.

2001 Kinney, J. H., G. W. Marshall, S. J. Marshall and D. L. Haupt, "Three-Dimensional Imaging of Large Compressive Deformations in Elastomeric Foams", Journal of Applied Polymer Science, 80,(1746-1755, 2001.

2002 Muller, R., T. Bösch, D. Jarak, M. Stauber, A. Nazarian, M. Tantillo and S. Boyd, "Micro-mechanical evaluation of bone microstructures under load." Proceedings of SPIE, 4503,(189-200, 2002.

2003 Hollander, D. A., T. Wirtz, M. Von Walter, R. Linker, A. Schultheis and O. Paar, "Development of Individual Three-Dimensional Bone Substitutes Using "Selective Laser Melting"." Eurpean Journal of Trauma, 2003.

2003 Kruth, J. P., Advances in selective laser sintering, International Conference on Advanced Research in Virtual an Rapid-prototyping, 2003.

2003 Sachlos, E. and J. T. Czernuszka, "Making tissue engineering scaffolds work. Review on the application of solid freeform fabrication technology to the production of tissue engineering scaffolds." European Cells and Materials, 5,(2003.

2004 Hutmacher, D. W., M. Sittinger and M. V. Risbud, "Scaffold-based tissue engineering: rationale for computer-aided design and solid free-form fabrication systems." Trends in Biotechnology, 22,(7): 354-362, 2004.

2004 Nazarian, A. and R. Muller, "Time-lapsed microstructural imaging of bone failure behavior." Journal of Biomechanics, 37,(1): 55-65, 2004.

2004 Van de Casteele, E., "Model-based approach for Beam Hardening Correction and Resolution Measurements in Microtomography." Faculteit Wetenschappen, Departement Natuurkunde, Universiteit Antwerpen, 2004.

2004 Yeong, W. Y., C. K. Chua, K. F. Leong and M. Chandrasekaran, "Rapid prototyping in tissue engineering: challenges and potential." Trends in Biotechnology, 22,(12): 643-652, 2004.

2005 Benouali, A. H., L. Froyen, T. Dillard, S. Forest and F. N'Guyen, "Investigation on the influence of cell shape anisotropy on the mechanical

performance of closed cell aluminium foams using micro-computed tomography." Journal of Materials Science, 40,(22): 5801-5811, 2005.

2005 Dillard, T., F. N'Guyen, E. Maire, L. Salvo, S. Forest, Y. Bienvenu, J. D. Bartout, M. Croset, R. Dendievel and P. Cloetens, "3D quantitative image analysis of open-cell nickel foams under tension and compression loading using X-ray microtomography." Philosophical Magazine, 85,(19): 2147-2175, 2005.

2005 Nagaraja, S., T. L. Couse and R. E. Guldberg, "Trabecular bone microdamage and microstructural stresses under uniaxial compression." Journal of Biomechanics, 38,(4): 707-716, 2005.

2005 Nazarian, A., M. Stauber and R. Muller, "Design and implementation of a novel mechanical testing system for cellular solids." Journal of Biomedical Materials Research Part B-Applied Biomaterials, 73B,(2): 400-411, 2005.

2006 Kerckhofs, G., J. Schrooten, M. Wevers, P. Van Marcke and V. Cleynenbreugel, "Standardisation and Validation of Micro-CT for the Morphological Characterisation of Porous Structures." ECNDT, 2006.

2006 Li, J. P., J. R. de Wijn, C. A. van Blitterswijk and K. de Groot, "Porous..." Biomaterials, 27,(1223-1235, 2006.

2006 Ohgaki, T., H. Toda, M. Kobayashi, K. Uesugi, M. Niinomi, T. Akahori, T. Kobayash, K. Makii and Y. Aruga, "In situ observations of compressive behaviour of aluminium foams by local tomography using high-resolution X-rays." Philosophical Magazine, 86,(28): 4417-4438, 2006.

2007 Li, J. P., P. Habibovic, M. van den Doel, C. E. Wilson, J. R. de Wijn, C. A. van Blitterswijk and K. de Groot, "Bone ingrowth in porous titanium implants produced by 3D fiber deposition." Biomaterials, 28,(18): 2810-2820, 2007.